Nuclear Spin Noise
Examined by
Magnetic Resonance Force Microscopy

Inauguraldissertation

zur Erlangung der Würde eines Doktors der Philosophie

vorgelegt der
Philosophisch-Naturwissenschaftlichen Fakultät
der Universität Basel

von

Benedikt Eduard Herzog

aus Beromünster, LU und Luzern, LU

Basel, 2018

Genehmigt von der Philosophisch-Naturwissenschaftlichen Fakultät auf Antrag von

Prof Dr. Martino Poggio
Fakultätsverantwortlicher

Prof. Dr. Ernst Meyer
Korreferent

Basel, den 20.06.2017

Prof. Dr. Martin Spiess
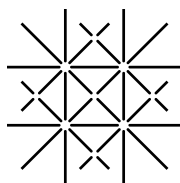Dekan

Doktorarbeit
PhD Thesis

Nuclear Spin Noise
Examined by
Magnetic Resonance Force Microscopy

Benedikt Eduard Herzog

12.07.2018

U N I
B A S E L

Universität Basel - Departement Physik

Wollen musst du!
Alles andere ist freiwillig.

–

Meinem Vater,
der in mir immerzu die Faszination des Verstehens und Erklärens förderte
und durch den ich nun das Umarmen des Unverständlichen lerne;

Meiner Mutter,
deren unermessliche und unbedingte Liebe erst
uns beide unseren Weg gehen lässt.

Contents

Abstract

This doctoral thesis deals with magnetic resonance force microscopy (MRFM), a highly sensitive method for measuring finest magnetic moments, for example nuclear spins.

By measuring the different polarisation modes of an ensemble of magnetic moments of ^{19}F atomic nuclei, the number of measured spins was determined to be $\sim$ 1,000,000 and the measurement volume to (26.3 nm) ^{3}. On the one hand, such an ensemble has statistical fluctuations; On the other hand, it follows a Boltzmann distribution in an external magnetic field. The two polarisation modes differed in their dependence on the number of particles of the ensemble. The variance of the force evoked by the spins is proportional to the square root of the particle number. The absolute value of the thermal polarisation though depends linearly on the magnetic field. Thereby an expression for the number of particles as a function of the two measured forces can be derived, which only includes the temperature and the strength of the external magnetic field as measuring constants. Knowledge about the exact spatial distribution of the magnetic field is not necessary, as it is in the case of other methods. In principle, the simple method can also be directly applied to other physical investigations in which thermal and statistical polarisation is measurable.

The implementation of MRFM requires the entire effort from the production of samples and microscope components, through the setup, operation and further development of the apparatus including its control software, up to the data evaluation. Due to this circumstance, the practical examination of the apparatus and its description is comparatively more detailed, at the costs of more successful experimental results. Even if the work on the MRFM project was carried out solo for the most part, – without the help of various persons from the research group of Prof. Dr. Martino Poggio including his own research management, it would not have been possible for me to carry it out.

The outline of this work can be found in section 1.2.

Zusammenfassung

Diese Doktorarbeit behandelt Magnet-Resonanz-Kraft-Mikroskopie (MRFM), ein höchst sensitives Verfahren um feinste magnetische Momente, zum Beispiel von Kern-Spins, zu messen.

Durch Messen der verschieden Polarisationsarten eines Ensembles magnetischer Momente von ^{19}F Atomkernen wurde die Anzahl gemessener Spins auf $\sim 1'000'000$ und das Messvolumen auf $(26.3 \text{ nm})^3$ bestimmt. Ein solches Ensemble weist zum einen statistische Fluktuationen auf; andererseits folgt es in einem äusseren Magnetfeld einer Boltzmann-Verteilung. Die beiden Polarisationsarten unterschieden sich in ihrer Abhängigkeit von der Teilchenanzahl des Ensembles. Die Varianz der durch die Spins hervorgerufenen Kraft, verhält sich proportional zur Quadratwurzel der Teilchenanzahl. Hingegen ist der absolute Wert der thermischen Polarisierung durch das Magnetfeld linear davon abhängig. Dadurch kann ein Ausdruck für die Teilchenanzahl in Abhängigkeit der beiden gemessenen Kräfte hergeleitet werden, welcher nur die Temperatur und die Stärke des äusseren Magnetfeldes als Messkonstanten beinhaltet. Kenntnisse über die genaue räumliche Verteilung des Magnetfeldes, wie das bei anderen Methoden zutrifft, sind nicht notwendig. Grundsätzlich kann die simple Methode auch direkt auf andere physikalische Untersuchungen angewendet werden, in denen thermische und statistische Polarisierung messbar ist.

Die Durchführung von MRFM erfordert den gesamten Aufwand vom Herstellen der Proben und Mikroskop-Bestandteilen, über das Einrichten, Betreiben und Weiterentwickeln der Messapparatur inklusive deren Steuerungssoftware, bis hin zur Auswertung der Daten. Diesem Umstand ist die verhältnismässig ausführliche praktische Untersuchung der Messapparatur und deren Beschrieb, zulasten von mehr experimentellen Ergebnissen geschuldet. Die Arbeit am MRFM Projekt wurde grösstenteils solo erbracht, – doch ohne die Mithilfe verschiedener Personen der Forschungsgruppe von Prof. Dr. Martino Poggio und insbesondere seiner eigenen Forschungs-Leitung hätte sie nicht erbracht werden können.

Die Gliederung dieser Arbeit befindet sich in Abschnitt 1.2.

Abbreviations

Abbreviation	Full Form
AC	Accelerated Current
AFM	Atomic Force Microscopy
AM	Amplitude Modulated
ARP	Adiabatic Rapid Passage (pulse)
AWG	Arbitrary Waveform Generator
BIR	B_1-Insensitive Rotation (pulse)
DAQ	Data AcQuisition
DFB	Distributed FeedBack (laser)
ESR	Electron Spin Resonance
FM	Frequency Modulated
FPGA	Field Programmable Gate Array
HS	Hyperbolic Secant
LO	Local Oscillator
NMR	Nuclear Magnetic Resonance
MRFM	Magnetic Resonance Force Microscopy
MRI	Magnetic Resonance Imaging
PIN	p-type – Intrinsic – n-type (photodiode)
PCI	Peripheral Component Interconnect
PID	Proportional-Integrative-Derivative (controller)
PM	Phase Modulated
PXI	PCI eXtensions for Instrumentation
RF	Radio Frequency (frequencies in the kHz regime)
SNR	Signal to Noise Ratio

List of Symbols

- Vectors are denoted as $\vec{X}$, whereas for their absolute value the same symbol X is used only without $\vec{}$, unity vectors as $\hat{e}_x, \hat{e}_y, \hat{e}_z$.

- Fourier transforms as well as quantum mechanical operators are denoted as $\hat{x}, \hat{I}$.

- The time derivatives of a quantity are denoted as $\dot{x}, \ddot{x}$.

- The term *magnetic field* $\vec{B}$ is used for the quantity strictly called magnetic flux density, measured in Tesla [T]. The magnetic field strength $\vec{H}$ in units of [A/m] does not appear in this work avoiding any confusion.

- If not indicated explicitly, the single-sided convention of spectral densities spanning only over positive frequencies is used (e.g. $S_x(f)$).

Symbol	Description	Unit
A	Cross-sectional area	[m^2]
α	^{4}He nucleus	
$\alpha_p(t)$	Angle between ω_{eff} and $\hat{e}'_x$	[rad]
α_t	Displacement-voltage transduction coefficient	[V/m]
$\vec{B}_0$	External, static magnetic field, note $\vec{\omega}_0 = \gamma \vec{B}_0$	[T]
$\vec{B}_1$	AC magnetic field (RF field), note $\vec{\omega}_1 = \gamma \vec{B}_1$	[T]
$\vec{B}_{\text{eff}}$	Effective magnetic field $\vec{B}_0 + \vec{B}_1$	[T]
$\vec{B}_{\text{tip}}, B_{\text{tip}_z}$	Gradual magnetic field of the nano-magnet, its z-component	[T]
B_z	Total magnetic field in z-direction $B_0 + B_{\text{tip}_z}$	[T]
β_{HS}	Truncation factor of a HS pulse	[ ]
β_n	Wave-vectors of the cantilevers oscillation	[1/m]
$\vec{D}(\vec{r}, t)$	Cantilever's 3-dimensional displacement function	[m]
c	C-factor (correction of the paddle's displacement)	[ ]
d	Cantilever's thickness	[m]
d_{sep}	Distance between cantilever tip and surface	[m]
E	Young's modulus	[Pa]
E_I^S	Imaginary part of the surface layer's E	[Pa]
E_m	Eigenenergies of μ_z in B_z	[J]
ϵ_{signal}	Error noise of the measured signal	[V^2]

F_{min}	Minimal measurable force per unit bandwidth	$\left[\mathrm{N}/\sqrt{\mathrm{Hz}}\right]$
F_{th}	Thermal noise force	[N]
$F_{t_{\mathrm{pol}}}$	Magnetic force measured at $t = t_{\mathrm{pol}}$	[N]
F_S	Shear force	[N]
F_x	Force in x-direction acting on the cantilever	[N]
	Frequencies related to magnetic fields	
$\vec{\omega}_0$	Frequency vector of $\vec{B}_0$; $\gamma\vec{B}_0$	[rad/s]
$\vec{\omega}_1(t)$	Frequency vector of $\vec{B}_1$; $\gamma\vec{B}_1$	[rad/s]
$\vec{\omega}_{\mathrm{eff}}$	Frequency vector of $\vec{B}_{\mathrm{eff}} = (\vec{\Delta\omega} + \vec{\omega}_1)/\gamma$	[rad/s]
$\vec{\Delta\omega}$	Frequency vector of the magnetic field pointing along the z-axis; $\vec{\omega}_0 - \vec{\omega}_{\mathrm{RF}}$	[rad/s]
	ARP pulse related frequencies	
$f_{\mathrm{centre}}, \omega_{\mathrm{centre}}$	Centre frequency of ω_{RF}, f_{RF}	[Hz], [rad/s]
$f_{\mathrm{RF}}(t), \vec{\omega}_{\mathrm{RF}}(t)$	Modulated carrier frequency of an ARP pulse	[Hz], [rad/s]
Ω	Offset from ω_{res}	[rad/s]
Ω_{max}	Maximal Ω for which the spins get still inverted.	[rad/s]
$\Delta f_{\mathrm{mod}}, \Delta \omega_{\mathrm{mod}}$	modulation width of $f_{\mathrm{RF}}(t)$	[Hz], [rad/s]
ω_{2p}	ARP sequence frequency (360° inversion); $2\pi/2t_p$	
	Other Frequencies	
$\Delta f_{\mathrm{BW}}, \Delta \omega_{\mathrm{BW}}$	Measurement bandwidth	[Hz], [rad/s]
$\Delta f_{\mathrm{BW_{min}}}$	Minimal measurement bandwidth	[Hz]
ω_{FWHM}	Full width at half maximum of e.g. a Lorentzian curve	[rad/s]
$f_{\mathrm{L_0}}, \omega_{\mathrm{L_0}}$	Resonance frequency of the cantilever's fundamental mode	[Hz], [rad/s]
$\omega_{\mathrm{L}n}$	Resonance frequency of the cantilever's n-th mode	[rad/s]
$f_{\mathrm{res}}, \omega_{\mathrm{res}}$	Spin resonance frequency	[Hz], [rad/s]
$f_{\mathrm{off\text{-}res}}$	Frequency far away from f_{res}	[Hz]
$\vec{G}$	Magnetic field gradient vector field $\nabla\vec{B}$	[T/m]
G_{zx}	One-dimensional magnetic field gradient $\partial B_z/\partial x$	[T/m]
Γ_0	Intrinsic dissipation; $m\gamma_0$	[kg rad/s]
γ_0	Dissipative constant	[rad/s]
γ	Gyromagnetic ratio	[rad/(s T)]
$h, \hbar$	Plank's constant, reduced Plank's constant	[kg m^2/s]
$\hat{I}, \hat{I}_z$	Dimensionless nuclear spin / angular momentum operator, its z-component	[ ]
I_y	Area moment of inertia	[m^4]
l	Cantilever's length	[m]
λ	Laser's wavelength	[m]
k	Spring constant	[N/m]
k_B	Boltzmann constant	[J/K]
k_m	Magnetic spring constant	[J/T^2]

κ	2$^{\text{nd}}$ derivative of $u_s(z)$ with respect to z, (approx.)	[rad/m]
M_{By}	Bending moment in y-direction	[N m]
$\vec{M}, M_z$	Ensemble's magnetisation, its z-component	[N m/T]
m	Cantilever's effective mass	[kg]
m_s	Eigenvalues of $\hat{I}_z$	[ ]
$\vec{\mu}, \mu_z$	Magnetic moment of a single, its z-component	[N m/T]
Q	Quality factor	[ ]
ρ	Density	[kg/m^3]
$\vec{S}$	Nuclear spin / angular momentum $\hbar\vec{I}$	[kg m^2/s]
S_F	Spectral density of the thermal noise force (white)	[N^2/Hz]
$S_V(f)$	Spectral density of the cantilever's displacement	[V^2/Hz]
$S_{V_{\text{floor}}}$	Spectral density of total noise other than thermal (white), $\alpha^2 S_{x_N} + S_{V_N} \approx S_{x_N}$	[V^2/Hz]
S_{V_N}	Spectral density of electronic (white)	[V^2/Hz]
$S_x(f)$	Spectral density of the cantilever's displacement	[m^2/Hz]
S_{x_D}	Double-sided spectral density of the cantilever's displacement	[m^2 s/rad]
S_{x_N}	Spectral density of displacement noise other than thermal (white)	[m^2/Hz]
$\sigma^2_{\text{spin-signal}}$	Variance of the cantilever's displacement depending on the forced caused by the spin inversion.	[V^2]
σ^2_{ip}	Variance of the cantilever's displacement in-phase with B_1	[V^2]
σ^2_{qd}	Variance of the cantilever's displacement out-of-phase with B_1, quadrature	[V^2]
σ_{M_z}	Standard deviation of the ensembles magnetisation in z-direction	[N m/T]
T_1	Spin-lattice / longitudinal relaxation time	[s]
$T_{1\rho}$	Spin-lattice relaxation time in the rotating frame	[s]
T_2	Spin-spin / transversal relaxation time	[s]
T_{L_0}	Period of the cantilever's fundamental mode; $1/f_{\text{L}_0}$	[s]
t_{aqui}	Acquisition time for a single MRFM measurement	[s]
$t_{\text{lock-in}}$	Lock-in amplifier's time constant	[s]
t_p	Length of an ARP pulse	[s]
t_{pol}	Polarisation time	[s]
τ_m	Spin ensemble correlation time	[s]
θ	Angle of cantilever's curvature	[rad]
$u_n(z)$	n-th mode of the cantilever's dynamical displacement function	[m]
$u_s(z)$	Cantilever's static displacement function	[m]
w	Cantilever's width	[m]

$X(z,t)$	Cantilever's one-dimensional, dynamic displacement function	[m]
$x_n(t)$	n-th mode of the time dependence of the cantilever's motion	[m]
$x(t)$	Fundamental mode of the time dependence of the cantilever's motion	[m]

List of Figures

1 Introduction

> 66 *(...), ipse se nihil scire id unum sciat.*
>
> ∼ *Ich weiss, dass ich nichts weiss.* 99

Cicero über **Sokrates**, *Academici libri quattuor*, 45 v. Chr.

1.1 Motivation

MAGNETIC phenomena are omnipresent in our daily life and will increasingly dominate the technological progress via spintronics, digital information storage and possibly also one day via quantum computing. The main direction is simple: smaller, faster, more sensitive.

RESONANCE is a phenomenon in which a force drives a system to oscillate with much greater amplitude at specific frequencies. Through magnetic resonance, the alleged feeble characteristics of spins are enhanced. Or: it simply is their nature of interaction. There is a second resonant behaviour too: the one of the force transducer.

FORCE MICROSCOPY transduces information about the behaviour or attributes of a phenomenon with little loss, i.e. with a high quality factor. With micro-mechanical force transducers like cantilevers quality factors in the ten-thousands to millions are reached, but the ceiling is probably still further away. Transducing information goes both ways. Being able to watch means also to be able to manipulate.

MAGNETIC RESONANCE FORCE MICROSCOPY is an important, versatile, far away from fully developed and hence fascinating instrument to conduct research on nuclear and electron spin phenomena.

Over the last 25 years, magnetic resonance force microscopy (MRFM) has led to exciting progress in the field of ultra-sensitive spin-detection and high-resolution magnetic resonance imaging (MRI) microscopy. Starting with early demonstrations in the 1990s imaging with resolutions of a few micrometres, the technique has progressed to the point where it can resolve single virus particles and molecular monolayers. Further development is ongoing; recent improvements in various components have put 1-nm resolution within reach without major modifications to the instrument, and moreover opened the door to faster imaging as well as high resolution spectroscopy by MRFM. The extension of MRFM to atomic resolution, where atoms in molecules could be directly mapped out and located in 3D, remains an exciting even if technically very challenging prospect [1].

Motivations enough to take a closer look.

1.2 Thesis Outline

In chapter 1 Introduction the short form of MRFM's working principle including an overview of the force sensitivity is given. The review of MRFM's history and state of the art shows the progress of this technique towards higher imaging resolution and advanced spectroscopic measurements of nuclear spins.

Chapter 2 Theory touches the physics of nuclear spins. The precise mathematical expressions of adiabatic rapid passage pulses are derived, whereas a more practical approach is given in chapter 4.

Chapter 3 Experimental Setup treats the MRFM apparatus including the cantilever physics, the set-up of the further key components and the interferometric motion detection. This is done in detail, on one side in order to carry out what is needed to do MRFM and on the other side to give the toeholds for further improvement.

Chapter 4 Classic Magnetic Resonance Force Microscopy explains the methods of normal, classic MRFM. Simply: how does MRFM work in the lab.

In chapter 5 Thermal versus Statistical Polarisation the reported simultaneous measurement of thermal and statistical nuclear spin polarisation is reviewed and extended.

Chapter 6 Magnetic Vortex as Gradient Source covers the idea and made efforts towards MRFM with magnetic vortices as gradient source. It explains the motivation for this project and possible reasons for the lacking success.

The thesis is concluded with chapter 7 Outlook pointing out why MRFM is a very promising technique for applications in nano-science. Especially for doing microscopy on nanoscale biological samples such as cells and even proteins, or for research related to novel solid state spin physics, e.g. towards quantum computing. It shall be highlighted already here that even the successful combination of today's achieved improvements of single MRFM components would give a nanometre scale resolution.

1.3 MRFM in a Nutshell

By MRFM small ensembles of nuclear spin states are measured and manipulated in a non-destructive way. Combined with the scanning technique known from e.g. atomic force microscopy (AFM) true three dimensional, isotope selective images of nuclear spins density distribution in the nanometre regime can be made.

Nuclear spin noise has already been predicted by Bloch in his pioneering 1946 paper on nuclear induction [2]. He noted that in the absence of any external radio-frequency (RF) driving field a sample of N spins of magnetic moment $\vec{\mu}$ contained in a pickup coil would induce very small voltage fluctuations proportional to $\sqrt{N}\vec{\mu}$ [3].

1.3.1 Basic Working Principle

The very short form of "how MRFM works" goes as summarised below. The full working principle is carried out in section 4.1 The characteristics of the individual components can be found in the according sections in chapters 3 and 4.
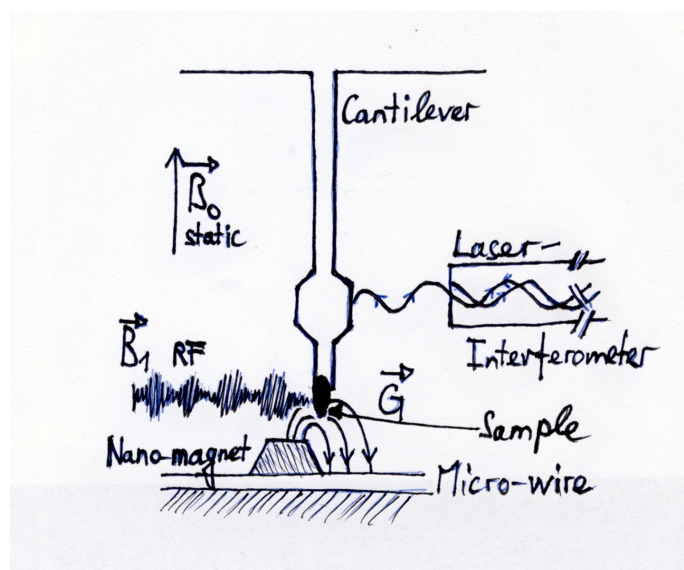
FIGURE 1.1: MRFM WORKING PRINCIPLE
The sample (fully black), containing magnetic moments $\vec{\mu}$, sits on the tip of the cantilever which serves as force transducer; the nano-magnet provides the high gradient field $\vec{G}$; with the electromagnetic RF field $\vec{B}_1$ the spins in the sample are inverted; the "external" magnetic field $\vec{B}_0$ sets the resonance frequency $f_{\text{res}} = {}^{\gamma B_0}/{2\pi}$; and with the laser interferometer the cantilever's displacement, which is proportional to the magnetic force $F_x = \mu_z G_{zx}$, is measured.

There exist atomic nuclei with a spin characteristic $\vec{s}$ with the spin quantum number I. These spins align in a static magnetic field $\vec{B}_0 = B_0 \hat{e}_z$ along its direction and split for

the case of $I = 1/2$ into two states, parallel $\langle\downarrow|$ and anti-parallel $\langle\uparrow|$ to $\vec{B}_0$.

In order to invert the population of the two states an oscillating magnetic field $\vec{B}_1 = B_1(t)\hat{e}_x$ perpendicular to $\vec{B}_0$ is applied and its frequency $f_{\text{RF}}(t)$ is swept through the resonance frequency $f_{\text{res}} = \Delta E_{m_s}/h$ of the two level system, where ΔE_{m_s} is the difference of the potential energy between $\langle\downarrow|$ and $\langle\uparrow|$. The method - known as adiabatic rapid passage - is characteristic for MRFM since it matches the slow dynamics of the cantilever[1] and it is less sensitive to field inhomogeneities.[2] [4–6]

With the inversion of the spin also the magnetic moment $\vec{\mu} = \gamma\vec{S}$, where γ is the isotope specific gyromagnetic ratio, is inverted. The change $\Delta\mu$ can be measured via the force it experiences in a magnetic field gradient according to $\Delta\vec{F} = \Delta\mu\vec{G}_{zx}$. As a source for the gradient $\vec{G}_{zx} = \partial B_z/\partial x$ typically a nano-sized magnet is used.

The sample containing the magnetic moments is attached to a cantilever which serves as a force transducer. The change in force $\Delta\vec{F}$ alters the oscillation of the cantilever whose motion is measured via a laser interferometer. Finally the signal is analysed with a lock-in amplifier to separate the part which originates from the spins flipping from the thermal motion of the cantilever and electronic noise.

In order to measure $\vec{\mu}$ in different parts of the sample, the sample on the cantilever is scanned by means of sub-nanometre precise positioners trough the regions of highest gradient. True three-dimensional (3D), non-destructive images can be reconstructed by deconvolution of the measured 3D spin-density map.

1.3.2 Sensitivity

In order to detect and manipulate fewer and fewer number of spins and since the ambitious idea of a detecting the magnetic moment of a single proton [7] has not been achieved yet, sensitivity plays a leading role in MRFM. The sensitivity of a measurement can be expressed by its signal to noise ratio (SNR), where the desired signal, arising from magnetic moments, is compared with the background noise of the setup. Hereby either the respective powers $\text{SNR} = P_{\text{signal}}/P_{\text{noise}}$ or the variances $\text{SNR} = \sigma_{\text{signal}}^2/\sigma_{\text{noise}}^2$ are confronted. For force detected magnetic resonance the theoretical SNR is given by eq. (3.58)

$$\text{SNR}_{\text{th}} = N\frac{(\mu_z G_{zx})^2}{S_F\Delta\omega_{\text{BW}}} \quad, \tag{1.1}$$

whereas N is the number of nuclei, μ_z a single atom's magnetic moment in z-direction, S_F the spectral density of the thermal force noise and $\Delta\omega_{\text{BW}}$ the bandwidth of the measurement.

In the present case of a thermally limited measurement the noise of the read-out

---

[1] A typical fundamental cantilever frequency of $f_? \approx 3\,\text{kHz}$ sets the time for the inversion by a single ARP pulse to $t_p = 1/(2f_{L_0}) \approx 150\,\mu\text{s}$.

[2] In macroscopic MRI, other inversion and detection methods not suited for MRFM are often used. Examples are measurements of the Larmor frequency or pulsing methods as spin echo pulses.

system is much lower than inherent thermal noise of the measurement technique. It can be neglected therefore. The latter is characterised S_F as derived in section 3.1.7, which is for a mechanical transducer eq. (3.53)

$$S_F = \frac{4k_B T m \omega_{\mathrm{L}_0}}{Q} = \frac{4k_B T k}{\omega_{\mathrm{L}_0} Q} = 4k_B T \Gamma_0 \quad ,$$
(1.2)

where k_B is the Boltzmann constant, T is the temperature, m the cantilever's effective mass, ω_{L_0} its fundamental resonance frequency, Q its quality factor, $k = m\omega_{\mathrm{L}_0}^2$ its spring constant and $\Gamma_0 = k/\omega_{\mathrm{L}_0} Q$ its intrinsic dissipation.

The minimal measurable force per unit bandwidth is $F_{\text{min-uBW}} = \sqrt{S_F \times 1[\text{rad} / \text{s}]}$. With the frequency in [Hz], $f_{\mathrm{L}_0} = \omega_{\mathrm{L}_0}/2\pi$ it reads eq. (3.57):

$$F_{\text{min-uBW}} = \sqrt{2k_B T \frac{k}{\pi Q f_{\mathrm{L}_0}}} \quad .$$
(1.3)

This points out which parameters can and have to be improved in order to increase the sensitivity. Namely: to increase the gradient G_{zx}, to decrease the temperature T, to decrease the product of the effective mass m and the resonance frequency ω_{L_0} of the cantilever, respectively its spring constant k, as well as increase its quality factor Q.

1.4 History and State of the Art of MRFM

This section gives a brief overview of the origins and the development of MRFM until the present day. For a more detailed review, the reader is pointed to the book chapter

Force-Detected Nuclear Magnetic Resonance
by *M. Poggio and B. E. Herzog*
to appear in *Micro and Nano Scale NMR: Technologies and Systems*,
edited by *Jens Anders and Jan G. Korvink*,
Wiley-VCH, Weinheim, 2017 [1].

This thesis and the book chapter were written in parallel; some parts are mutually built upon each other. Earlier reviews and book chapters discussing different aspects of the progress of MRFM were written by Poggio and Degen (2012, 2010) [8, 9], Kuehn et al. (2008) [10], Barbic (2008) [11], Hammel et al. (2007) [12], Berman et al. (2006) [13], Suter (2004) [14], Nestle et al. (2001) [15], and Sidles et al. (1995) [16].

1.4.1 Force versus Inductive Detection

In order to understand why force-detected NMR is well-suited to small sample volumes, the analysis of Sidles and Rugar [17] gives a comprehensive explanation. They compare

inductive and mechanical methods for detecting magnetic resonance considering both detection setups as oscillators coupled to a spatially localized magnetic moment.

In the first case the oscillator is an electrical LC circuit – the pick-up coil – inductively coupled to the magnetic moment. In the second case the oscillator is a mechanical spring – the cantilever – holding the magnetic moment, which is coupled to the field gradient of a nearby magnet. The two cases turn out to be mathematically identical and can be characterised by three parameters: an angular resonance frequency ω_0, a quality factor Q, and a "magnetic spring constant" k_m with units of [J/T ^{2}], which is defined in a way that both the electrical and mechanical oscillators are treated on the same footing.

The authors show that the signal-to-noise ratio of the two magnetic resonance detection schemes is proportional to:

$$SNR \propto \sqrt{\frac{\omega_0 Q}{k_m}} \quad . \tag{1.4}$$

For conventional inductive detection with a cylindrical coil, k_m is proportional to the volume of the coil; where for force detection k_m depends on the magnetic field gradient $\vec{G}$ and the size and aspect ratio of the cantilever: $k_m \propto {}^{Gwd^3}/{l^3}$, where w, d, and l are the width, thickness, and length of the cantilever, respectively.

The minute dimensions and extreme aspect ratios of cantilevers as well as the strong micro- and nanometre-scale magnets routinely realised by modern fabrication techniques ensure that k_m is much smaller for modern force-detected techniques than for inductively-detected techniques. An MRFM apparatus using a cantilever with a mechanical spring constant $k = 50$ μN/m and a magnetic tip with field gradient $G_{zx} = 5 \cdot 10^6$ T/m has $k_m = 2 \cdot 10^{-18}$ J/T^2; a small coil of 4 turns with a diameter of 1.8 mm and a length of 3 mm has $k_m = 1.2 \cdot 10^{-2}$ J/T^2 [18]. Inductive coils often exhibit a higher ω_0 than force detected schemes, typically between 100 MHz and 1 GHz in the first case and a few kHz in the latter. Contrarily, mechanical devices usually have a Q that surpasses the one of inductive circuits ($Q \sim 100$) by orders of magnitude. For example state-of-the art cantilevers achieve Q between 10^4 and 10^7, yielding a minimal measurable force $F_{\min}$ around 1 aN (eq. (3.57)), – less than a billionth of the force needed to break a single chemical bond. Finally, due to the huge difference in k_m of more than a quadrillion (10^{15}), force detection is leading the race for highest sensitivity.

Intuitively this comparison can be understood by considering the quantity k_m, as the energy required to produce an oscillating field within the volume of the inductive coil. For the cantilever, it is the energy required to produce the same oscillating field within the sample by moving it in the magnet's field gradient. The huge disparity can be understood by considering that producing an oscillating field within the whole volume of an inductive pick-up coil can easily require more energy than moving a tiny sample on a compliant cantilever through a magnetic field gradient.

The higher SNR of force detection together with the nanometre positioning precision of scanning probe microscopy allow image resolutions of far below 1 μm and even

atomic resolution can – in principle – be aspired.

1.4.2 History

This subsection gives an overview of the historical development of MRFM, starting with its roots and the major steps of progress. Subsequently the simultaneous progress with the aspect on the different components of MRFM is reviewed, hence the overview is not continuous in time.

THE ROOTS, THE IDEA AND THE FIRST IMPLEMENTATION OF MRFM: Force-detection techniques in NMR experiments date back to Evans in 1956 [19], and were also used in paramagnetic resonance measurements by Alzetta et al. in the 1960s [20].

In 1985 Sleator et al. were able to measure nuclear spin noise, i.e. the statistical fluctuations of the ensemble's magnetisation, using a superconducting quantum interference device (SQUID) [3, 21].

In 1981 Binnig, Gerber and Weibel introduced the scanning tunnelling microscope (STM) [22], which – for the first time – provided real-space images of individual atoms on a surface. The closely related invention of the atomic force microscope (AFM) by Binnig [23] and its subsequent realization by Binnig, Quate and Gerber [24], both in 1986, eventually expanded atomic-scale imaging to a wide variety of surfaces beyond the conducting materials made possible by STM.

It is in the midst of these developments in the 1980s and early 1990s that modern force-detected NMR was born. As scanning probe microscopy (SPM) expanded its applications to magnetic force microscopy (MFM), Sidles proposed a force microscopy based on magnetic resonance as a method to improve the resolution of MRI to molecular length-scales [7, 25, 26].

Soon after the proposal in 1991 Rugar realised the first micrometre-scale experiment using an AFM cantilever [27], demonstrating mechanically detected ESR in a 30 ng sample of diphenylpicrylhydrazyl (DPPH). The original apparatus operated in vacuum and at room temperature with the sample attached to the cantilever. A mm-sized coil produced an RF magnetic field tuned to the electron spin resonance of DPPH at 220 MHz with a magnitude of 1 mT. The electron spin magnetisation was modulated by varying the strength of an 8 mT polarising magnetic field in time. A nearby NdFeB magnet produced a magnetic field gradient of 60 T/m, which, as a consequence of the sample's oscillating magnetisation, resulted in a time-varying force between the sample and the magnet. This force modulation was converted into mechanical vibration by the compliant cantilever. Displacement oscillations were detected by a fibre-optic interferometer achieving a thermally limited force sensitivity of 3 fN/$\sqrt{\text{Hz}}$.

Following this initial demonstration of cantilever-based MRFM, the technique has undergone a series of developments towards higher sensitivity that, as of today, is 7 orders of magnitude better than that of the 1992 experiment [8]. Nevertheless, the basic idea of

detecting magnetic resonance using a compliant cantilever and a strong magnetic field gradient persists.

MAJOR STEPS OF PROGRESS: The fabrication of very soft (low spring constant) and high quality factor cantilevers made in 1994 the first mechanical NMR experiment on a micrometre-scale ammonium nitrate sample possible [28].

In 1996 Zhang et al. used the technique to detect ferromagnetic resonance (FMR) in a micrometre-scale yttrium iron garnet (YIG) film [29].

A major step towards higher sensitivity was made by incorporating the MRFM instrument into a cryogenic apparatus in order to reduce the thermal force noise of the cantilever. A first experiment carried out in 1996 at a temperature of 14 K achieved a force sensitivity of 80 aN/$\sqrt{\text{Hz}}$ [30], a roughly 50-fold improvement compared to 1992, mostly due to the higher cantilever mechanical quality factor and the reduced thermal noise achieved at low temperatures.

In 2003 researchers approached the level of sensitivity necessary to measure statistical fluctuations in small ensembles of electron spins, a phenomenon that had previously only been observed with long averaging times [31]. Further refinements finally led to the demonstration of single electron spin detection in 2004 [32].

PULSE SCHEMES: In the first ESR experiment the amplitude of the polarising field (B_0) was modulated in order to periodically saturate the magnetisation [27]. Already in the subsequent experiment, adiabatic rapid passage (ARP) by sweeping the RF field frequency and amplitude was used to invert the magnetisation [28]. In the following different pulse schemes were developed to avoid spurious excitation of the cantilever [33, 34]. Other protocols include the detection of spin signals in the form of a shift in the cantilever resonance frequency (rather than changes in its oscillation amplitude) [35], and a scheme that relies on detecting a force-gradient, rather than the force itself [36].

CANTILEVERS: The force transducer's spectral noise density is crucial for the sensitivity of the measurement. Around 2000 a force sensitivity in the range of $\sim$ 10 fN/$\sqrt{\text{Hz}}$ at room temperature and just below $\sim$ 1 aN/$\sqrt{\text{Hz}}$ at millikelvin temperatures was measured [37, 38].

Since 2003 the most used force sensors in MRFM are mass loaded single crystal silicon cantilevers [39], like the ones used in this work and described in detail in section 3.1. Several approaches have been tried to enhance the sensitivity of this type of levers. The minimal measurable force of a cantilever is proportional to

$$F_{\text{min}} \propto \sqrt{\frac{k}{f_{\text{L}_0}Q}} \propto \sqrt{\frac{wd^2(E\rho)^{1/2}}{Ql}} \propto \sqrt{\frac{d^2}{Q}} \qquad , \qquad (1.5)$$

where E is the Young's modulus, ρ the density, and w, d and l, width, thickness and

length of the cantilever. Without changing the material and the basic geometry Q and k (which depends mainly on d), remain for optimisation.

The quality factor Q can be increased by annealing the levers in UHV which reduces surface dissipation (section 3.1.5). This can give an improvement of about one order of magnitude, though it is lost again when the levers are exposed to air. Surface passivation before exposure can reduce this effect [40]. Though finally, the overall enhancement is limited.

The idea to reduce the spring constant k by reducing the thickness d is counteracted by the simultaneous reduction of Q due to enhanced surface dissipation which comes with thinner levers [41, 42].

This type of cantilever has probably reached its limit. For further improvement of the sensitivity other approaches as discussed in section 1.4.3 have to be developed.

ALTERING THE CANTILEVERS NATURAL MOTION: Active feedback control of the cantilever's motion improves its motional stability and enables instrument designs of much higher sensitivity and faster imaging than passive designs [43]. Garbini, Bruland et al. introduced optimal control of the cantilever's oscillation in the late 1990s [43–45]. The damping of the motion increases the minimal measurement bandwidth and thereby the overall sensitivity and was further improved by new technological abilities [46, 47].

SPECTROSCOPY: The prospect of applying the MRFM technique to nanoscale spectroscopic analysis has also led to efforts towards combination with pulsed NMR and ESR techniques. MRFM is ill suited to high-resolution spectroscopy as broadening of resonance lines by the strong field gradient of the magnetic tip completely dominates any intrinsic spectral features. Nevertheless a number of advances have been made. In 1997, MRFM experiments carried out on phosphorus-doped silicon were able to observe the hyperfine splitting in the ESR spectrum [48]. Roughly at the same time a series of basic pulsed magnetic resonance schemes were demonstrated to work well with MRFM, including spin nutation, spin echo, T_1 and $T_{1\rho}$ measurements [49, 50].

In 2002 researchers applied nutation spectroscopy to quadrupolar nuclei in order to extract local information on the quadrupole interaction [51]. This work was followed by a line of experiments that demonstrated various forms of NMR spectroscopy and contrast, invoking dipolar couplings [52], cross polarisation [53, 54], chemical shifts [55], and multidimensional spectroscopy [55].

More recently, experiments in which magnetic field gradients can be quickly switched on and off, have again raised the possibility of doing high resolution spectroscopy by MRFM. Nichol et al. used a nanometre-scale metallic constriction, similar to the micro-wire, to produce both a switchable magnetic field gradient and the RF field [56] (see section 1.4.3). Tao et al. demonstrated the use of a commercial hard disk write head for the production of large switchable gradients [57].

SAMPLE ON CANTILEVER OR VICE VERSA: The usually chosen configuration in MRFM experiments is the sample-on-cantilever scheme where the source for the gradient field is e.g. on a chip brought to its vicinity. Though the places of two objects can also be switched. Already in 1998 researchers introduced the "magnet-on-cantilever" scheme [30], where the roles of gradient magnet and sample were interchanged. Using this approach field gradients of up to $2.5 \cdot 10^5$ T/m were obtained by using a magnetized sphere of 3.4 μm diameter [58]. These gradients were more than 3 orders of magnitude larger than those achieved in the first MRFM experiment. A decade later the idea was tried anew by at least two research groups. Nickel nanorods with a diameter of 120 nm attached to a cantilever yielded gradients of $5.4 \cdot 10^6$ T/m [59, 60]. My predecessor investigated nickel nanowires and FeCo coated needles expecting to have gradients of $\sim 10^6$ T/m, but without experimental success in MRFM [61].

IMAGING: In addition to steady advances in sensitivity researchers also pushed the capabilities of MRFM for imaging. The first one-dimensional MRFM image was made using ESR detection in 1993 and soon after was extended to two and three dimensions [62–64]. These experiments reached about 1 μm axial and 5 μm lateral spatial resolution, which is roughly on par with the best conventional ESR microscopy experiments today [65]. In 2003 sub-micrometre resolution (170 nm in one dimension) was demonstrated with NMR on optically pumped GaAs [66]. In parallel, researchers started applying the technique for the 3D imaging of biological samples, like the liposome, at micrometre resolutions [67]. Shortly thereafter an 80 nm voxel size was achieved in an ESR experiment that introduced an iterative 3D image reconstruction technique [48]. The one-dimensional imaging resolution of the single electron spin experiment in 2004, finally, was about 25 nm [32].

In 2007 Mamin et al. measured nuclear fluorine spins of a CaF_2 sample and achieved a lateral resolution of 90 nm. The enhancement was achieved due to nanoscale magnetic tips consisting of a multilayer of Fe/CoFe/Ru [68]. The group at the IBM research laboratory further improved the design of the magnet and merged it together with a new source for the RF field. They replaced the previous coil with a lithographically designed 200 nm thick, 2.6 μm long and 1.0 μm wide micro-wire. On top of it a 200 nm wide FeCo nano-magnet was placed. It is the ancestor of the micro-wires described in section 3.4 and chapter 6. This historical review is by no means complete.

1.4.3 State of the Art

In this subsection four selected improvements of the recent past are highlighted: diamond cantilevers, nanowires and carbon nanotubes as force transducers, as well as switchable magnetic field gradients for high resolution spectroscopy by MRFM and faster imaging. They reflect the avant-garde of future, more sensitive MRFM.

DIAMOND CANTILEVERS AS FORCE SENSORS: Using diamond instead of silicon and keeping the basic geometry the same is a possible way to improve the sensitivity. Tao et al. [69] demonstrated with single crystal diamond cantilevers a force sensitivity $F_{min} = 0.11$ fN/$\sqrt{\text{Hz}}$ at room temperature and 6 aN/$\sqrt{\text{Hz}}$ at 3 K, respectively 0.54 aN/$\sqrt{\text{Hz}}$ at 100 mK in the best case. Although diamond has a higher density and Young's modulus which would decrease the sensitivity, the lower dissipation of single crystal diamond counterbalances this. At 3 K Q was typically $\sim 1.5 \times 10^6$ and at millikelvin temperatures it reached almost 6×10^6. Important for the Q is also the surface termination, where the best results were found for oxygen-terminated devices compared to fluorine-terminated or untreated ones. A detailed explanation on dissipation Q^{-1} is given in section 3.1.5.

The investigated cantilevers were between 20 and 240 μm long, between 8 and 16 μm wide and between 80 and 800 nm thick. By improving the processing technique cantilevers with dimensions of 240 μm × 1 μm × 50 nm should be possible to be manufactured. Such cantilevers would have $F_{min} = 9.4$aN/$\sqrt{\text{Hz}}$ (300 K), 0.49 aN/$\sqrt{\text{Hz}}$ (3 K) respectively 45 zN/$\sqrt{\text{Hz}}$ (100 mK).

The advantages of this diamond cantilevers are that the detection method with the laser interferometer is well known in handling and its noise is thermally limited. Further, nitrogen-vacancy (NV) centres can be implemented by doping, which opens the door for applications like single-photon generation, quantum engineering and again nanoscale magnetic spectroscopy [70–72]. Though the downside is, that the fabrication is of high purity, single crystal diamond cantilevers is demanding, e.g. single crystal can not be grown on other material, and expensive.

NANOWIRE AS FORCE SENSORS: High force sensitivity principally demands two characteristics of a force transducer: a long, narrow and thin geometry and low dissipation. By making the devices smaller and smaller the surface to volume ratio increases which makes surface dissipation the dominant loss mechanism. Due to the manufacturing process *top-down* fabricated structures exhibit a not completely reducible imperfectness. Optical as well as electron-beam lithography have a limited resolution and contamination by chemical agents is unavoidable. An approach to defect free and clean structures are self-assembled or directed self-assembled *bottom-up* fabrication methods as chemical vapour deposition (CVD) or molecular beam epitaxy (MBE), wherewith e.g. nanowires and carbon nanotubes can be grown.

Nanowires can have diameters from a few to hundreds of nanometres [73] and can be several micrometres long. Spring constants therefore lie in the range of tens to several hundreds of μN/m [74]. The often single crystalline structure together with, where appropriate, a straightforward added surface treatment at the end of the fabrication process ensures low surface dissipation. Due to the very high surface to volume ratio the surface purity and chemistry plays an even more important role as for cantilevers. So far, e.g. Q factors of up to 37×10^3[75] have been reported.

A challenge for all kinds of ultra-sensitive mechanical force transducers is to measure the displacement precisely and without back action. The standard optical interferometer scheme [76] usually used to measure the cantilevers displacement has its limit for very narrow structures. For wires with a diameter below ~ 50 nm their cross-section with the laser beam and thus the reflectivity becomes too low and the noise of the read out system is for the given power disturbing. Nichol et al. [77] used polarised laser light to measure nanowires with a diameter of 40 to 60 nm. The parallel to the nanowire oriented light showed a 50-fold higher reflectivity compared to perpendicular orientation. Like this a displacement sensitivity of 0.5 pm/$\sqrt{\text{Hz}}$ at a low enough laser power (15 µW) avoiding heating of the wire was achieved.

For nanowires with a 90 degree rotational symmetry the two transverse oscillation modes are degenerated. Due to a small asymmetry in the cross-section this degeneracy can be lifted and the frequencies of the two perpendicular modes are slightly spaced. The two modes can (in future) be used to simultaneously measure forces along the two oscillation directions. Classical cantilevers are only sensitive along their main flexural mode. Further, exploiting the nonlinear motion of the nanowires allows mechanical mixing and amplification of signal excitation through this mixing. With the demonstrated gain of 26 dB force sensitivities of ~ 100 zN/$\sqrt{\text{Hz}}$ should be possible [75].

The difficulty with nanowires comes with their size. As mentioned highest cleanness is important and the motion detection is demanding. Further, as for cantilevers, it holds, that the connection to the substrate is crucial. Up to now, artificial attachment at a favourable arbitrary position without introducing significant clamping losses has not been demonstrated. E.g. attachment methods as glueing are not rigid enough. So far, the best results have been achieved with nanowires as-grown from the substrate. A further issue is, that for the interferometer detection the nanowires should be close to an edge of the substrate. Though, most nanoscale manufacturing techniques achieve best results away from the edges of the substrate. E.g. spin-coating used for optical and e-beam lithography produces a bulge at the edges changing thickness and thus precision; the non-uniform electric field hinders or makes self assembly techniques impossible.

NANOTUBES AS FORCE SENSORS: Following further the approach of transducers with low effective mass and low dissipation unavoidably also carbon nanotubes (CNT) come into question.

CNTs exhibit the highest known Young's modulus [78]. But with single wall CNTs – which have a diameter of ~ 1.4 nm and are very long (~ 4 µm) – spring constants k as low as ~ 10µN/m can be achieved. Due to the perfect molecular composition CNT have extremely high quality factors. At 30 mK it can be as high as 5 million and at 1.2 K $\sim 50'000$. Together with an effective mass m in the order of 10^{-20} kg this leads to a sensitivity of $F_{\min} = 12$ zN/$\sqrt{\text{Hz}}$ at 1.2 K. For millikelvin temperatures an improvement of at least one order of magnitude is expected [79].

The optical detection of CNTs thermal vibration at room temperature has been

demonstrated for a thin rope of nanotubes ($d = \sim 6$ nm) by placing the CNT inside a fibre-based high finesse optical cavity [80]. The resolution of 70 pm/$\sqrt{\text{Hz}}$ is high enough to resolve the motion at low temperatures too.

The displacement of CNTs can also be measured electrically. The vibration of a suspended nanotube over a gate electrode modulates the capacitance. Thereby also the conductivity of the CNT and thus the bias current at the fringes of the Coulomb blockaded regime is modulated. By converting the current into a voltage signal and applying a cross-correlation measurement scheme the weak signal from the thermal oscillation can be extracted from the overwhelming electric noise.

SWITCHABLE MAGNETIC FIELD GRADIENTS: One of the limitations of using a nanoscale magnetic particle as source for the gradient dB_z/dx is that the gradient can not be varied or turned off without physically changing the arrangement (of cantilever and magnetic particle). This reduces the sensitivity of a series of well-established MRI schemes, like Fourier [81, 82] or Hadamard [83] encoding. A main advantage of such acquisition schemes is that during the measurement time the signal from the full volume of the sample is acquired. Faster signal acquisition significantly enhances the SNR ratio compared to techniques where the signal is recorded sequentially. It has been demonstrated that these techniques can be used in MRFM with a constant gradient [84, 85]. But the present gradient during the encoding pulse enhances de-phasing and the spectral line-width of the NMR resonance peaks, which makes it not applicable for spectroscopic techniques as e.g. chemical shift imaging. It is also technically possible to flip away the magnet in order to turn the gradient on and almost off [86, 87], though the movement disturbs the equilibrium state the of the whole arrangement, whereby the spatial resolution stayed limited to the micrometre scale.

A different approach developed by Nichol et al. [88] is to remove the magnet and employ the magnetic field of the already present micro-wire as gradient. For this purpose MAGGIC (Modulated Alternating Gradients Generated with Currents), a new MRFM spin detection protocol, was developed and engaged with a nanowire serving as force transducer.

The protocol basically consists of a sequence of four alternating pulses: (1) a spin inversion pulse, (2) an oscillating gradient pulse, (3) a second inversion pulse and (4) a second oscillating gradient pulse but with opposite sign.

The inversion pulses (1 & 3) are identical to the conventional amplitude and frequency modulated adiabatic rf pulses with the centre frequency $f_{\text{NMR}} = \gamma B_0$ and modulation width Δf_{mod}. But contrary to classical MRFM, their purpose is not to generate the alternating force at the force sensors resonance frequency f_{nanowire}. When the magnetic moment of the spin ensemble is inverted by the inversion pulse, the sign of the next gradient pulse is altered as well.

It is the gradient pulses (2 & 4), that generate the alternating force. They oscillate with f_{nanowire} and thereby produce a force arising from the spins according to $F_x = m_z dB_z/dx$

with the frequency f_{nanowire}.

The length of the whole sequence T_{seq} is chosen much shorter than the correlation time τ_m of the statistical spin fluctuations, as well as it is much longer than the nanowire oscillation period, i.e. $\tau_m \gg T_{\text{seq}} \gg 1/f_{\text{nanowire}}$. Setting the time scales like this makes it possible to measure (and average) the non-zero variance $\langle m_z^2(t) \rangle$ long enough to exceed the measurement noise.

By changing the sign of the gradient pulse every half period of the sequence, Fourier components at f_{nanowire} are avoided in order to reduce spurious excitation of the nanowire. Since both the spin ensembles magnetisation and the sign of the gradient pulses are simultaneously inverted, the amplitude of the force F_x (at f_{nanowire}) does not change the sign.

In order to achieve the essential high magnetic field gradients by a conducting wire, the current density flowing through it has to be as high as possible. Therefore the micro-wire is narrowed to a several hundred nanometre wide and similarly long constriction exhibiting a current density in the order of 10^7 A/cm^2. This produces a gradient of $\sim 10^5$ T/m at a distance of 80 nm. The authors predict that with even smaller constrictions gradients of 10^6 T/M by current densities of 10^9 A/cm^2 are possible.

A proof-of-concept Fourier transform MRI imaging experiment, with the at the beginning mentioned multiplex enhancement, has been demonstrated [56].

2 Theory

> *If I were forced to sum up in one sentence what the Copenhagen interpretation says to me, it would be **'Shut up and calculate!'**.*
>
> David Mermin, *What's Wrong with this Pillow?* [89][1], 1989

OVERVIEW: In section 2.1 of this chapter a brief overview of the theoretical description of (nuclear) spin physics in a static field including the comparison of the involved energies is given. For an advanced theoretical description the reader is pointed to established textbooks on this topic, as e.g. *Principles of Magnetic Resonance* by Slichter [5] – whereupon this excerpt is based – or to other PhD theses on this topic [18, 61].

Section 2.2 gives an extended view on the spin inversion by adiabatic rapid passage (ARP) completive to section 4.1.1.

However, the major description of MRFM is carried out in chapters 3 to 5, especially in section 4.1.

2.1 The Physics of Nuclear Spins

2.1.1 Nuclear Spins and Magnetic Moment

Atomic nuclei carry an intrinsic form of angular momentum called spin $\vec{S}$ which is quantified by the spin quantum number I, whereas $2I \in \mathbb{N}_0$. Associated with $\vec{S}$ is the magnetic moment $\vec{\mu}$ of the nuclei. The two quantities are related via the gyromagnetic ratio[2] γ, characteristic for each isotope of a chemical element [90], according to

$$\vec{\mu} = \gamma \vec{S} \quad . \tag{2.1}$$

Particles with $\vec{S}, \vec{\mu} \neq 0$, e.g. single nucleons, electrons and some composed structures like atomic nuclei, show magnetic phenomena including magnetic resonance. However, the present work only focuses on atomic nuclei.

---

[1]Even though MRFM is not (yet?) quantum mechanics in the strict sense.

If applicable, I rather prefer Heisenberg over von Neumann and Bohr (and Mermin).

[2]Values for γ are typically listed in two different types of units, in [rad/(s T)] and, by a factor of 2π smaller, in [Hz/T]. If not otherwise specified the convention of γ in units of [rad/(s T)] is used.

Quantum mechanics states that the projection of $\vec{S}$ measured along any axis can only take on a discrete set of $2I + 1$ values [91]. For z as the conventionally taken projection axis, the z-components S_z of $\vec{S}$ are written as

$$S_z = m_s\hbar \quad , \text{ where} \tag{2.2}$$
$$m_s = \{-I, -I + 1, \ldots, I\} \tag{2.3}$$

is the dimensionless magnetic quantum number and $\hbar$ is the reduced Plank's constant.

The dimensionless angular momentum (or spin) operator $\hat{\vec{I}}$ with the z-component $\hat{I}_z$ is defined as [5]

$$\hat{\vec{I}} = \frac{\hat{\vec{S}}}{\hbar} \quad . \tag{2.4}$$

2.1.2 Spins in a Static Magnetic Field

LEVEL SPLITTING: In a static magnetic field $\vec{B}_0 \neq 0$ the potential energy of two states with different $\vec{S}$ is not any more degenerated. The energy levels are split up due to the coupling of $\vec{S}$ to $\vec{B}_0$, i.e. the (nuclear) Zeeman effect. The corresponding potential energy of the states is given by

$$E_m = -\vec{\mu} \cdot \vec{B}_0 = -\hbar\gamma B_0 m_s \quad , \tag{2.5}$$

which are the eigenenergies of the Hamiltonian [5]

$$\hat{H} = -\hat{\mu}_z B_z = -\hbar\gamma\hat{I}_z B_z \quad . \tag{2.6}$$

Considering two states with a difference in m_s of 1 and setting $\vec{B}_0$ along the z-axis, the potential energy difference between these two states is

$$\Delta E_m = \gamma\hbar B_0 \quad . \tag{2.7}$$

This is true for the simplest case of $s = 1/2$ which results in a two-level system with $m_s = \pm 1/2$, but also for nuclei with $s > 1/2$ with three or more levels. In these cases the energy difference of each two neighbouring levels is ΔE_m. In the following a system with $s = 1/2$ is regarded, which simplifies the further depiction. The state of $\vec{\mu}$ with $m_s = -1/2$ pointing in the same direction as $\vec{B}_0$, is denoted as *up* $|\uparrow\rangle$ and the opposite state as *down* $|\downarrow\rangle$.

The two level system of a spin in a magnetic field can absorb and re-emit electromagnetic radiation. It exhibits a resonance behaviour at the frequency ω_{res} corresponding to ΔE_m, here it is $\omega_{\text{res}} = \gamma B_0$.

For higher order spins, the carried out principals stay roughly the same, although the mechanism is more complex and the specific conditions for the adiabatic inversion are

slightly different [92].

LARMOR PRECESSION: Placing a magnetic moment $\vec{\mu}$ in a magnetic field produces an unbalanced torque on $\vec{\mu}$ which causes its orientation to change. The *equation of motion of a magnetic moment in a magnetic field* can be derived classically and reads [5]:

$$\frac{\mathrm{d}\vec{\mu}}{\mathrm{d}t} = \vec{\mu} \times \vec{B}_0 \quad , \tag{2.8}$$

which holds also for a time dependant field $\vec{B}(t)$. Unsurprisingly the quantum mechanical derivation by solving the Schrödinger equation leads to the very same results as derived in [5] too.

For a static magnetic field $\vec{B}_0$, the above equation says that $\vec{\mu}$ describes a precession about $\vec{B}_0$ with a fixed angle between the two vectors. Its frequency - the Larmor frequency - is equal to ω_{res}, as long as no other fields are involved.

Adding to the static field $\vec{B}_0$ an electromagnetic AC field $\vec{B}_1(t) \perp \vec{B}_0$, the Larmor precession is influenced by the effective magnetic field $\vec{B}_{\mathrm{eff}} = \vec{B}_0 + \vec{B}_1(t)$. The effect of the oscillating field $\vec{B}_1(t)$ can be visualised in a rotating frame of reference (called *frequency modulated frame*) and even in a *doubly rotating frame*, as carried out in the following section 2.2.2.

COMPARISON OF ZEEMAN SPLITTING-, INTERACTION- AND THERMAL-ENERGY: For atomic nuclei the thermal energy $k_B T$ is even at cryogenic temperatures and very high fields much higher than the energy splitting, $k_B T \gg \Delta E_m$, e.g. for $T = 1$ K $\rightarrow k_B T \approx 6 \cdot 10^{-23}$ J; for $B_0 = 10$ T and ^{1}H $\rightarrow \Delta E_m \approx 2 \cdot 10^{-26}$ J. This implies for a single nuclear spin, that it can occupy all states without external excitation (other than the thermal). For an ensemble of spins, it means that the occupation of the available states follows a Boltzmann distribution, as discussed in section 5.2.1.

The interaction of individual spins in solids is usually only weak. It is either directly via the dipolar coupling or additionally, if existing, mediated by conduction electrons. The magnetic dipole interaction energy of two protons at typical bond length (100 pm) is in the order of 10^{-30} J.

However, for the performed measurements a non-interacting ensemble of spins can be assumed, since the coupling energy between $\vec{S}$ of ^{1}H and B_0 is already for 1 mT an order of magnitude bigger than the dipolar spin-spin coupling, $\Delta E_m \approx 2 \cdot 10^{-29}$ J.

2.2 ARP-Pulses

Adiabatic rapid passage (ARP) is one particular method of manipulating spins by electromagnetic radiation out of the various collection of NMR sequences [5, 93]. The long

studied method is well known since the early days of magnetic resonance 1946 [94, 95] (1946).

ARP pulses are sweeps of the effective magnetic field $\vec{B}_{\text{eff}}$ which are slowly enough (adiabatically) that the magnetisation vector $\vec{M}$ of the spin ensemble can precess around $\vec{B}_{\text{eff}}$ (see Fig. fig. 2.1); but the sweeps are is still faster (rapid) than the relaxation times T_1 and T_2 [96].

In the next subsections, the first order hyperbolic secant pulse (HS1) is examined in detail. It is that type of ARP pulse, used in the present experiments. HS1 pulses are modulated in amplitude and frequency (phase), which is possible since late 90ies when the necessary hardware and software was available.

There exist less elaborated types of ARP pulses as the very early ones, where either only the amplitude of $\vec{B}_0$ or $\vec{B}_1$, or the frequency (phase) of $\vec{B}_1$ is varied (e.g. sawtooth and zigzag sweeps).

2.2.1 Fundamentals

Given are two magnetic fields, a static field $\vec{B}_0 = B_0 \hat{e}_z$ and a pulsed oscillating field $\vec{B}_1 = B_1(t)\hat{e}_x$. The effective field is the vector sum of the two, which reads in the laboratory frame:[3] $\vec{B}_{\text{eff}} = \vec{B}_0 + \vec{B}_1(t)$.

Fictitious fields arise in rotating reference frames due to the accelerated relative movement of the frames. All these fields have their origin in the two magnetic fields of the laboratory frame: $\vec{B}_0$ and $\vec{B}_1$. The fields are denoted as the respective resonance frequencies $\vec{\omega}_i = \gamma \vec{B}_i$, where gamma is the gyromagnetic ratio of the isotopically specific spin and i stands for the respective field. The effective field vector in the below introduced frequency modulated frame is given by [96]

$$\vec{\omega}_{\text{eff}} = \vec{\omega}_0 + \vec{\omega}_1 - \vec{\omega}_{\text{RF}} = \vec{\Delta\omega} + \vec{\omega}_1 \quad , \tag{2.9}$$

where $\vec{\omega}_{\text{RF}} = \omega_{\text{RF}}\hat{e}_z$ is the angular frequency vector of $\vec{B}_1(t)$ perpendicular to $\vec{\omega}_1$, which arises due to the coordinate transformation. It only affects spins which are on resonance at this particular frequency.

2.2.2 The Hyperbolic Secant Pulse in Different Frames of Reference

There are four different reference frames: the laboratory, phase modulated, frequency modulated, and doubly rotating frame.

---

[3]In other coordinate systems additional components arise due to the transformation.

LABORATORY FRAME: According to Garwood et al. [96], the HS1 pulse in the lab frame can be written as

$$\omega_1(t) = \omega_{1_{\max}} \left(\operatorname{sech}\left(\beta_{\mathrm{HS}} t \right) \right)^{1+i\nu} \quad , \tag{2.10}$$

where $\omega_{1_{\max}}$ is the maximum pulse amplitude and β_{HS} and ν are real constants. Equation (2.10) can be transformed in a phase modulated (PM) and in a frequency modulated (FM) representation as carried out in the following.

PHASE MODULATED FRAME: Instead of represented through the complex exponential, eq. (2.10) can be expressed with a modulated pulse phase $\phi(t)$. This phase modulated (PM) representation is given by [96]

$$\omega_1(t) = \omega_{1_{\max}} \operatorname{sech}\left(\beta_{\mathrm{HS}} t \right) e^{i\phi(t)} \quad , \quad \text{where} \tag{2.11}$$

$$\phi(t) = \nu \left(\ln\left(\operatorname{sech}\left(\beta_{\mathrm{HS}} t \right) \right) \right) \quad . \tag{2.12}$$

Thereby, the PM reference frame rotates with *constant* frequency ω_{centre} around an axis perpendicular to $\vec{\omega_1}$.

FREQUENCY MODULATED FRAME: In the frequency modulated (FM) representation as shown in fig. 2.1, the reference frame rotates with the time-dependent frequency $\omega_{\mathrm{RF}}(t)$ and eq. (2.10) is then described by the amplitude modulated (AM) function [96]

$$\omega_1(t) = \omega_{1_{\max}} \operatorname{sech}\left(\beta_{\mathrm{HS}} t \right) \quad , \tag{2.13}$$

and the frequency modulated (FM) function [96]

$$\omega_{\mathrm{RF}}(t) - \omega_{\mathrm{centre}} = \frac{\mathrm{d}\phi}{\mathrm{d}t} = -\nu \beta_{\mathrm{HS}} \tanh\left(\beta_{\mathrm{HS}} t \right) \quad . \tag{2.14}$$

In terms of the pulse length t_p, the modulation width $\Delta\omega_{\mathrm{mod}}$ and the truncation factor β_{HS}, the AM and FM functions of the HS1 pulse can be written as [96]

$$\omega_1(t) = \omega_{1_{\max}} \operatorname{sech}\left(\beta_{\mathrm{HS}} \left(2t/t_p - 1 \right) \right) \quad , \tag{2.15}$$

$$\omega_{\mathrm{RF}}(t) - \omega_{\mathrm{centre}} = -\frac{\Delta\omega_{\mathrm{mod}}}{2} \tanh\left(\beta_{\mathrm{HS}} \left(2t/t_p - 1 \right) \right) \quad . \tag{2.16}$$

A visualised explanation of the FM rotating frame is given in section 4.1.1 and fig. 4.1.

The spins precess around the effective field $\vec{\omega}_{\mathrm{eff}}$, the vector sum of the static field $\vec{\omega}_0$ and the AC field $\vec{B}_1$ with the two components $\vec{\omega}_{\mathrm{RF}} \perp \vec{\omega}_1$. The orientation is commonly
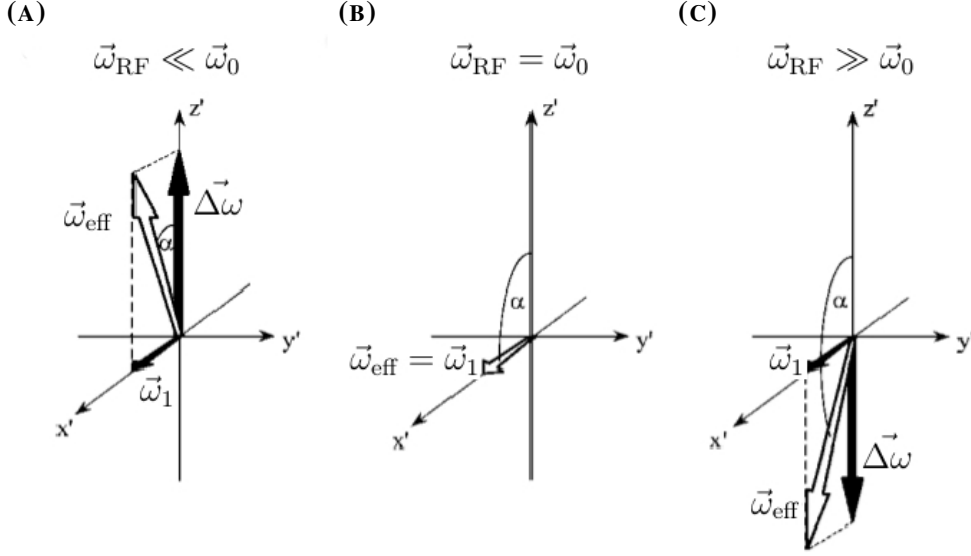
FIGURE 2.1: EFFECTIVE MAGNETIC FIELD $\vec{\omega}_{\text{EFF}}$ IN THE ROTATING FRAME
The components of $\vec{\omega}_{\text{eff}}$ are $\vec{\omega}_1$, the amplitude of the RF-field $\vec{B}_1$, and $\vec{\Delta\omega}$, the detuning of $\vec{B}_1$'s frequency from the resonance frequency $\omega_{\text{res}} = \omega_0$. The ensemble's magnetisation $\vec{M}$ precesses around $\vec{\omega}_{\text{eff}}$ and follows it as long as the adiabatic condition is fulfilled. The sequence shows the situations **(A)** far below resonance at the beginning, **(B)** at resonance and **(C)** far above resonance at the end of the sweep. Figure adapted from [96].

chosen as [96]

$$\vec{\omega}_1 = \gamma B_1 \hat{e}'_x \tag{2.17}$$

$$\vec{\Delta\omega}(t) = (\gamma B_0 - \omega_{\text{RF}}(t))\, \hat{e}'_z \quad , \tag{2.18}$$

where $\hat{e}'_x$ and $\hat{e}'_z$ denote the unity vectors in the FM frame. As can be seen from eqs. (2.17) and (2.18), the orientation of $\vec{\omega}_1$ stays fixed, only its amplitude changes. Though $\vec{\omega}_{\text{eff}}$ changes its orientation at the instantaneous velocity $\mathrm{d}\alpha_p/\mathrm{d}t$, where

$$\alpha_p(t) = \arctan\left(\frac{\omega_1(t)}{\Delta\omega(t)}\right) \quad . \tag{2.19}$$

COURSE OF ONE PASSAGE: The ARP pulse starts at $t = 0$ with ω_{RF} far below resonance ω_0, hence $\vec{\omega}_{\text{eff}} \approx \Delta\omega$. It is increased, which reduces $\vec{\Delta\omega}$ and rotates $\vec{\omega}_{\text{eff}}$ around $\hat{e}'_y$, the y unity vector of the FM frame. At resonance $\omega_{\text{RF}} = \omega_0$, thus $\vec{\Delta\omega} = 0$ and $\vec{\omega}_{\text{eff}}$ points along $\hat{e}'_x$. Increasing ω_{RF} further makes $\vec{\Delta\omega}$ negative and continuously rotates $\vec{\omega}_{\text{eff}}$ until it points at $t = t_p$ in opposite direction then at the start. A more

descriptive explanation of the ARP in the FM frame including the visualisation is given in section 4.1.1 and fig. 4.1.

ADIABATIC CONDITION: The condition that the passage happens, i.e. the ensemble's magnetisation $\vec{M}$ follows $\vec{\omega}_{\text{eff}}$, is that the passage is done sufficiently slow enough.[4] How slow it has to be is quantified by the adiabatic condition: *The magnitude of the effective field has to be much bigger then the speed of its rotation;*

$$|\omega_{\text{eff}}(t)| \gg \left|\frac{\mathrm{d}\alpha_p}{\mathrm{d}t}\right| \quad , \tag{2.20}$$

whereas α_p is the angle between the z' and $\vec{\omega}_{\text{eff}}$ [96]. Further, it has to be provided that $\vec{\omega}_{\text{eff}}$ undergoes a full $180\,°$ rotation. This means that the condition $\Delta\omega \gg \omega_1$ has to be fulfilled at the beginning and the end of the sweep.

DOUBLY ROTATING FRAME: The FM frame does not give a visual explanation why $\vec{M}$ follows $\vec{\omega}_{\text{eff}}$. Therefore a doubly rotating frame, the ω_{eff}-frame, denoted by double primes (i'') is introduced (fig. 2.2). It rotates with the angular velocity $\mathrm{d}\alpha_p/\mathrm{d}t$ around $y' = y''$ and thus the orientation of $\vec{\omega}_{\text{eff}}$ is fixed in this frame.
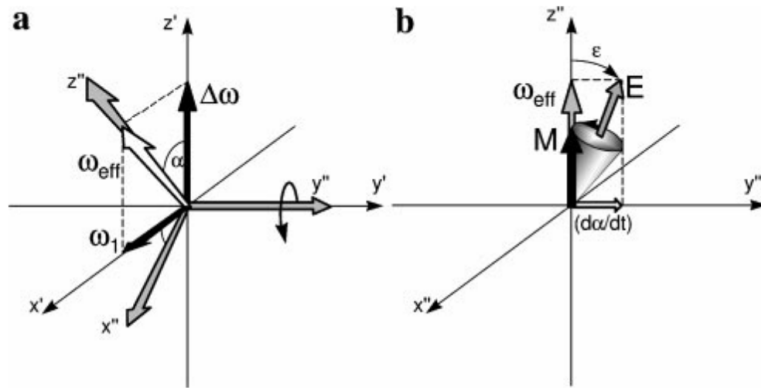
FIGURE 2.2: EFFECTIVE FIELD VECTOR IN THE DOUBLY ROTATING FRAME
(**a**) *Frequency Modulated (FM) Frame* - In black, the effective field vector $\vec{\omega}_{\text{eff}}$ with its components as shown in fig. 2.1a; in grey, the axes $x'', y''z''$ of the doubly rotating frame which rotates around y'. (**b**) *Doubly Rotating Frame* - The effective field vector $\mathbf{E} \equiv \vec{E}_p$ with its components $\omega_{\text{eff}} \cdot \hat{e}''_z$ from the FM frame and the contribution from the second transformation of coordinates $\mathrm{d}\alpha_p/\mathrm{d}t \cdot \hat{e}''_y$. The ensemble's magnetisation $\mathbf{M} \equiv \vec{M}$ precesses around $\vec{E}_p$. When the adiabatic condition is well satisfied ϵ is small, $\vec{M}$ strays never beyond an angle of 2ϵ from $\vec{\omega}_{\text{eff}}$ and $\vec{M}$ follows the rotation of $\vec{B}_{\text{eff}}$ in the laboratory frame. Figure taken from [96].

---

[4]But still faster then the longitudinal and transverse spin relaxation times T_1, T_2.

Thereby, a further fictitious field component $^{\mathrm{d}\alpha_p}/_{\mathrm{d}t} \cdot \hat{e}_y''$ arises and the effective field in the doubly rotating frame is now the vector sum $\vec{E}_p = \omega_{\mathrm{eff}} \cdot \hat{e}_z'' + {^{\mathrm{d}\alpha_p}}/_{\mathrm{d}t} \cdot \hat{e}_y''$ as visualised in fig. 2.2(b).

$\vec{M}$ precesses around $\vec{E}_p$ on the cone of angle ϵ

$$\epsilon = \arctan\left(\frac{^{\mathrm{d}\alpha}/_{\mathrm{d}t}}{\omega_{\mathrm{eff}}}\right) \quad , \tag{2.21}$$

and thus it strays never beyond an angle of 2ϵ from $\vec{\omega}_{\mathrm{eff}}$. When the adiabatic condition (eq. (2.20)) is well satisfied ϵ is small, $\vec{M}$ closely traces ω_{eff} during the ARP [96].

DIFFERENT ISOCHROMATES: In a gradual magnetic field, neighbouring spins to the ones with resonance frequency $\omega_{\mathrm{res}} = \omega_0$ experience a slightly different field and exhibit therefore a resonance frequency $\omega_{\mathrm{res}} + \Omega$, whereas Ω is the offset from ω_{res}.

Whilst the 180 ° inversion of such spins within a certain boundary Ω_{max} (see section 4.1.1) happens within the same time, for a 90 ° rotation this is not true. After a $t_p/2$ not all spins of the ensemble, i.e. only the spins with ω_{res}, are in the equatorial, x'-y'-plane. For the mathematical description together with extensive depiction the reader is referred to Garwood et al. [96].

3 Experimental Setup

> 66 *Wo immer es ein Problem gibt, ist es meistens deins.* 99

Tomi Ungerer, *Besser nie als spät*, 2015

This chapter describes the experimental setup necessary to measure nanoscale magnetic resonance.

Section 3.1 treats the cantilever as force transducer, its deflection, motion, dissipation, resonant amplification and finally its spectral density determining the minimal measurable force. The sample preparation is overviewed in section 3.2, followed by the technical explanation of the magnetic pulse generation in section 3.3. The micro-wire, the nano-magnetic tip and the static magnetic field are discussed in sections 3.4 to 3.6. The interferometric motion detection including the microscope's core setup and the signal amplification are explained in section 3.7. Section 3.8 concludes the chapter with the overview of the cryogenic and vibration isolation system.

3.1 Cantilever

3.1.1 Introduction

MOTIVATION: One of the key components in MRFM is the cantilever. It acts as force transducer converting the magnetic force of the spins into a displacement which can be measured optically with very high accuracy and little adulteration. The signal transduction of the spins via magnetic force received by the cantilever is the fundamental difference of MRFM compared to classical (medical) MRI. MRFM's superior sensitivity is finally provided by the cantilever as signal transducer.

SECTION OVERVIEW: In section 3.1.2 the cantilevers *deflection* as preliminary stage for its oscillation is regarded; followed by section 3.1.3, the analysis of its *dynamical behaviour*. The determination of the *spring constant* is given in section 3.1.4. Section 3.1.5 treats the relevant *dissipation mechanisms* in detail. *Dissipation* Q^{-1} limits the sensitivity of the cantilever.[1] It is eventually one of the factors whereby MRFM's

---

[1]Different nomenclatures for dissipation exist. In this work the following is used:
dissipation $Q^{-1} = \Delta E_{\text{kin}}/2\pi E_{\text{kin}}$, [ ]; intrinsic dissipation $\Gamma_0 = m\omega_{\text{L}_0}Q^{-1}$, [kg rad/s^{-1}];
dissipation rate $\gamma_0 = \Gamma_0/m$, [rad/s^{-1}]; (see e.g. eqs. (3.35) and (3.36)).

sensitivity is at the same time limited and can possibly be improved. Dissipation is quantified by its inverse, the *quality factor Q*. In section 3.1.6 the *enhancement of the signal by the resonant behaviour* of the cantilever is derived. Section 3.1.7 finally concludes the description of the cantilever with the expression of the *signal to noise ratio* (SNR) based on the spectral density.

CHARACTERISTICS OF THE DEPLOYED CANTILEVERS: All measurements described in this work are made with the same type of cantilevers as shown in fig. 3.1. They are ultra-soft, made of un-doped silicon, with a paddle to reflect the laser and an additional mass at the tip to tune the harmonics. These cantilevers are developed and produced by Chui et al. [39] and used in a variety of ultra-high sensitivity measurements in MRFM[32, 68, 97–104] and other topics [40, 105–110].

Un-doped silicon is not conducting and exhibits a bigger band-gap than the laser's energy,[2] which minimises laser-, as well as RF-induced, self heating.

The cantilevers exhibit a typical length of 90 µm to 130 µm, a width of 4 µm and a thickness of 100 nm.

FIGURE 3.1: SCANNING ELECTRON MICROGRAPH OF A CANTILEVER
Silicon cantilever chip with a 120 µm long, 4 µm wide and 100 nm thick, mass-loaded cantilever. *Inset:* The magnification of the cantilever shows the octagonal paddle acting as moving mirror of the interferometer. The transition from the thin lever to the 2 µm thick additional mass appears as a slightly brighter stripe at the right side of the paddle. Pictures taken from Poggiolab archive.

About 15 µm above the tip a 10 µm wide, octagonal paddle serves as mirror for the

---

[2]The laser wavelength of 1550 nm corresponds to an energy of 0.8 eV, whereas the band-gap of Si is 1.11 eV.

laser interferometer. Its influence in the displacement detection is considered by the *c-factor* (section 3.1.3).

At the end of the cantilever a ~ 10 µm $\times 4$ µm wide and 2 µm thick mass is added epitaxially. It shifts the higher flexural harmonics away from the fundamental mode causing large gaps in the thermal mode spectra, which reduces the coupling to higher modes. Also at the base of the levers an additional mass is added on top of the chip. It causes a more rigid clamping, which suppresses losses by phonon radiation to the substrate.

Typical values of the quality factor Q reach from 30'000 to 80'000 at low temperatures [39, 104] and the spring constant k is usually around 75 µN/m to 90 µN/m [104, 105], determined through measurements of the thermal noise spectra. With this characteristics a force sensitivity of $< 10^{-12}$ m Hz$^{-1/2}$ aN is reached.

3.1.2 Cantilevers Deflection

MOTIVATION: Although the cantilever in MRFM is not operated in a static manner it is instructive to firstly consider a pure motionless deflection before examining the dynamical behaviour. The conversion of a force into a displacement is based on the same parameters in both cases. The static deflection differs from the mode shape of the cantilever derived by the dynamical consideration in that the energy distorting the beam is stored also in higher modes. Hence the static derivation gives a slightly bigger amplitude. Also the approximated mode shapes of the cantilever are slightly different for each approach.

Around 1700 the Basel mathematician and physicist Jacob Bernoulli discovered that *the curvature of an elastic beam at any point is proportional to the bending moment of that point* [111], which is one of the key steps in the following derivation whose fundamentals can be found e.g. in [112, 113].

DISPLACEMENT EQUATION: The cantilever is aligned along the z-direction, clamped at $z = 0$ and free at $z = l$. A force F_x acting in x-direction at the tip of the cantilever causes a deflection $u_s(z)$ in x-direction

$$\frac{\mathrm{d}u_s(z)}{\mathrm{d}z} = \tan\theta \approx \theta \quad , \tag{3.1}$$

whereas θ is the angle of the curvature for a small segment $\mathrm{d}s$ of the cantilever and $\mathrm{d}z$ is its projection on the z-axis, approximated for small deflections. The curvature κ is given by

$$\kappa = \frac{\mathrm{d}\theta}{\mathrm{d}s} \approx \frac{\mathrm{d}\theta}{\mathrm{d}z} \quad . \tag{3.2}$$
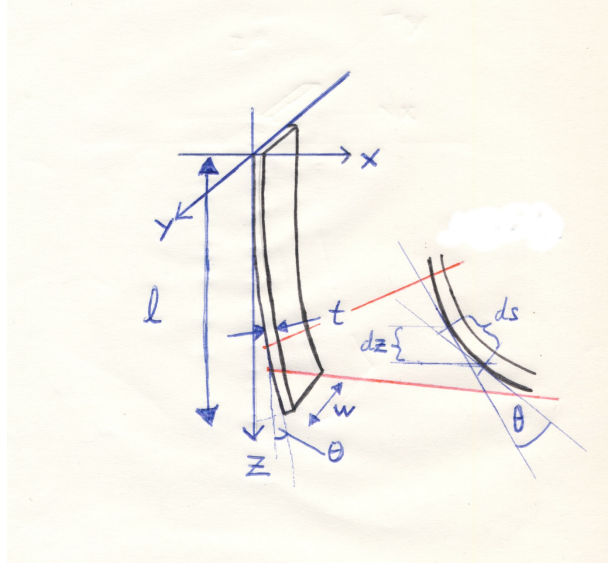
FIGURE 3.2: CANTILEVER'S DEFLECTION
Schematic of a bended cantilever depicting the dimensions of a deflected cantilever:
length l, width w, thickness[3] $t \equiv d$, the angle of curvature θ for a small segment $\mathrm{d}s$,
and its projection on the z-axis $\mathrm{d}z$.

Taking the first derivative of eq. (3.1) and combining it with eq. (3.2) we get

$$\frac{\mathrm{d}^2 u_s(z)}{\mathrm{d}z^2} = \frac{\mathrm{d}\theta}{\mathrm{d}z} = \kappa \quad . \tag{3.3}$$

For linear elastic beams the curvature κ is depending on the bending moment M_{By},
Young's modulus E and the area moment of inertia I_y according to [113]

$$\kappa = \frac{M_{By}}{EI_y} \quad . \tag{3.4}$$

This yields the *differential equation of the deflection curve* depending on the bending
moment M_{By} or a shear force $F_S = \mathrm{d}M_{By}/\mathrm{d}z$. M_{By}, respectively F_S is caused by an
arbitrary force $F_x = -F_S$ acting at the tip of the cantilever at $z = l$:

$$\frac{\mathrm{d}^2 u_s(z)}{\mathrm{d}z^2} = \frac{M_{By}}{EI_y} \quad , \tag{3.5}$$

$$u_s'''(z) \equiv \frac{\mathrm{d}^3 u_s(z)}{\mathrm{d}z^3} = -\frac{F_x}{EI_y} \quad . \tag{3.6}$$

This equation can be solved by integrating it three times:

$$u_s''(z)EI_y = -F_x z + c_1 \qquad \text{with } u_s''(0) = lF_x \Rightarrow c_1 = lF_x$$
$$u_s'(z)EI_y = -F_x z^2/2 + lF_x z + c_2 \qquad \text{with } u_s'(0) = 0 \Rightarrow c_2 = 0$$
$$u_s(z)EI_y = -F_x z^3/6 + lF_x z^2/2 + c_3 \qquad \text{with } u_s(0) = 0 \Rightarrow c_3 = 0$$
$$u_s(z)EI_y = F_x z^2(3l - z)/6 \quad . \tag{3.7}$$

The area moment of inertia I_y of a rectangular cross-section along its long side (i.e. width w) is

$$I_y = \int_A x^2 \mathrm{d}A = \int_{-d/2}^{d/2} \int_{-w/2}^{w/2} x^2 \mathrm{d}x \mathrm{d}y = wd^3/12 \quad . \tag{3.8}$$

Thereby we finally get mode shape for the *static displacement* in x-direction evoked by F_x

$$\boxed{u_s(z) = \frac{2z^2(3l - z)}{Ewd^3}F_x} \quad , \tag{3.9}$$

whereby the spring constant is defined too (section 3.1.4).

3.1.3 Cantilevers Motion

CONSIDERED EFFECTS IN THE EULER-BERNOULLI BEAM THEORY: Around 1750 a *differential equation of motion of an elastic beam* was for the first time formulated by Daniel Bernoulli, a nephew of Jacob Bernoulli. Leonard Euler accepted the theory in his investigations on this topic. The *Euler-Bernoulli beam theory* - also called classical beam theory - considers the strain energy due to bending and the kinetic energy of lateral displacements. It does not account for effects due to rotation of the cross-section, rotary inertia and shear distortion. Only in 1921 Timoshenko added this effects to the original theory correcting its slight overestimation of the resonance frequencies [111]. However, for slender beams, whose thicknesses, respectively widths are much shorter[4] than the lengths, and with small applied forces leading only to small amplitudes, the new accounted contributions are negligible and Timoshenko's theory converges to the result of Euler and Bernoulli [112].

The result of the two 18th century scientists is expressed in the *Euler-Bernoulli differential beam equation* (eq. (3.14)) below. It can be derived using e.g. either Hamilton's variational principle [111] or the equilibrium of forces and bending moments. In the following, the major steps according to [112] of the latter approach are depicted. In both cases it is assumed that the cross-section over the entire length of the beam as well as area moment of inertia I_y is constant. This is not entirely true for the given cantilevers due do the varying cross-section at the paddle and the mass on the tip.

---

[4]The model of the two Basel scientists holds for long and thin beams where the ratio of length to width, respectively thickness is bigger then ten [114, 115].

EULER-BERNOULLI DIFFERENTIAL BEAM EQUATION: The dynamical behaviour of a cantilever is described by the *displacement function* with the general form $\vec{D}(\vec{r}, t)$. Due to the geometry of the given cantilevers[5] the three-dimensional form can be reduced to the one-dimensional case $X(z, t)$ considering only displacements in x-direction. Further $X(z, t)$ can be separated into two functions, such as

$$X(z, t) = \sum_n u_n(z) x_n(t) \quad , \tag{3.10}$$

where $u_n(z)$ describes the shape of the n-th mode and $x_n(t)$ the time dependence accordingly. We start the derivation by considering the forces acting on a differentially small element with width $\mathrm{d}z$ of a beam with cross-sectional area A and density ρ as shown in fig. 3.2. Firstly, the forces on the two sides of the element at the positions z and $z + \mathrm{d}z$ have to be balanced (eq. (3.11)). And secondly there is no net torque M_{By} on the element (eq. (3.12)). Whereby we find the two equations:

$$F_x(z + \mathrm{d}z) - F_x(z) - \rho A \mathrm{d}z \frac{\partial^2 X(z, t)}{\partial t^2} = 0 \quad , \tag{3.11}$$

$$F_x(z + \mathrm{d}z)\mathrm{d}z + M_{By}(z + \mathrm{d}z) - M_{By}(z) = 0 \quad . \tag{3.12}$$

These equations are expanded in Taylor series about z, where only first order therms are kept. Combined together with eq. (3.6), which relates the change of the curvature to M_{By}, I_y and Young's modulus E, we find the *wave equation*

$$\frac{\partial^2}{\partial z^2} \left(E I_y \frac{\partial^2 X(z, t)}{\partial z^2} \right) = -\rho A \frac{\partial^2 X(z, t)}{\partial t^2} \quad . \tag{3.13}$$

For a homogeneous and prismatic beam where I_y and E are constant[6] this equation can be simplified resulting in the *Euler-Bernoulli differential beam equation*:

$$\boxed{E I_y \frac{\partial^4 X(z, t)}{\partial z^4} + \rho A \frac{\partial^2 X(z, t)}{\partial t^2} = 0} \quad . \tag{3.14}$$

The solutions to this equation describe the *temporal* as well as the *positional behaviour* of the cantilever.

As an aside: It is possible to introduce already at this point the effect of dissipation, by adding the complex valued susceptibility function to E making Young's modulus complex.[7] For clarity we go on for now without losses and complement the temporal

---

[5]Long, thin and relatively wide compared to the thickness.

[6]This is not exactly true for the used cantilevers, which do not have a constant cross-section, e.g. at the paddle, hence I_y is not constant.

[7]This is useful for an analytic consideration of dissipation e.g. by the Zener model also known as the standard linear solid model. Thereby, the imaginary part of the modulus E_I quantifies the contribution

solution with dissipation later on.

The time dependence of the oscillation can be assumed to be harmonic, such as

$$x_n(t) = x_{0,n} \exp(-i\omega_{\mathrm{L}_n} t + i\phi_n) \quad , \tag{3.15}$$

where $x_{0,n}$ are the amplitudes, ω_{L_n} the frequencies and ϕ_n the phase angles of the n modes. Equation (3.14) can now be separated into two ordinary differential equations:

$$\frac{\mathrm{d}^2 x_n(t)}{\mathrm{d}t^2} + \omega_{\mathrm{L}_n}^2 x_n(t) = 0 \quad , \tag{3.16}$$

$$\frac{\mathrm{d}^4 u_n(z)}{\mathrm{d}z^4} - \beta_n^4 u_n(z) = 0 \quad , \tag{3.17}$$

where $\beta_n = (\rho A/EI_y)^{1/4}\omega_{\mathrm{L}_n}^{1/2}$ are the wave-vectors and the equation is the non-linear dispersion relation between β_n and ω_{L_n}. This allows to consider first the *mode shape* and afterwards the *time dependence* individually.

MODE SHAPE: Assuming that the shape is a superposition of complex exponential functions depending on β_n, the general solution of $u_n(z)$ satisfying eq. (3.17) has (in terms of real functions) the form

$$u_n(z) = a_n \cos(\beta_n z) + b_n \sin(\beta_n z) + c_n \cosh(\beta_n z) + d_n \sinh(\beta_n z) \tag{3.18}$$

The boundary conditions for a cantilever with length l are: no deflection and zero curvature at the clamped side and neither force, nor torque acting on the free end, thus:

$$u_n(0) = \frac{\mathrm{d}u_n}{\mathrm{d}z}(0) = \frac{\mathrm{d}^2 u_n}{\mathrm{d}z^2}(l) = \frac{\mathrm{d}^3 u_n}{\mathrm{d}z^3}(l) = 0 \quad . \tag{3.19}$$

This implies for the amplitudes: $a_n = -c_n$ and $b_n = -d_n$, further β_n has to satisfy

$$\cos(\beta_n l)\cosh(\beta_n l) + 1 = 0 \quad . \tag{3.20}$$

Finally the shape of the cantilever's oscillations is given

$$u_n(z) = a_n(\cos(\beta_n z) - \cosh(\beta_n z)) + b_n(\sin(\beta_n z) - \sinh(\beta_n z)) \quad , \tag{3.21}$$

with the numerical values for $\beta_n \cdot l = 1.875,\ 4.694,\ 7.855,\ \dots$ and $a_n/b_n = $ -1.3622, -0.9819, -1.008, $\dots$ found from the boundary conditions. The shape of the first flexural

---

of intrinsic sources of dissipation. The derivation with further references is depicted for example in [116].

mode of a cantilever with l=90 µm normalised to $|u_0(z = l)| = 1$ is thus given by

$$u_0(z) = a_0 \left(\cos(\beta_{0_{90}}z)\right) - \cosh(\beta_{0_{90}}z)) + b_0(\sin(\beta_{0_{90}}z) - \sinh(\beta_{0_{90}}z))$$

with $a_0 = -0.5000$ m, $b_0 = 0.3671$ m and $\beta_{0_{90}} = 2.083 \cdot 10^4$ m^{-1} .   (3.22)

The values of the normalisation constants a_0, b_0 are independent of l and can be calculated from eq. (3.21), $\beta_n \cdot l = 1.875$, $^{a_a}/_{b_n} = -1.3622$ and $|u_0(z = l)| = 1$. For $\beta_{0_{90}}$, the length of the cantilever is set to $l = 90 \cdot 10^{-6}$ m.

TEMPORAL SOLUTION - LANGEVIN EQUATION: Equation (3.16) describes the temporal behaviour of a cantilever in absence of friction and without any external driving. From the dispersion relation

$$EI_y\beta_n^4 = \rho A\omega_{\mathrm{L}n}^2 \tag{3.23}$$

tying the eqs. (3.16) and (3.17) together and by determining β_n from the boundary conditions the *cantilever's frequencies* for a distinct material and geometry are given:

$$\omega_{\mathrm{L}n} = \sqrt{\frac{Ed^2\beta_n^4}{12\rho l^4}} \quad , \tag{3.24}$$

whereas still $I_y = wd^3/12$ as in the static displacement. Although this calculation does not directly apply to the cantilevers used and described in this work. Mainly it does not take into account the additional mass at the tip, resulting in a more then twice as high frequency compared to mass-loaded cantilevers. The mechanics of such levers with non-uniform cross-section is best studied through a finite element model matching the experimental results [117].

In the following only the fundamental mode $x_{n=0}(t) \equiv x(t)$ is regarded. Its resonance frequency is still denoted as ω_{L_0}.

Since eventually forces act on the cantilever, it is convenient to multiply the position-depending part of the Euler-Bernoulli equation (eq. (3.16)) with an inertial mass m obtaining the *frictionless equation of motion*

$$m\ddot{x}(t) + m\omega_{\mathrm{L}_0}^2 x(t) = 0 \quad , \tag{3.25}$$

where the summands are forces with unit [N]. The two dots denote the second time-derivative of x. The introduced mass is the *effective motional mass* of the system, often denoted as m_{eff}, which is different than the gravitational mass. In fact, for a cantilever the effective mass is one-fourth of the gravitational mass [117, 118]. For simplicity only $m \equiv m_{\mathrm{eff}}$ is used in this work. Equation (3.25) can also be obtained without the Euler-Bernoulli equation, by considering a system of an inertial mass m in a conservative potential $U(x)$ with a local minimum at $x = 0$ [112]. The solution to the friction less

equation of motion is as already assumed

$$x(t) = x_0 \exp(-i\omega_{\mathrm{L}_0} t + i\phi) \quad , \tag{3.26}$$

whereas x_0 is the amplitude and ϕ the phase angle determined by the initial conditions. The minus sign is taken by convention.

Coupling the oscillator to its environment and including dissipation and noise is expressed by adding a corresponding force term F_{env} on the right hand side of eq. (3.25). This environmental force can be separated into a dissipative term which is proportional to the velocity $\mathrm{d}x/\mathrm{d}t$ and a random thermal noise term F_{th}, such as

$$F_{\mathrm{env}} = m\gamma_0 \mathrm{d}x/\mathrm{d}t + F_{th} \quad . \tag{3.27}$$

The dissipation is quantified by the constant γ_0 relating the rate of dissipation to the velocity. This yields the *Langevin equation* describing the lossy and noisy harmonic oscillator:

$$\boxed{m\ddot{x}(t) + m\gamma_0 \dot{x}(t) + m\omega_{\mathrm{L}_0}^2 x(t) = F_{th}(t)} \quad . \tag{3.28}$$

An alternate form is to express the dissipation including the mass as $\Gamma_0 = m\gamma_0$ and to introduce the spring constant $k = m\omega_{\mathrm{L}_0}^2$ into the above equation:

$$\boxed{m\ddot{x}(t) + \Gamma_0 \dot{x}(t) + kx(t) = F_{th}(t)} \quad . \tag{3.29}$$

C-FACTOR: In general, the displacement of the cantilever can not always be measured at the same location where the force is acting on it. In the here described work, the force acts on the very end of the cantilever, at $z = l$, where the sample is attached. But the displacement is measured at the paddle, $\sim 15\,\mu\mathrm{m}$ above the tip, where the laser is aimed on (see fig. 3.1). The so called *c-factor* taking this difference into account, is defined as

$$c := u_0(z = l)/u_0(z_{\mathrm{paddle}}) \quad , \tag{3.30}$$

where z_{paddle} is the position of the paddle measured from the base of the cantilever.

From eq. (3.22) the c-factor can be calculated for each different set of l and z_{paddle} according to

$$\boxed{c = \frac{1}{0.5(\cosh(\xi) - \cos(\xi)) + 0.3671(\sin(\xi) - \sinh(\xi))}} \tag{3.31}$$

$$\text{with} \quad \xi := 1.875 \cdot \frac{z_{\mathrm{paddle}}}{l} \quad .$$

For a 90 μm long cantilever this gives the numerical value of $c = 1.297$.

Experimentally c is considered in the transduction coefficient α_t (eq. (3.65)).

3.1.4 Spring Constant

With Hooke's law $F = kx$ the spring constant k can be calculated straight forwardly from the static displacement derived in eq. (3.9):

$$k = \frac{Ewd^3}{4l^3} \quad . \tag{3.32}$$

One could argue that the static displacement is not as accurate as the derivation based on the dynamical approach. Though, using the frequency given through the dispersion relation of the Euler-Bernoulli equation (eq. (3.24)), considering that $k = m\omega_{\mathrm{L}_0}^2$ and that for a cantilever the effective mass is reduced, $m = 1/4\rho wdl$ [117, 118], yields to an only very slightly stiffer spring constant

$$k_{\mathrm{dyn}} \cong 1.03 \cdot \frac{Ewd^3}{4l^3} \quad . \tag{3.33}$$

However, looking at the spring constant as measure for the sensitivity of the force transducer, $F = kx$ does not take into account the resonant character of the cantilever. Which is in fact the basic reason of using a cantilever at all. Through the resonance, the sensitivity is indeed increased by several orders of magnitude as shown below in section 3.1.6.

Experimentally k is determined by measurements of the thermal noise, as carried out in more detail in section 3.1.7. From the fluctuation-dissipation theorem (eq. (3.53)) k can be written in terms of measurable quantities as

$$k = \frac{\pi S_F Q f_{\mathrm{L}_0}}{2k_B T} \quad , \tag{3.34}$$

whereas S_F is the spectral density of the thermal noise force, Q the quality factor, f_{L_0} the cantilevers resonance frequency, k_B the Boltzmann constant and T the temperature of the cantilevers mode in equilibrium with its environment. Q is determined by ring-down measurements as carried out in section 4.2.1 and T by a 4-wire resistance temperature sensor.

3.1.5 Dissipation Mechanisms

OVERVIEW: Dealing with measurements of tiniest, lowest possible forces inevitably gives a central role to the reduction of noise and the amplification of the signal. Due to its geometry a cantilever is a resonator: driven by an external force it oscillates with a greater amplitude at specific preferential frequencies, i.e. the natural frequency ω_{L_0} and its overtones. However, the stored kinetic energy of this modes also gets reduced by entropic processes, it dissipates, quantified by the dissipation rate γ_0. There is a variety of different mechanisms which contribute to dissipation. The energy can be transferred

by phonons out of the resonator, transferred into other modes in non-linear systems, converted to other non kinetic forms of energy or lost to the thermal bath as heat.

The following paragraphs give the definition of the quality factor Q and a selected overview of the relevant dissipation mechanisms. For a more detailed description including other dissipation mechanisms, the reader is pointed to the extensive report *Dissipation in Nanoelectromechanical Systems* [116], which builds the footing for these paragraphs. For some of the mechanisms (e.g. damping by air Q_{LPG}^{-1}), the strict suppression is well established, but still absolutely mandatory to implement, giving the reason to discuss them too. The reduction of the remaining is crucial to achieve highest sensitivity. And it is moreover one of the toe-holds for further improvement of MRFM.

Dissipation mechanisms can be split up into two categories: *intrinsic dissipation*, where the energy gets lost within the resonator itself. Namely relevant for the deployed cantilevers are here *surface losses* Q_{SL}^{-1}, *thermoelastic dissipation* Q_{TED}^{-1} and, potentially, *mechanical defects* Q_{MD}^{-1}. To the second category belong mechanisms of *extrinsic dissipation* like *clamping losses* Q_{CL}^{-1}, dissipation by a the surrounding medium, in this case it is: *gas at low pressure* Q_{LPG}^{-1}, and last but certainly not least, *non-contact friction* Q_{NCF}^{-1}.

QUALITY FACTOR: Dissipation is the measure of how fast a (mechanical) oscillator loses its stored (kinetic) energy E_{kin}. In its most general form dissipation Q^{-1} is written as

$$Q^{-1} = \frac{\Delta E_{\text{kin}}}{2\pi E_{\text{kin}}} \quad , \tag{3.35}$$

where ΔE_{kin} is the energy loss per cycle of oscillation and E_{kin} the total stored energy. The definition of energy loss *per radian* over the total energy is by convenience. It introduces the factor of 2π here and thereby it is omitted in equations involving the frequency which are more often used.

By solving the Langevin equation (eq. (3.29)) of the damped oscillator one obtains the expression for Q^{-1} based on the rate of dissipation γ_0 and the resonance frequency ω_{L_0}, or based on the intrinsic dissipation $\Gamma_0 = {}^{m\gamma_0}/_{\omega_{\text{L}_0}}$ [112]. For small damping $\gamma_0 \ll \omega_{\text{L}_0}$, it can be approximated and finally be written depending on ω_{FWHM}, the full-width-at-half-maximum (FWHM) of a Lorentzian fit to the spectral density:

$$Q^{-1} = \frac{\gamma_0}{\sqrt{\omega_{\text{L}_0}^2 - \gamma_0^2/4}} \cong \frac{\gamma_0}{\omega_{\text{L}_0}} = \frac{\Gamma_0}{m\omega_{\text{L}_0}} = \frac{\omega_{\text{FWHM}}}{\omega_{\text{L}_0}} \quad . \tag{3.36}$$

The transformations are valid for low dissipation ($Q > 100$) and linear response, which applies to the used cantilevers.

The overall quality factor of a resonator in the linear regime is defined as the sum of

the inverse of each uncorrelated drain channel contributing to the dissipation

$$Q = \frac{1}{Q_{\text{CL}}^{-1} + Q_{\text{SL}}^{-1} + Q_{\text{NCF}}^{-1} + Q_{\text{LPG}}^{-1} + Q_{\text{TED}}^{-1} + Q_{\text{MD}}^{-1} + \dots} \quad . \tag{3.37}$$

SURFACE LOSSES Q_{SL}^{-1} are the most dominant source of dissipation for the deployed cantilevers.

Whereas in macroscopic structures bulk properties dominate the intrinsic dissipation and surface effects are negligible, for nanoscale structures this does not hold any more. With shrinking dimensions the surface-to-volume ratio is growing, bulk processes related to the volume are reduced and surface losses eventually become dominant.

Surfaces contain a large amount of defects due to the abrupt termination and exposure to the environment. Free dangling bonds can build oxides as well as attract and permanently fix absorbates. Especially in top-down manufactured structures the crystal termination is not atomically smooth and potentially spoiled with chemical agents from the etching process. The defects on the atomically rough, impure surface form additional energy reservoirs and mediate anharmonic mode coupling which contributes significantly to damping. For a quantitative measure, surface dissipation can be calculated according to the equation below. The two parameters of the surface layer, the thickness δ and the imaginary part of the complex Young's modulus[8] E_I^S, are difficult to predict theoretically [116] and have to be determined experimentally for the specific object. For very thin beams ($d \ll w$), one sees that Q_{SL} is proportional to the cantilever thickness d, emphasising the importance of this dissipation mechanism for sensitive cantilevers (remember $k \propto d^3$) [116]:

$$Q_{\text{SL}}^{-1} = \frac{2\delta(3w + d)}{wd} \frac{E_I^S}{E} \approx 6\frac{\delta}{d}\frac{E_I^S}{E} \quad . \tag{3.38}$$

As material for nano-mechanical resonators often silicon is chosen. It is available in very pure quality, exhibits thereby little intrinsic dissipation and it can be easily processed in various forms. Tough when silicon is exposed to air, a $\sim 1-2$ nm thick, heterogeneous, amorphous oxide layer is formed, consisting of SiO_2 as well as other oxides.

The quality (E_I^S) of this native layer can be improved by *annealing* the structure at 500 to 800 °C in UHV. Thereby the quality factor can be enhanced by a factor of 10 to 100 as shown for Si cantilevers of different manufacturers by Rast et al. [119]. This procedure has also been tested for the cantilevers used in this work.[9] The downside is, that the enhancement is not durable. Exposed to air a new oxide layer is formed, setting

---

[8]By adding the complex susceptibility function to the Young's modulus, material related dissipation can be described quantitatively as it is done in the Zener model. See e.g. [116] for an overview and further references.

[9]The experiments have been made by Lucas Moser, Master student in the Poggiolab, Universität Basel

back the improvement. In principle it is possible to anneal the cantilever without breaking the vacuum before the subsequent measurements and it is indeed implemented in certain experimental apparatuses.[10] Since other components of the measurement system are often not suited to such high temperatures, it involves higher practical demands as e.g. the separation of the annealing area from the measurement area. Further it remains questionable if the sample itself or the attachment of the sample to the cantilever will hold the thermal load.

For the used cantilevers in this work, methods to permanently reduce Q_{SL}^{-1} have been studied by Tao et al. [40]. The idea thereby is to *controllably terminate the surface*, so that the native oxide can not be formed when exposed to ambient conditions. The most successful of several investigated processes is to etch away the native oxide and terminate the surface by a gas-phase thermal hydrosilylation with organic molecules. At cryogenic temperature an improvement in Q of a factor 4.3 from $\sim$ 60'000 to 260'000 was achieved.

Other ways to improve Q_{LS} are to use different materials, more inert than silicon (*diamond cantilevers*, see section 1.4.3, [69]), or to manufacture the resonator in a bottom-up instead of a top-down manner: Grown *nanowires* exhibit a more homogeneous crystalline structure and fewer other defects at the surface than etched cantilevers (see section 1.4.3, [74, 75]).

CLAMPING LOSSES Q_{CL}^{-1} occur due to concentrated strain at the base of the cantilever. The vibrating shear force and bending moment at the attachment point acts as an excitation source of *elastic waves propagating into the substrate* of the cantilever chip. Quantitatively the clamping losses can be estimated according to [41, 120]

$$Q_{CL}^{-1} \approx \frac{1}{2.17} \left(\frac{d}{l} \right)^3 \quad . \tag{3.39}$$

For ultra-thin and long cantilevers, e.g. $d = 100$ nm and $l = 90$ μm, this results in $Q_{CL} > 10^9$.

The effect can even be reduced by adding an additional mass on top of the base during the manufacturing process, as it is the case for the used levers. By making the base of the cantilever thicker and thereby making the clamping harder the radiation to the substrate is reduced even more.

NON-CONTACT FRICTION Q_{NCF}^{-1} occurs due to the interaction of two closely separated objects. Its mechanisms are still subject of ongoing discussion, since theoretical predictions [121, 122] and experimental observations [119, 123–130] differ sometimes by orders of magnitude [131]. Q_{NCF}^{-1} can even be used as measurement observable as in non-contact friction microscopy [132, 133]. In general, the main origins of non-contact

---

[10]As for example in the group of Ernst Meyer, Universität Basel.

friction are *Joule dissipation*, *van der Waals friction* and *phononic friction*, whereas the two latter become only relevant at closer separations than in our case. Joule dissipation origins in electrostatic forces which arise from permanent or fluctuating charges situated on the cantilever's tip or/and the surface. The charge induced on the other surface follows the tip's motion and experiences a resistive loss [134].

The distance dependence of Q_{NCF}^{-1} on the separation d_{sep} follows a power law

$$Q_{NCF}^{-1} \propto d_{sep}^{-n} \quad , \tag{3.40}$$

where the exponent n depends on the geometry of the cantilever's tip, the material composition of the objects (dielectric, conductor) and the nature of the friction. Experimental observations for a cantilever in pendulum geometry with a Au coated tip over a thin film of Au yield $n = 1.3$ [128], which is in good agreement with the theoretical model resulting in $n = 1.5$ [121, 122]. Similar experiments, though with a SmCo tip over an Au surface yield an exponent of $n = 0.5$ [119].

Non-contact friction can be minimised by equilibrating the surface potentials of the two objects and by the choice of the surface material. Q_{NCF}^{-1} dominated by Joule dissipation exhibits a parabolic characteristic depending on the bias voltage V_{bias} between cantilever and surface.[11] Stipe at al. approximated their results with

$$Q_{NCF}^{-1} = \xi(T) \frac{V_{bias}^2 + V_0^2}{d_{sep}^{-1.3}} \quad , \tag{3.41}$$

whereas $\xi(T)$ characterises the temperature dependence and V_0 corresponds to the minimal friction at zero bias [128]. The electrostatic normal force, which alters f_{L_0}, follows a parabolic behaviour as well, whereas the minima occur at the same V_0. This enables to minimise Q_{NCF}^{-1} by tuning $f_{L_0}(V_{bias})$ to its lowest value. The second, parallel approach is, to choose a high purity conducting material for the two objects as done by covering the cantilever's tip with an thin AU film.

For our ultra-soft cantilevers, non-contact friction becomes significantly contributing at separations $\lesssim 50$ nm, where Q_{NCF}^{-1} becomes larger than the internal friction of the cantilever. Since in the present MRFM setup the wanted, highest magnetic field gradients $\vec{G}$ are found closest to the nano-magnet, Q_{NCF}^{-1} is eventually *the* dominant dissipation mechanism.

DISSIPATION BY GAS AT LOW PRESSURE Q_{LPG}^{-1}:   In order to reduce *dissipation by the surrounding medium*, the microscope operates in ultra-high vacuum (UHV). In this regime, the mean free path of the remaining gas molecules (1 km -10^5 km) is much bigger than the cantilever dimensions and the particles do not interact with each other. The dissipation is only due to the momentum transfer between individual molecules and

---

[11]The parabolic dependence does not apply generally for Q_{NCF}^{-1}. E.g. van der Waals friction exhibits a V^4 dependence [121, 122].

the cantilever. It can be calculated according to [116, 135]

$$Q_{\mathrm{LPG}}^{-1} = \left(\frac{2}{\pi}\right)^{2/3} \frac{1}{\rho d f_0} \frac{p}{\sqrt{k_B T/m_g}} \quad , \tag{3.42}$$

where $f_0 = 2\pi\omega_{\mathrm{L}_0}$, p is the pressure, k_B the Boltzmann constant, T the temperature and m_g the mass of the gas molecules.

The crossover from the Q_{LPG}^{-1} regime to viscous damping depends on the pressure p and the dimensions of the resonator. The border is approximately determined as $p_{\mathrm{crossover}} \approx 0.034[\mathrm{N/m}]/w$. This results for the given cantilevers in $p_{\mathrm{crossover}} \approx 85.0$ mbar, below which dissipation by a low pressure gas applies [135].

The contribution of Q_{LPG}^{-1} is relevant to the total dissipation above a pressure of $p \approx 10^{-7}$ mbar, at which for cryogenic temperatures $Q_{\mathrm{LPG}} \approx 300'000$. At room temperature it already becomes negligible an order of magnitude earlier. The boundaries for the region where Q_{LPG}^{-1} applies, respectively matters are experimentally confirmed by Yang et al. [42].

THERMOELASTIC DISSIPATION Q_{TED}^{-1} occurs due to phonon-phonon interactions resulting from the *scattering of acoustic phonons with thermal phonons*. Thereby the mechanical energy is converted to heat and conducted out of the cantilever to the substrate. The damping mechanism depends on the material of the resonator, its dimensions and on temperature. It is described by several authors, e.g. started by Zener [136] and further developed by Lifshitz and Roukes [137], leading to slightly different estimations for Q_{TED}^{-1}.

In general Q_{TED}^{-1} scales with the system size and is reduced in smaller systems. Although it is possible that, depending on the aspect ratio and material properties of the resonator, thermoelastic dissipation contributes significantly also at the nanoscale [116]. It is investigated for comparable cantilevers in [42] with the conclusion that for the given very long and thin cantilevers Q_{TED}^{-1} is negligible, e.g. $Q_{\mathrm{TED}} > 10^7$ at room temperature and even $Q_{\mathrm{TED}} > 10^9$ at 4 K [42, 116].

DISSIPATION DUE TO MATERIAL DEFECTS Q_{MD}^{-1}: Defects in the crystal structure such as substitutional impurities (*doping* atoms), *interstitial motion* and *grain boundary sliding* are contributing to dissipation, as the defects reconfigure between equilibrium and metastable states in the dynamic field. Q_{MD}^{-1} follows a power law dependence on temperature since the defect sites need an activation energy which is typically in the order of 10 K or higher. Below the activation energy the contribution to dissipation is constant.

The strategy to minimise Q_{MD}^{-1} is simple: high quality material is mandatory to build excellent resonators. This is indeed the case for the used cantilevers and Q_{MD}^{-1} can be assumed to be minimal as well as not relevantly contributing.

3.1.6 Resonant Enhancement by the Quality Factor

The static displacement caused by a force acting on the cantilever was derived in section 3.1.2. And in section 3.1.3, the cantilever's spring constant based on geometry and material was discussed. However, the *resonant enhancement of the force's transduction into a displacement* has not yet been quantified.

We recall the Langevin equation (eq. (3.28)) and write it in terms of Q, approximated for small damping (eq. (3.36)), as well as of a total force $F(t) = F_{\text{th}}(t) + F_x(t)$ driving it. $F_x(t)$ is thereby the force caused by the spin inversion (section 4.1.3):

$$m\ddot{x}(t) + m\frac{\omega_{\text{L}_0}}{Q}\dot{x}(t) + m\omega_{\text{L}_0}^2 x(t) = F(t) \quad . \tag{3.43}$$

The Fourier transform of this equation is

$$-\left(m\omega^2 - i\frac{m\omega\omega_{\text{L}_0}}{Q} - m\omega_{\text{L}_0}^2\right)\hat{x}(\omega) = \hat{F}(\omega) \quad , \tag{3.44}$$

which on resonance $\omega = \omega_{\text{L}_0}$ simplifies to

$$i\frac{m\omega_{\text{L}_0}^2}{Q}\hat{x}(\omega_{\text{L}_0}) = \hat{F}(\omega_{\text{L}_0}) \quad . \tag{3.45}$$

Transformed back to the time-domain we get

$$F(t)\big|_{\omega=\omega_{\text{L}_0}} = i\frac{m\omega_{\text{L}_0}^2}{Q}x(t) \tag{3.46}$$

and in real values with the spring constant $k = m\omega_{\text{L}_0}^2$

$$F(t)\big|_{\omega=\omega_{\text{L}_0}} = \frac{k}{Q}x(t) \quad . \tag{3.47}$$

Comparing the last equation to Hooke's law $F = kx$, we see that the transduction to the displacement is enhanced by the factor Q.

3.1.7 Signal to Noise Ratio

SIGNAL: In the end, the measured signal is that part of the cantilever's displacement $x(t)$ which is caused by the magnetic force $F_x \propto M_z$, respectively its standard deviation $\sigma_{F_x} \propto \sigma_{M_z}$, whereas M_z is the measurement ensemble's magnetisation and σ_{M_z} its standard deviation. Therefore, the spins are inverted twice per cantilever period so that the cyclic spin signal exhibits the same frequency f_{L_0} as the cantilever and drives it (see sections 4.1.2 to 4.1.4 and eqs. (4.3), (4.4) and (4.8)). Figuratively spoken, the magnetic force's peak sits on top of the Lorentzian peak of the cantilever's thermal

motion in the spectral density plot, as shown in fig. 4.2b. In order to increase the minimal measurement bandwidth $\Delta f_{BW_{min}}$ the motion of the cantilever is damped, whereby the spectral density distribution is broadened as explained in section 4.2.1.

NOISE $\rightarrow$ POWER SPECTRAL DENSITY: The characteristics of the measurement system's noise are described by the spectral density. As derived in section 3.1.3 the time dependence of an oscillating cantilever is described by the Langevin equation

$$m\ddot{x}(t) + m\gamma_0\dot{x}(t) + m\omega_{L_0}^2 x(t) = F_{th}(t) \quad , \tag{3.48}$$

whereas the coupling to the environment is separated in the velocity dependent dissipation term $m\gamma_0\dot{x}(t)$ (examined in section 3.1.5) and the random thermal noise term $F_{th}(t)$, with zero statistical average $\langle F_{th}(t)\rangle = 0$. It is this noise term through which the thermal equilibrium of the cantilever with its environment is established. The *equipartition theorem* thereby relates kinetic, potential and thermal energy of such a system [112, 138, 139]:

$$\frac{1}{2}m\langle \dot{x}^2\rangle = \frac{1}{2}k\langle x^2\rangle = \frac{1}{2}k_B T \quad . \tag{3.49}$$

How the noise intensity for a time-dependent signal is distributed over a frequency range is described by the *(power) spectral density* $S(\omega)$. The double-sided spectral density $S_{x_D}(\omega)$ of a displacement $x(t)$ is defined as [140]

$$S_{x_D} = \lim_{\tau\to\infty}\langle |\hat{x}_\tau(\omega)|^2\rangle \quad , \tag{3.50}$$

whereas $\hat{x}_t(\omega)$ is the truncated Fourier transform of the displacement $x(t)$ for a finite time window:

$$\hat{x}_\tau(\omega) = \frac{1}{\sqrt{\tau}}\int_{-\tau/2}^{+\tau/2} x(t)e^{i\omega t}\mathrm{d}t \quad . \tag{3.51}$$

As carried out by several authors [117, 118, 140], the mean-square amplitude of the displacement for a time window much longer than the oscillation period for the single-sided convention[12] of $S(\omega)$ is

$$\langle x^2\rangle = \frac{Q}{4\omega_{L_0}^3 m^2}S_F \quad , \tag{3.52}$$

whereas S_F is the *spectral density of the thermal noise force*, which is independent of ω in the region of interest.

---

[12]The double-sided spectral density of the displacement $S_{x_D}(\omega)$ spans over positive as well as negative frequencies and can not be fit directly to physical data. It is related to the single-sided spectral density $S_x(\omega)$ by $S_x(\omega) = 2S_{x_D}(\omega)$ [118].

With the equipartition theorem, eq. (3.49), the white S_F is determined as [118]:

$$S_F = \frac{4k_BTm\omega_{L_0}}{Q} = \frac{4k_BTk}{\omega_{L_0}Q} = 4k_BT\Gamma_0 \quad . \tag{3.53}$$

Such a result is known as *fluctuation-dissipation theorem.* It has a general validity for systems governed by a Langevin equation [112, 117].

Finally, the single-sided *spectral density of the displacement* in terms of the measurable quantities f, f_{L_0}, Q, T and k is [118]:

$$S_x(f) = \frac{2k_BTf_{L_0}^3}{\pi kQ\left(\left(f^2 - f_{L_0}^2\right)^2 + (ff_{L_0}/Q)^2\right)} \quad . \tag{3.54}$$

In the whole displacement detection setup other noise sources also add to $S_x(f)$. Assuming that further displacement noise S_{x_N} before and of the photodetector itself as well as electronic noise S_{V_N} afterwards are white, the *measured spectral density* in units of V^2/Hz is [117, 118]

$$S_V(f) = S_{V_N} + \alpha_t^2\left(S_{x_N} + S_x(f)\right) \quad , \tag{3.55}$$

whereas α_t is a transduction coefficient in units of V/m. In principal, it can be determined by fitting the physically measured spectral density using the eqs. (3.54) and (3.55). In our case however α_t is rather determined by tuning of the interferometer as described in section 3.7.1 and eq. (3.65).

FORCE SENSITIVITY: The minimal measurable force $F_{\min}$ is given by the spectral force density S_F multiplied with the measurement bandwidth Δf_{BW}:

$$F_{\min} = \sqrt{4k_BT\Gamma_0\Delta\omega_{BW}} = \sqrt{2k_BT\frac{k}{\pi Qf_{L_0}}\Delta f_{BW}} \quad . \tag{3.56}$$

For the present setup[13] it is $F_{\min} = 1.7$ aN.

In practise, $F_{\min}$ is raised by S_{x_N} and S_{V_N}, although the contribution of the latter is negligible ($S_{V_N} \ll S_{x_N}\alpha_t^2$). The experimentally minimal measurable force $F_{\min}^{\exp}$ can be obtained from the measured spectral density $S_V(f)$, as carried out in appendix A.2:

$$F_{\min}^{\exp} \cong \frac{k}{Q}\sqrt{\frac{S_V(f_{L_0}) - S_{V_{\text{floor}}}}{\alpha_t^2}\Delta f_{BW}} \quad . \tag{3.57}$$

Thereby, the spring constant k, the (squared) peak voltage $S_V(f_{L_0})$ and the noise floor

---

[13]$T = 4.4$ K, $k = 75$ µN/m, $Q = 3.1 \cdot 10^4$, $f_{L_0} = 3.1$ kHz, $\Delta f_{BW} = 0.1$ Hz
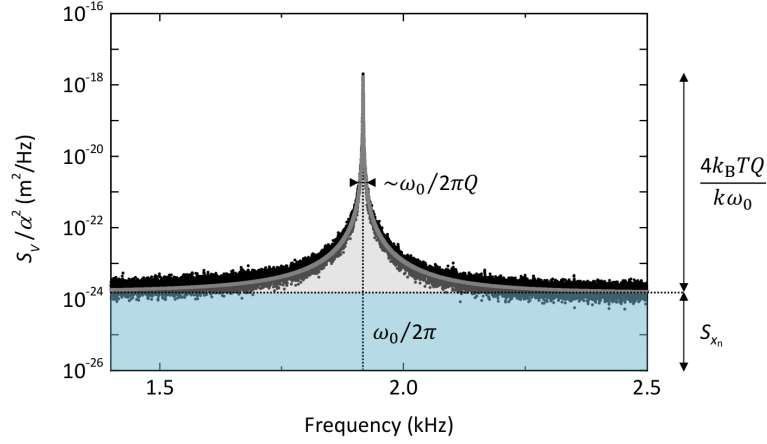
FIGURE 3.3: THERMAL NOISE SPECTRAL DENSITY
The black dots depict the spectrum of a cantilever's fundamental mode, measured with a fibre-optic interferometer. The grey curve fits the experimental data according to eqs. (3.54) and (3.55). The grey area included between the fit and the noise floor $S_{V_{\text{floor}}} \approx S_{x_N}$ is proportional to $1/k$ which enables its calculation for known values of T, Q and ω_{L_0}. $T = 4.2$ K and $p < 10^{-6}$ mbar, $k = 100$ μN/m and Q = 10^4. Figure taken from [117].

$S_{V_{\text{floor}}}$ far away from resonance can be extracted from the measured spectrum, Q is determined by the ring-down method (section 4.2.1) and α_t by the interferometer tuning (section 3.7.1).

SIGNAL TO NOISE RATIO: Finally, the theoretical SNR is given by the ratio of the magnetic force F_x (eq. (4.3)) to the minimal measurable force F_{min} (eq. (3.57)):

$$SNR_{\text{th}} = \left(\frac{F_x}{F_{\text{min}}} \right)^2 = N \frac{(\mu_z G_{zx})^2}{S_F \Delta \omega_{\text{BW}}} = N \frac{(\mu_z G_{zx})^2}{4 k_B T \Gamma_0 \Delta \omega_{\text{BW}}} \quad . \tag{3.58}$$

The experimental SNR is the comparison of the signal measured by the lock-in amplifier and its error as described in section 4.1.4 and eq. (4.7).

3.2 Sample Preparation

Contemplable samples for MRFM are restricted in mass and size to the order of a few micrometres. On one side, because of the delicate cantilever. On the other side, since in this particular setup, the investigated spins have to be as close as possible to the nano-magnet to reach a high sensitivity.

The nano- to micro-metre scale of the samples makes it everything but trivial to attach them to the cantilever. It is indeed challenging to mount e.g. nanowires and splitters of

CaF or KPF_6 crystals on its tip. The samples are attached under an optical microscope on a vibration isolation table using glass needles which are operated by micro-manipulators. The procedure is explained in detail and richly illustrated, in Weber's dissertation [141]. The main steps are listed in the following:

- The cantilever chip is clamped onto a holder particularly designed for the e-beam evaporation in the end.

- In a first step, UHV compatible, not out-gassing two-component glue (G1) is deposited with a glass needle at the very tip of the cantilever.

    - The glass needles are fabricated individually by pulling a glass capillary while heating it. Thereby, fine and clean tips with a radius of curvature of 200 nm are produced, suitable to handle the small objects.

- In a second step, the sample is unhinged from the substrate, picked up, orientated and placed with new, clean needles.

- Under ambient conditions the glue is dried for approximately 24 hours and the rigid attachment is checked afterwards.

Such objects with high surface to volume, respectively surface to mass relations, exhibit huge van der Waals forces, which can hinder a controlled handling. It is therefore necessary to irradiate the objects with α-particles during all steps. It frees trapped electric charges on the surfaces and reduces electrostatic interaction.

- Finally a ~ 10 nm thin layer of gold with a ~ 5 nm thin sticking layer (Si) is evaporated at the very tip in order to reduce non-contact friction.
  The evaporation-holder is equipped with a razor blade that is pushed against the cantilever close to the tip. It covers the shaft of the cantilever from the evaporation beam so only the tip gets coated. Spoiling the shaft would disable the cantilever, as it would bend at low pressure and cryogenic temperature.

Liquid samples like e.g. dissolved stearic acid are attached by repeatedly dipping the cantilever's tip into the solution and letting it dry.

3.3 Magnetic Pulse Generation

This section covers the process of the pulse's *design and generation* on the computer, the *heterodyning*, *amplification*, *filtering*, *splitting* and *biasing*, before the pules are applied to the micro-wire (section 3.4). Figure 3.4 shows the schematic of the whole wiring setup. The theory of the ARP pulse design is explained in section 2.2 and the practical approach in sections 4.1 and 4.3.
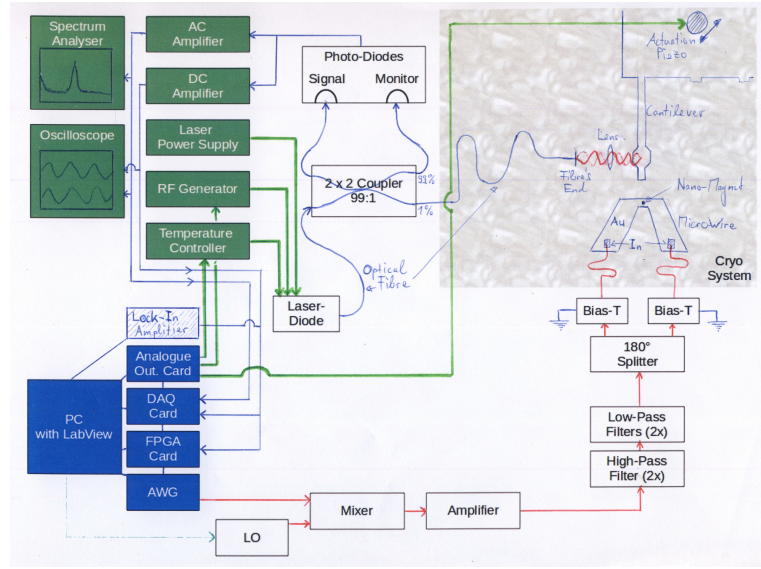
FIGURE 3.4: APARATUS' CABELING FOR CONTROL AND READ-OUT
From a personal computer equipped with PXI extension cards the experiments are piloted (in blue). The instruments of the control racks (in green) are controlled via analogue outputs. The ARP pulses are generated with an AWG and finally emitted by a micro-wire (bottom lower and lower-right part). The cantilever's displacement is measured with a laser fibre interferometer including a 2×2-coupler, converted by a photodiode to a voltage and recorded with the PC.

WAVEFORM AND TRIGGER GENERATION: The ARP pulses are designed by LabView and generated with a corresponding arbitrary waveform generator (AWG) (NI PXIe-5451 or NI PXI-5421). The AWG is installed in a PXI chassis (NI PXIe-1082) which communicates internally and to the computer via a remote control card (PXIe-8375) and PCI buses.

Based on the input parameters[14] (f_{centre}, Δf_{mod}, β_{HS}), the cantilever frequency f_{L_0} and the AWG sampling rate $f_{\text{AWG-sampling}}$, the normalised discrete values of the amplitude of one ARP pulse are calculated. A digital wave-form with eight consecutive ARP pulses is created by LabView as input for the AWG. Finally, the *wave-form* is sent to the AWG together with the pulse's effective amplitude and the AWG is set to send a *trigger* on a separate channel every eight ARP pulses. The main output of the AWG is connected to the micro-wire lead and the trigger output is fed into the lock-in amplifier.

Sending a sequence of eight pulses to the AWG is done for better performance of the pulse generation. Solely out of convenience the trigger is set to the same number. For the detection, the lock-in amplifier is set up accordingly, i.e. receiving the trigger every four cantilever cycles.

---

[14]see section 4.1

HETERODYNING: *Measuring spins* with a high gyromagnetic ratio at high fields results in a f_{res} *exceeding the AWG's maximal output frequency* $f_{\text{AWG-max}}$.[15] The AWG's limit is given by the Nyquist–Shannon sampling theorem: $f_{\text{AWG-max}} < 1/2 \cdot f_{\text{AWG-sampling}}$.

In such cases, the AWG's output is heterodyned: it is multiplied by an RF-mixer (Mini-Circuits ZLW-1H) with a local oscillator (LO), i.e. a constant sine wave with f_{LO}. The LO is generated by an unspecific waveform generator. Accordingly, the frequency set for the pulse generation in LabView is given by $f_{\text{centre}} - f_{\text{LO}}$.

When implementing heterodyning, it is assured that the inputs of the mixer (the AWG's output and the LO) have the same power and that the undesired heterodyne (the difference of the two inputs) is filtered out.

AMPLIFICATION: The AWG's maximum output voltage is not sufficient to generate a high enough B_1, especially since it is slightly damped by the subsequent filtering. Therefore the signal is amplified with a RF-amplifier (Mini-Circuits ZHL-1-2W-S+).

FILTERING: The generated signal includes disturbing noise at other frequencies than f_{RF}. With a series of low- and high-pass filters these components are suppressed.

SPLITTING: For optimal driving of the spin inversion and minimal spurious excitation of the cantilever, the micro-wire is driven differentially [142]. Therefore the signal is split by a 180 ° phase shift power splitter (Mini-Circuits ZFSCJ-2-1-S) and the two output leads are fed into the micro-wire. This results in a *standing electromagnetic wave* inside the closed loop formed by the leads and the micro-wire. With equally long leads from the spitter to the micro-wire chip, a *voltage node* and a *current anti-node* are located exactly at the centre of the micro-wire. The magnetic field is thus maximal and the electric field is minimal at the sample position. Thereby the spin driving is optimal without driving the cantilever by electric fields.

AWGs often exhibit an second, inverted output channel, wherewith the splitter could be replaced. Tests by the research group of R. Budakian, University of Illinois, however showed, that the thereby achieved phase shift is not as good as needed for MRFM.

Aside from the length of the leads, also the impedance has to be the same in both of arms. This applies in particular to the In-bonding connections to the micro-wire (see section 3.4).

UN-FLOATING: The AWG's output is not explicitly referenced to the chassis ground - it is floating. The mean value of the pulses and thereby also the mean potential of the micro-wire are thus not fixed to 0 V. Therefore both micro-wire leads are *biased* to the ground shield of the coaxial cables by bias tees (Mini-Circuits ZFBT-4R2G+).

---

[15]E.g. $\gamma_{\text{H}} = 42.576 \cdot 2\pi$ MHz/T, $B_0 = 6$ T, $f_{\text{AWG-sampling}} = 400$ MHz
$\Rightarrow\quad f_{\text{res}} = 255$ MHz $> 1/2 \cdot f_{\text{AWG-sampling}}$.

REMARKS:

- Due to its small dimensions the micro-wire can only take a very low maximal current before it fuses. To avoid a discharging trough the micro-wire it is mandatory to ground oneself while connecting or disconnecting the leads to the micro-wire.

- During the set-up of the above described wiring, the maximal input powers of each element are considered and checked in order to ensure a proper behaviour.

3.4 Micro-wire

The micro-wire[16] provides the pulsed electro-magnetic field $\vec{B}_1$ in order to invert the spins. It was first used in MRFM by Poggio et al. [142], replacing an electromagnetic coil which had typically been used so far.

CHARACTERISTICS AND FABRICATION: Nowadays the conductor consists of a 200 nm thick gold layer on a silicon chip designed by e-beam lithography and deposited by e-beam evaporation. Optical and a SEM images of the micro-wire are shown in fig. 3.5. The fabrication manual is attached in appendix A.4. In its middle a narrow, 1 μm wide and 2.5 μm long constriction increases the current density and thereby the power of B_1. With the micro-wire, field strengths at the sample position of a more than 20 mT are achieved without significantly changing the operating temperature of the system. In comparison, the previously used coil produced less than 2 mT at the sample and the dissipated heat was with 200 mW an order of magnitude bigger than with a micro-wire [103, 142].

The constriction is aligned so that the current flows in y-direction. Due to the rectangular cross-section with small height (200 nm) and relatively large width (1 μm), $\vec{B}_1$ is in immediate vicinity above the wire parallelly oriented to its surface (in x-direction) and it is constant (thin sheet approximation).

The large pads at both ends serve as contact points to connect the micro-wire chip to Cu wires by indium (In) bonding. For each of the two lines this is done by sandwiching one end of a Cu wire between two accordingly cut and flattened pieces of an In wire and squeezing them together. By pressing the In-Cu-wire-sandwich firmly but gently on the gold pads, the micro-wire is connected. This last step withstands only one attempt. The gold layer can easily be damaged by trying to attach it several times. Onto the other end of the Cu wires, a female connector is soldered, which can be plugged into the permanently installed, semi-rigid coaxial lines of the microscope. Thereby, the micro-wire chip can be (dis-)mounted easily and the flexible Cu wires guarantee a free movement of the piezoelectric positioners on which the chip is mounted.

---

[16]The micro-wire is sometimes also referred to as the strip-line [18, 143].
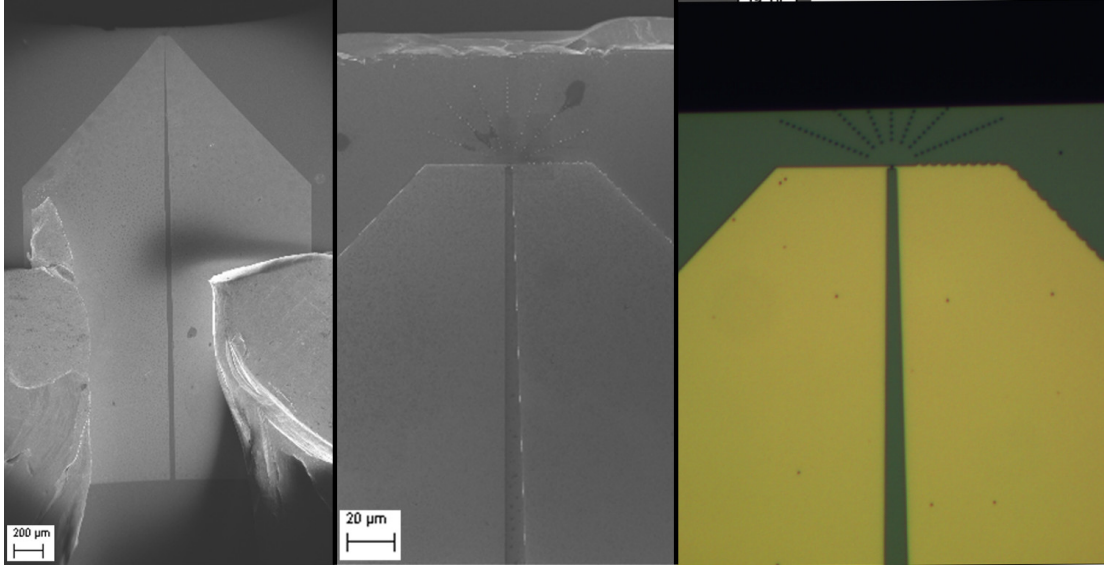
FIGURE 3.5: MICRO-WIRE
Left and middle: Scanning electron micrographs of a micro-wire. The two big chunks in the left image are the In-bonding contacts. *Right:* optical image of an other, identical micro-wire. The golden area is the 200 nm thick Au conductor. In fig. 3.6 a still bigger magnification of the same micro-wire is shown.

EXPERIMENTAL TROUBLES: Some micro-wire exemplars exhibit a non-constant dependence of B_1's power on its frequency. The higher power can drive the cantilever unintentionally via the electric field instead of the magnetic force caused by spin inversions. If this occurs within the range where f_{res} is expected, the artificial increase of σ_{ip}^2 looks similar to a real spin signal. Anomalous values of τ_m might expose the artificial nature of the signal already during the actual measurement, but τ_m can also be off due to improperly set filters.[17] A repeated measurement at different B_0 clearly uncovers the artificial driving.[18]

Such power peaks are caused by reflections of the RF current inside the wire. Calculations ruled out that their occurrence is due to the shape of the micro-wire.[19] This leaves the connections as source of the reflections, i.e. the Cu-In and In-Au interfaces of the In bonding and the plug connector. Due to the manual production of the In-bonding, different contact areas or impurities can not always be avoided completely. For a future design of RF micro-wires, connections which are impedance matched should be considered.

---

[17]See section 4.2.3.
[18]Due to $f_{\text{res}} = \gamma/(2\pi)(B_0 + B_{\text{tip}_z})$.
[19]The calculations have been made by Nicola Rossi, PhD student at the Poggiolab, Universität Basel.

OTHER MICRO-WIRE DESIGNS: Similar wires, but with wider constrictions are made
for attempted measurements in room-temperature-MRFM [144] and vortex-MRFM
(chapter 6). The larger size of the magnetic tip (next section), respectively the permalloy
disc evoking the vortex (chapter 6), require micro-wires with a width of ~ 3 μm. For
the same B_1, this in turn increases the required current and thus the heating.

3.5 Nano-Magnet

The gradient $\vec{G}$, respectively G_{zx} needed to probe the magnetic moment $\vec{\mu}$ is provided by
a *nanoscale-sized dysprosium magnet*. It is placed on top of the centre of the micro-wire
and thereby brings the high pulse field and the high gradient together. The nano-magnet
has the shape of a truncated cone with a height of ~ 225 nm and a base/top diameter of
~ 380 nm, respectively ~ 270 nm as shown in fig. 3.6. It provides gradients $G_{zx} > 1.5 \cdot$
10^6 T/m within a distance of $\lesssim 100$ nm.

The concept of using a nano-magnet in MRFM was since its introduction [142]
steadily improved, using different materials [145] (from CoFe to Dy) and geometries
[101]. It currently yields the highest $\vec{G}$ used in nano-NMR experiments and is mod-
erately difficult to fabricate compared to other methods. Other previous and ongoing
developments are discussed in chapters 1 and 7. Apart from the need of highest $\vec{G}$,
they tend to reducing the downsides of this very nano-magnet concept, as the no-flat
surface [57], that it is not switchable [56, 74], or they follow the mirrored approach of
magnet-on-tip configuration [60, 61, 146].

MATERIAL PROPERTIES: Dysprosium ($_{66}$Dy) is chosen due to its very high magnetic
moment. Paramagnetic at room temperature, it becomes ferromagnetic below 85 K. The
tip field B_{tip_z} is at typical measurement separation of ~ 50 to 100 nm in the order of $\sim$
100 to 250 mT, estimated from measured resonance frequencies $f_{\mathrm{res}} = \gamma(B_{\mathrm{tip}_z} + B_0)$.

The gradient in z-direction ($\partial B_z / \partial z$) can be determined by measuring f_{res} for
different separations between sample and nano-magnet. Though, in order to obtain
$\partial B_z / \partial x \equiv G_{zx}$, simulations of the magnetic field distribution have to be made [101,
145].

Since dysprosium is very reactive, Mamin et al. covered it in its first implementation
with a capping layer of Ti. Even though a slow, further degradation over the course of
weeks is still happening [145]. Own[20] investigations showed that after the exposure
to air and the immediate forming of the natural oxide layer, the further degradation is
as slow as with the Ti capping. In addition, the capping layer only covers the top of
the nano-magnet, leaving the sides unprotected; and it enhances the minimal distance

---

[20]Made by Fei Xue (Poggiolab, Universität Basel) in collaboration with Hans-Josef Hug (Universität
Basel).
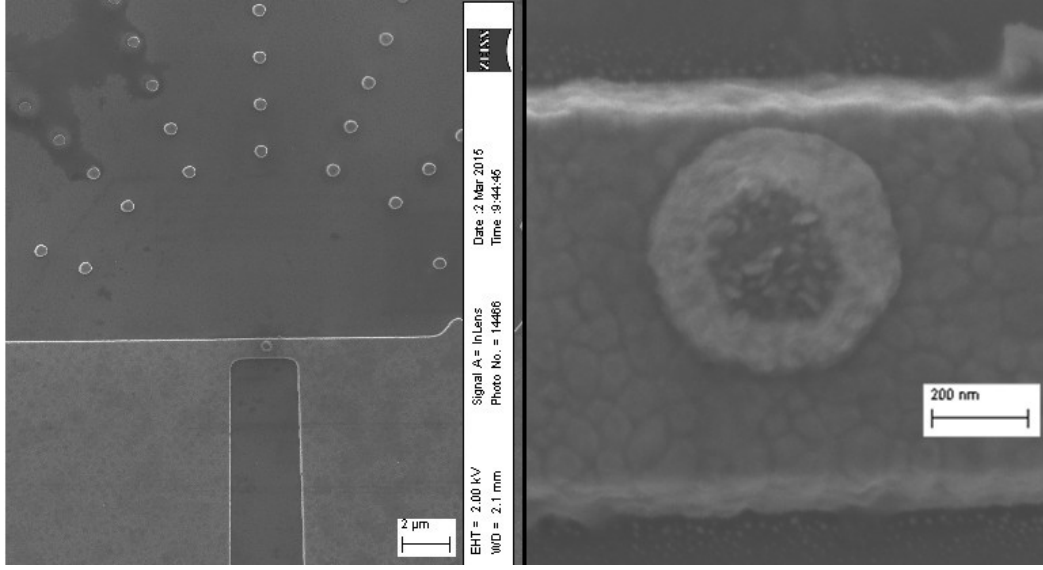
FIGURE 3.6: NANO-MAGNET

Scanning electron micrographs of a nano-magnet sitting in the middle of a micro-wire. The nano-magnet's dimensions are bottom diameter: 539 nm, top diameter: 282 nm, height: $\sim$ 300 nm. The circularly arranged dots in the upper half of the left image are guides to find the nano-magnet in the dark (see section 4.2.6).

between Dy and sample, which reduces the attainable G_{zx}. Therefore we omitted the capping of our nano-magnets.

FABRICATION: The nano-magnet is fabricated by means of e-beam evaporation only shortly before the experiment. Therefore, a stencil with accordingly sized holes is patterned with e-beam lithography on top of the micro-wire. The Dy together with a Ti sticking layer is evaporated through the stencil and the surplus material is removed by a lift-off process [142, 145].

Since highest purity is essential, an especially long pre-evaporation phase before opening the shutters was granted in order to avoid the evaporation of Dy-oxide.

3.6 Static Magnetic Field

The static magnetic field B_0 is generated by a superconducting electromagnet. It is integrated in the lower part of the cryogenic apparatus described in more detail in section 3.8 and its field is fixed orientated. The magnet exhibits in its centre a bore into which the microscope, encased by the UHV chamber, is inserted. A power supply (Cryomagnetics, Model 4G), capable to apply 5 V provides the 100 A yielding a maximum B_0 of $\pm$ 6 T.

3.7 Motion Detection

The motion of the cantilever is measured with a low power fibre-interferometer. Its advantage is the sub-angstrom displacement sensitivity and low down to not measurable heating. The interferometer is based on the work of Drake et al. in 1984 [147]. Since then, it was further improved by several researchers [58, 76, 148] and used in a series of highly sensitive measurements ranging from motion detection to scanning force microscopy, magnetometry and especially MRFM [16, 27, 30, 75, 99, 101–108, 110, 149–152]. For the presently used system the interferometer is already described in several theses [61, 117].

The section is structured into: 3.7.1 the interferometer from the laser to the photodiode and the signal monitoring, 3.7.2 the physical arrangement of the microscope's core, 3.7.3 the amplification by a lock-in amplifier and 3.7.4 the settings for the real-time observations of the signal.

3.7.1 Interferometer

PRINCIPLE: The interferometer is built up by a 1550 nm, single mode laser whose wavelength can be adjusted by an applied voltage. Its coherent light is fed into a 2x2 coupler dividing the light into a 99% arm used for reference and 1% arm for the displacement detection. Via a single mode glass-fibre and focussed by an aspheric lens, the light is aimed at the cantilever paddle. At the interface between fibre and vacuum, which forms a semi-transparent mirror, the light is split into two beams: (1) a reflected and (2) a transmitted beam. The later goes further towards the cantilever, is reflected by it and couples partially back into the fibre[21] where it interferes with the before reflected beam. Superimposed, the light travels back to the 2x2 coupler, from where 99% is fed into a photodiode measuring its power.

The two superimposing beams differ only in the phase, which the transmitted beam picks up on the way before it re-enters the fibre. When the cantilever moves, this distance and thus the phase of the transmitted beam changes. Trough the interference the varying phase modulates the total power of the superimposed beam, yielding a sinusoidal position dependent signal.

RF-MODULATION: Unmodified, the laser light's long coherence time causes disturbing reflections from other fibre interfaces. The minimally needed coherence length for the interferometry is given by the distance the transmitted beam travels before it re-enters the fibre. To extinct the disturbing reflections, the laser's phase is modulated with a arbitrary RF signal (770-1700 MHz) which reduces the coherence.

---

[21]The cavity formed between the end of the fibre and the cantilever has a very low finesse ($\mathcal{F} = 0.04$), due to the low mirrors' reflectance ($R = 30\%$).

$$\mathcal{F} = \pi \cdot \left(2 \arcsin \left(\sqrt{\frac{(1-R)^2}{4R}} \right) \right)^{-1}.$$

OPTIMAL WORKING-POINT, LINEARISED RESPONSE & TRANSDUCTION COEFFI-
CIENT α_t: Linear response as well as optimal sensitivity are achieved by dynamically
setting the wavelength, such as in the cantilever's equilibrium position the detected
signal power P_d is in the middle between maximum P_{max} and minimum P_{min} at P_{avg}.

Neglecting multiple reflections inside the cavity ($\mathcal{F} \ll 1$), P_d can be modelled as
the two component interference between reflections from the fibre end (R_1) and the
cantilever (R_2) based on the incident electric field E_i and the phase shifts acquired by
the light reflected from the fibre end (ϕ_1) and from the cantilever (ϕ_2) [117, 148]:

$$P_d = \left| E_i \sqrt{R_1} e^{i\phi_1} + E_i \sqrt{1 - R_1} \sqrt{R_2} \sqrt{1 - R_1} e^{i\phi_2} \right|^2 \quad . \tag{3.59}$$

A detailed, well written analysis and description of the very present setup is given by
Montinaro in section 2.1 of his thesis. It yields the detected power P_d depending on the
average power P_{avg}, the visibility $\bar{V}$, the cavity length l_{cav_0} and λ [117]:

$$P_d = P_{\text{avg}} \left(1 + \bar{V} \cos \frac{4\pi l_{\text{cav}}}{\lambda} \right) \quad , \tag{3.60}$$

with

$$P_{\text{avg}} = \frac{P_{\text{max}} + P_{\text{min}}}{2} = E_i^2 (R_1 + R_2) \qquad \text{and} \tag{3.61}$$

$$\bar{V} := \frac{P_{\text{max}} - P_{\text{min}}}{P_{\text{max}} + P_{\text{min}}} = \frac{2\sqrt{R_1 R_2}}{R_1 + R_2} \quad . \tag{3.62}$$

The length of the cavity is in fact varying with the oscillation $x(t)$ of the cantilever:
$l_{\text{cav}} = l_{\text{cav}_0} + x(t)$. Considering small oscillations $|x(t)| \ll \lambda$ and setting λ so that for
$x(t) = 0 \Rightarrow P_d = P_{\text{avg}}$, the linearised expression for the measured power based on the
cantilever displacement $x(t)$ is obtained [117][22]:

$$P_d = P_{\text{avg}} \left(1 + \bar{V} \frac{4\pi}{\lambda} \frac{1}{c} x(t) \right) \quad , \tag{3.63}$$

whereas c is the c-factor c (section 3.1.3) correcting the difference between the can-
tilever's measured displacement at the paddle $x(t)/c$ to the displacement at the tip $x(t)$
where F_x acts onto.

The photodiode converts the measured light into a photocurrent and finally into a volt-
age[23] V_d proportional to P_d. Differentiating eq. (3.63) in x, the linearised interferometer

---

[22]Montinaro does the derivation by adjusting l_{cav_0} which formally leads to the same result of eq. (3.63).
    In practise however λ is adjusted and l_{cav_0} is fixed.
[23]The individual gains of the photodiode are: $G_{\text{signal}} = 5.1 \cdot 10^6$ V/A, $G_{\text{monitor}} = 1 \cdot 10^5$ V/A.

gain is obtained [117]:

$$\left| \frac{\mathrm{d}V_d}{\mathrm{d}x} \right| = \frac{4\pi}{\lambda c} V_{\mathrm{avg}} \bar{V} = \frac{2\pi}{\lambda c} \left(V_{\mathrm{max}} - V_{\mathrm{min}} \right) \quad , \tag{3.64}$$

where $V_{\mathrm{max}}, V_{\mathrm{min}}, V_{\mathrm{avg}}$ are the maximal, minimal and average detected voltages respectively.

Through the above expression also the transduction coefficient α_t is determined for the present detection setup as:

$$\alpha_t = \pm \left| \frac{\mathrm{d}V_d}{\mathrm{d}x} \right| = \pm \frac{2\pi}{\lambda c} \left(V_{\mathrm{max}} - V_{\mathrm{min}} \right) \quad , \tag{3.65}$$

where the sign depends upon which side ((+)/(-)) of V_d's oscillations the laser is locked onto (see paragraph below). V_{max} and V_{min} and the (+)/(-) are without additional effort determined as described in the following paragraph. It shall be emphasised that eq. (3.65) is only valid for this displacement detection method at the described optimal working point. In general it can be determined by fitting the spectral density (section 3.1.7).

The sensitivity of the interferometer as a displacement sensor is ultimately limited by the shot noise of the photodetector. In the present setup the root-mean-squared equivalent noise displacement corresponding to $\mathrm{SNR}_{\mathrm{photodetector}} = 1$ with $P_{\mathrm{avg}} = 20$ nW is in the order of 10^{-12} m / $\sqrt{\mathrm{Hz}}$ [117, 148].

DYNAMICAL STABILISATION: The equilibrium position around which the cantilever oscillates is not stable. It is influenced by thermal drift and electric fields including non-contact friction, which are distorting the cantilever on a timescale much longer than $1/f_{\mathrm{L}_0}$. In order to keep the interferometer in the ideal measurement regime around V_{avg} the laser's wavelength λ is adjusted by a PID control loop running on an FPGA-card (NI PXI-7854R). The loop drives the laser's temperature, which is roughly proportional to λ. Therefore V_{max} and V_{min} are measured by manually tuning λ until a maxima and a minima are reached. The PID controller's target value is set to V_{avg} and the PID gain settings are tuned to achieve a fast[24] tracking without over-regulation.

For $V_{\mathrm{avg}}(\lambda)$ exist two states: one on the rising sides (+) of the oscillations of $V_d(\lambda)$ and one on the falling sides (-). Although in principle they should be equal, we observe differences in the measurement noise and measured Q-factor depending to which side λ is tuned. The differences get smaller with lower laser power and become tolerable for $P_i = E_i^2 \leq$ 15-20 nW.[25] One reason for the differences might be photon-phonon absorption / emission inducing heating, respectively cooling of the cantilever. Another origin might multiple cavities causing this effect: one between the end of the fibre and the front face of the cantilever, and a second between the end of the fibre and the back

---

[24]Still much slower then the kHz oscillations of the cantilever.

[25] $\frac{|Q_+ - Q_-|}{(Q_+ + Q_-)/2} \lesssim 3\%$

face of the cantilever.

This control loop is set up before all measurements and runs permanently. Though especially during the initial measurement preparations it gets off and has to be reset once a while. Distorting the cantilever reduces $\bar{V}$, even down to 0 in the extreme case. Short touches of cantilever and chip surfaces can easily be regulated by the loop. However, for long and extreme distortions the loop starts to diverge or stabilises with a high off-set, causing unwanted, strong heating or cooling of the laser trying to adjust λ.

EXPERIMENTAL IMPLEMENTATION: A schematic overview of the connections is given in fig. 3.4. The GaInAs-p DFB laser diode (JDSU CQF 953 401-19340), with manually made encasing and connections for power supply, RF modulation and temperature controller, is placed directly on top of the measurement system. The according supply devices: the power supply (ILX Lightwave LDX-3620), the arbitrary RF generator (Mini-Circuits ZX95-1700W-S+), RF amplifier (Mini-Circuits ZFL-1000VH), attenuators (Mini-Circuits VAT-3+ and BLK-89-S+) and the temperature controller (Thorlabs TED200C) are placed away from the system and connected via hanging cables to avoid the breaking of the vibration isolation. The latter two are controlled by an analogue output card (NI PXI-6733).

For the glass fibre connections the ordinary, factory-provided plug-connectors of the laser-diode and the 2x2 coupler (Photop, single mode, single window, wideband (1550 $\pm$ 40 nm)) are used.

The laser is operated in a maximally quiet and stable regime, where the power is much higher than needed. To reduce it, the connection from the laser-diode to the 2x2-coupler is simply loosened until only as much light as wanted is coupled into the fibre.

The displacement as well as the reference signal are measured with a photodetector with internal low-noise amplification, custom built by the institute's electronic workshop (Dual PIN-Receiver, Physics Basel (SP 928)). Its outputs are fed by coaxial cables to the subsequent devices placed away from the vibration isolated system. The signal is split and again amplified by low-noise DC and AC amplifiers (SRS SR560) before it is put in to the lock-in amplifier (only the AC signal) and the DAQ card (NI PXI-6251) of the computer. The AC and DC signals are monitored on an oscilloscope (Tektronix DPO 3034, 2.5 GS/s) and the frequency response is visualised by a spectrum analyser (SRS SR760 FFT).

The fibre is guided trough a manually made vacuum feed-trough into the system. For repair or dis-/assembly of the microscope it can be spliced[26] several times without introducing significant noise.

REFLECTIVITY TUNING: To increase the sensitivity of the interferometer the reflectivity R_1 of the fibre end is increased by *evaporating a thin film of Si* onto it. Maximal

---

[26]https://en.wikipedia.org/wiki/Fusion_splicing

visibility is achieved for $R_1 = R_2$, whereas the reflectivity of the cantilever is given by $R_2 = 30\%$. The accordingly needed film thickness is 25 nm [61].

CAVITY SETUP: The three elements which in the end have to be precisely aligned are: the end of the fibre, the lens and the cantilever. To make life easier, fibre and lens are permanently arranged together by the *sheath*, a half-open, cylindrical tube (see fig. 3.8b).

On one end of the sheath the lens is glued onto. Into the sheath the fibre is glued, so that its end is precisely centred in the lens' focal spot. Therefore a glass ferrule is put over the stripped core of the fibre, which is glued together with the fibre into the sheath. The *ferrule* ensures translational fixation while enabling small longitudinal displacement due to thermal expansion and contraction. It also facilitates the precise alignment of the laser with the cantilever.

FINE ALIGNMENT & THERMAL CONTRACTION: Eventually, the sheath has to be aligned with the cantilever such as the paddle is in the other focal spot of the lens. Further, this has to be done in a way which is invariant against thermal contraction. The fine alignment is enabled with the *fibre-holder*, which holds the sheath and wherewith its orientation can be adjusted with sub-micrometre precision.

The *fibre-holder* is basically a semi-rigid, hollow cylinder. At its base it is fixed to the rest of the *force sensor* setup (section 3.7.2 and figs. 3.8 and 3.9a). The tip can be minimally tilted by pushing with built-in set-screws on wings arranged on the sides of the cylinder. The sheath, inserted into the fibre-holder, is fixed to the tip of it and by bending the fibre-holder's tip, the orientation of the sheath and finally the orientation of the laser beam is changed.

Before the fine alignment, the cantilever has been placed so that the laser beam impacts somewhere on the cantilever's paddle and a not yet optimised interferometrical signal is established (course alignment, see section 3.7.2). After the course alignment, the cantilever is fixed in space and only the sheath (fibre end) is moved.

The first step in the *fine alignment* is to set the x-distance (in direction of the laser beam) to the lens' focal distance with help of an optical microscope. Therefore the sheath is moved along the fibre-holder's long axis and fixed with two lateral screws to the fibre-holder's tip.

The second step is the y-z-alignment. The 4 set-screws pushing on the fibre-holder's wings are therefore alternately tightened, so that $\bar{V}$ is maximal. The effect of changing the laser beam's orientation on $\bar{V}$ is observed with an oscilloscope. The tightened screws make the fibre-holder rigid and ideally the thermal contraction affects the alignment only in x-direction, but not in y and z.

During the cool-down from room temperature to 4 K the cavity between fibre and cantilever is being contracted. The change, which the maxima and minima of the oscillations of $P(T)$ thereby undergo, displays the quality of the alignment (fig. 3.7). The contraction only in x-direction does not significantly affect $\bar{V}$. Though the alignment

in y and z has to be done carefully, i.e. the screws have to be tightened equally and not too hard. Otherwise the thermal distortion in y or z kills the signal.
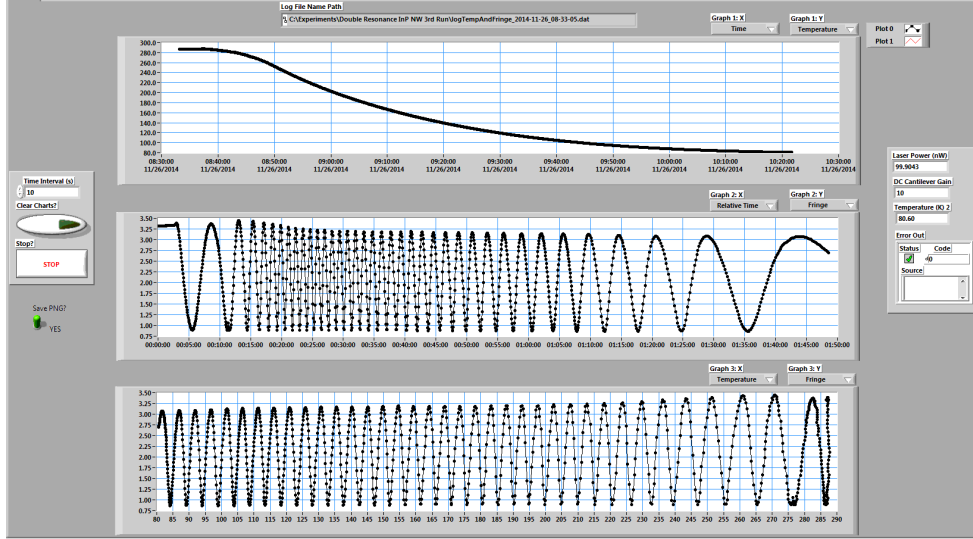
FIGURE 3.7: COOL-DOWN GRAPH – THE INTERFEROMETER'S OSCILLATIONS
Screenshot of the LabView controls showing the oscillations of the measured photodiode's voltage V_d due to the contraction of the interferometer's cavity during a cool-down. *Upper graph:* course of the temperature versus time, from room temperature to ~ 4 K; *middle graph:* V_d versus time; *lower graph:* V_d versus temperature.

For some ideal assemblies the thermal contraction does not reduce the visibility significantly. Though usually a minor reduction still has to be accepted even in a good case. A part of the reduction is characteristic for each specific sheath, respectively fibre-holder, and is reversible. To counteract it, the orientation is misaligned in y-z to an empirical value, after the maximal setting for $\bar{V}$ has been found. The major part of the reduction in visibility can thereby be avoided.

Finally, to be able to do MRFM, a minimal visibility of ~ 15 % is needed; but much higher values are possible and strongly recommended to pursue.

3.7.2 Microscope-Core Setup

OVERVIEW: The design of the microscope's core is based on the setup used in the research group of D. Rugar at IBM Research Division, Almaden Research Center. It has been re-built and further evolved in the research group of M. Poggio at Universität Basel. There exist other similar setups as for example used in the Group of C. Degen at ETHZ, which is mainly just horizontally mirrored compared to the present setup [18].

An other configuration, where the axis of the cantilever is normal to both the external magnetic field and the rf micro-wire source, was demonstrated by Xue et al. [101].

(A)

(B)
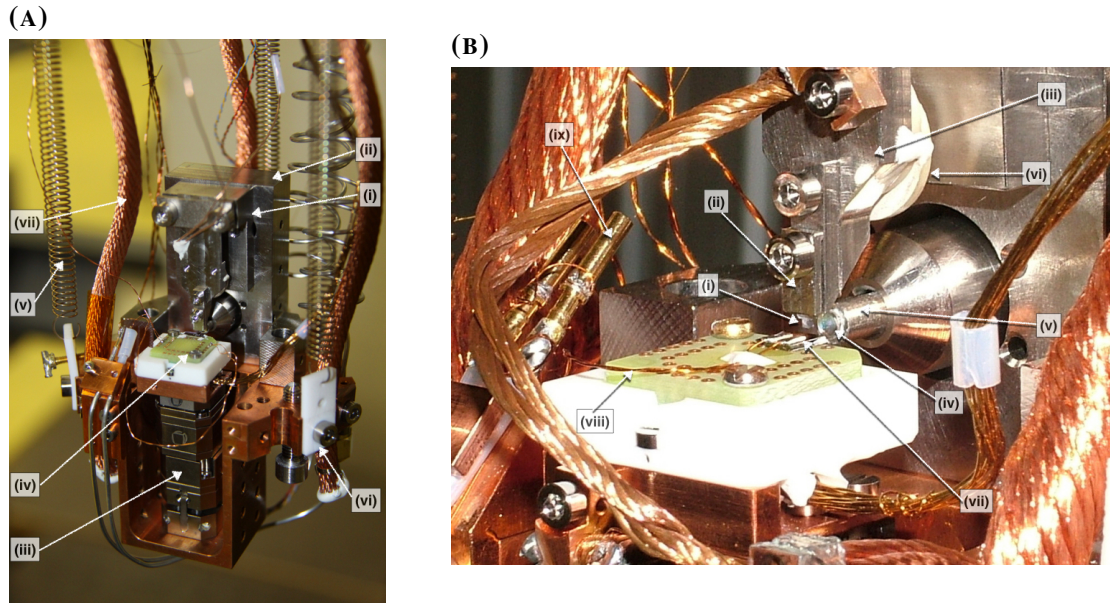
FIGURE 3.8: THE MICROSCOPE'S CORE
(A) In the upper back: the assembled force sensor with the T-block (i) mounted on the support-stage (ii); in the lower front: the piezoelectric positioner stack (iii) with an (arbitrary) chip (iv) on top. The three beryllium-copper (v) and Teflon (vi) springs isolate the microscope's core from environmental vibrations. Through the three copper leads (vii) the core is thermally connected to the cryostat. The semi-rigid coaxial RF lines are fed from the right side (spiral) underneath the positioner stack to its left side (straight), where they are fixed and connected to the wires of the micro-wire chip. **(B)** A zoom-in showing the cantilever chip (i) on the general holder (ii) and actuation lever (iii), the lens (iv) at the end of the sheath (v), the actuation piezo (vi), and an MRFM chip (micro-wire & nano-magnet) (vii) with the flexible wires (viii) to the coax-lines' connectors (ix). Photographs from the Poggiolab archive.

The core of the apparatus consists of two parts: (1) the force sensor composed of cantilever, fibre, lens and actuation piezo; and (2) the chip positioner, a stack of piezoelectric positioners on top of which a chip can be brought into vicinity of (1). For MRFM, this is the micro-wire chip with the nano-magnet. Though in general any other item close to an edge of a flat surface[27] can be measured by the force sensor [108, 109, 153]. Or it is used solely, without any other object nearby [106, 110, 151].

The core is placed on a custom designed support-stage which is suspended on springs from a corresponding ceiling-stage. The two stages are thermally connected by ~ 7 mm

---

[27]The microscope can only operate within ~ 100 μm to the edge of a chip. Further away, the laser beam gets partially blanked off.

(A)

(B)
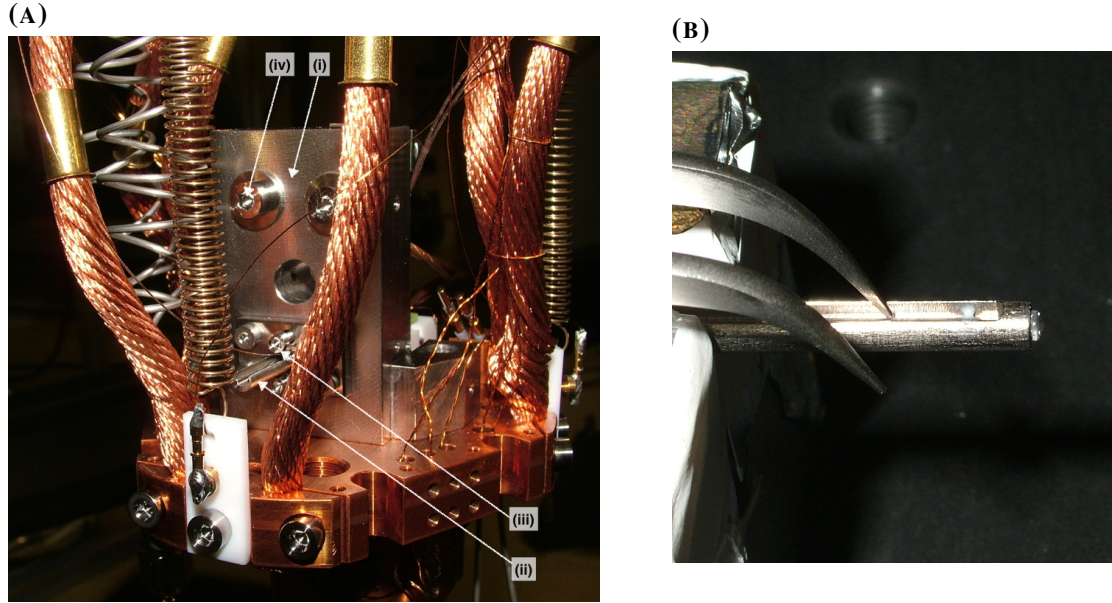
FIGURE 3.9: THE REAR SIDE OF THE MICROSCOPE'S CORE & THE SHEATH
(A) Rear side of the support stage (i) showing the sheath's back end (ii), the set-screws for the fine alignment (iii) (section 3.7.1) and the T-block's fixation screws (iv) with the mentioned big washers. The hole in the middle is for accessing the set-screw which pushes on the actuation piezo. **(B)** Front end of the sheath with the integrated lens. With the tweezers the fibre (not visible) is held in place inside the sheath while waiting for the glue to be cured. Photographs from the Poggiolab archive.

thick flexible Cu leads. Twisted cable pairs and semi-rigid coaxial lines are fixed with interconnectors to the ceiling-stage, from where the leads go directly or via an additional fixation on the supporting-stage (coaxial lines) to the individual elements.

If not specified differently, the elements of the microscope's core, including all screws, are made of titanium. It provides minimal thermal contraction and is first and foremost paramagnetic compared to steel. The second material of choice is copper (Cu, diamagnetic) exhibiting the best available thermal properties

FORCE SENSOR: The $\sim 100\,\mu$m long cantilever sits at the edge of the *cantilever chip* (see fig. 3.1, $\sim 2 \times 5 \times 1$ mm^3).[28] To simplify the handling the chip is clamped into a *general-holder* ($\sim 4 \times 10 \times 3$ mm^3), which in turn is mounted on the *actuation lever* as shown in fig. 3.8b. In order for the cantilever to eventually be precisely vertical, all elements are carefully aligned orthogonal, respectively parallel.

This assembly and the course alignment below have to be made anew for every experiment. The rest of the microscope's core is either semi-permanently or irreversibly

---

[28]All dimensions on this page refer to the frontal view and are listed as (width $\times$ height $\times$ depth).

assembled.

The *actuation lever* ($\sim 1 \times 4 \times 0.2$ cm^3) is rigidly clamped to the ⅂-*block* (fig. 3.8a, $\sim 2 \times 3 \times 1.5$ cm^3).[29] The *actuation piezo*, a stack of two piezoelectric discs, is glued to the back of the lever and faces the ⅂-block. The hot pin is thereby in the middle and the outsides go to ground. By a set-screw, pushing from the ⅂-block on the actuation piezo, the actuation lever it is bended and brought under tension. An oscillating voltage on the actuation piezo thereby drives the actuation lever and finally the cantilever.

On the other side of the cavity is the *sheath* (fig. 3.9b holding *lens* and *fibre*, which has been introduced previously. As mentioned, it is held by the *fibre-holder* enabling the fine alignment. The fibre-holder itself is screwed to a relatively big ($\sim 3 \times 5 \times 1.5$ cm^3), massive *support block*. On one side, it serves as support for the ⅂-block and has the according openings (holes) to access the ⅂-block from behind. On the other side it fixes the whole *force sensor* to the *support-stage*.

COURSE ALIGNMENT: The above assembling is made on the lab table and to some extent under a microscope. The course alignment is subsequently made on the system itself. It consist of attaching the *assembled ⅂-block* (with cantilever and sample) to the *support block*, so that the laser beam impacts somewhere on the cantilever's paddle.

For the fixation, the support block does not exhibit threaded holes, but rather much wider openings than the diameter of the attachment screws which are fed trough these openings. Thereby the assembled ⅂-block can be moved to some extend in the y-z-plane, but not in x. The fixation is finally made by clamping the two pieces together with accordingly big washers covering the openings.

For the *course alignment*, the assembled ⅂-block is pressed against the support block. Unspecific light is coupled into the fibre from behind which makes the fibre's core (the lens' focal spot) visible in the frontal view. Looking with a *microscope* on the *cantilever* and the *fibre's core*, the assembled ⅂-block is moved in the y-z-plane until the two overlap. While one person holds by hand the ⅂-block in this position an other person tightens the screws (fig. 3.9a) without distorting the alignment.

In x-direction the distance is set by means of the fine alignment, if necessary in an iterative way.

CHIP POSITIONER: The stack of the piezoelectric positioners (attocube) consists of a vertical, linear positioner (ANPz51), two horizontal linear positioners (ANPx51) and a horizontal scanner (ANSxy50) screwed on top of each other. With the linear positioners a 3 mm $\times$ 3 mm $\times$ 2.5 mm region can be covered whilst the scanner enables finer positioning than with the linear positioners (subnm precision on 15×15 μm^2).

On top of the stack, a holder (Cu) designed to receive the micro-wire chip is mounted.

---

[29]The term refers to the side view, which has the shape of an L that has been turned upside down: ⅂. In the textual visualisation the cantilever is facing down at the left side of ⅂.

Positioning with the positioner stack is straight-forward and simple. But the stack exhibits the disadvantage of noticeable oscillations. By coupling trough non-contact friction to the cantilever's oscillation they can increase the measurement noise floor.

3.7.3 Signal Amplification (Lock-In Amplifier)

The signal caused by the spin inversions oscillates with the cantilever frequency f_{L_0}. Its phase is well defined by the driving through the ARP pulses, which enables the amplification by a digital lock-in amplifier (Zurich Instruments HF2LI).

In essence, a lock-in amplifier multiplies the measured signal with a reference signal and integrates it over a time much longer than one period. Thereby signals at other frequencies than the reference, as well as signals at the reference frequency but uncorrelated or shifted in phase, are strongly attenuated. This yields two outputs, one in-phase with the reference (ip) and the other, the quadrature (qd), shifted 90 ° to the reference. The in-phase signal contains the evoked measurement (spin) signal *and* the measurement noise. Though the quadrature contains *only* the noise, which is for the present system mainly caused by the thermal cantilever oscillations.

The reference signal is given by the 4th harmonic of the AWG's trigger signal ($f_{\text{trigger}} = 1/4 f_{L_0}$), which the lock-in amplifier can generate internally based on f_{trigger}. A phase shift between reference and measured signal can be set manually or it can be estimated by the lock-in amplifier to yield a maximal difference between in-phase and quadrature. The measured signal is demodulated with six different bandwidth filters, whereby the spectral distribution of the signal ($\to \tau_m$) can be approximated (see section 4.2.3).

The six signal pairs are analysed by the lock-in amplifier and digitally sent to the computer for further conversion, monitoring and recording. In classic MRFM it is the difference in variance $\sigma_{\text{ip}}^2 - \sigma_{\text{qd}}^2$ which is finally of interest (see section 4.1.4).

3.7.4 Real-Time Observation of the Signal

The above outlined method buffers the data between lock-in amplifier and computer, causing a slight delay in the observation. By *connecting* the two *analogue outputs* of the in-phase and quadrature signal via a DAQ-card to a *FPGA-card*, the buffering is avoided and the delay becomes negligible (limited by the performance of the lock-in amplifier). The FPGA card is mounted into the same PXI chassis as the DAQ-card and the AWG, connecting the them directly via PCI buses. The reaction time, how fast the applied pulses can be changed based on the measured signal, is in this configuration only limited to the AWG's trigger period. For real-time observation techniques such as *manipulation of the spin noise's distribution* and *storing of spin fluctuations* (see section 4.3.5), the trigger is thus set to $f_{\text{trigger}} = f_{L_0}$. The fast reaction time enables to immediately change the ARP pulses (e.g. its frequency or length) based on the observed signal; immediately means here for the next, upcoming cantilever oscillation period.

This configuration was introduced by Peddibhotla [61, 103] and adapted for the measurements presented in chapter 5 and in [104].

3.8 Measurement Environment

3.8.1 ^{4}He Fridge

The majority of the performed experiments are made in ^{4}He bath cryostat (Cryomagnetics magnet model 60-500-010L). For some single runs (vortex MRFM tests), a ^{3}He flow cryostat is used too.

The ^{4}He Fridge consist of a inner vessel containing the superconducting magnet-coil with a bore whole for the UHV chamber. The latter encases the microscope's core and is located at the end of a ~ 2 m long hollow dip-stick, which is inserted into the cryostat. The inner vessel is eventually filled with liquid helium. It is surrounded by a nitrogen jacket, separated by a lower vacuum ($\lesssim 10^{-3}$ mbar), to reduce the helium consumption. Vibrations caused by the boil-off of the cryogenic liquids are efficiently absorbed by the vibration isolation.

For the cool-down, liquid nitrogen is first filled into the inner vessel too, until the system reached a temperature of $\lesssim 80$ K. The stable temperature enables the intermediate alignment of cantilever and micro-wire. In a second phase, the nitrogen is pumped out of the inner vessel and it is filled with helium. For permanent operation the helium has to be refilled every $\sim$ 5-6 days.

3.8.2 Vacuum System - The Dip-Stick

The whole dip-stick, its rod and the chamber around the microscope's core build one connected UHV-system. It is pumped with a turbo-pump (Pfeiffer HiPace 80) backed up by an oil-free diaphragm-pump (Pfeiffer MVP 015), wherewith a pressure $< 10^{-7}$ mbar is achieved. Before cooling down it is sealed off to avoid a fighting of the cold system against the turbo-pump. The cryogenic pump effect of 4 K keeps the UHV over weeks.

3.8.3 Vibration Isolation

The microscopes's vibration isolation basically consists of two parts: three *mechanical springs* by which the microscope's core is suspended and a *floating table* which the whole cryostat is sunken into.

The first part itself again consists of two components: A ~ 15 cm long *Cu spring* absorbs low frequency vibrations and ~ 1.5 cm long *Teflon pieces* at the ends of the Cu spring block the higher frequencies.

The floating table decouples the whole system from environmental vibrations.

4 Classic Magnetic Resonance Force Microscopy

> *Le simple est toujours faux. Ce qui ne l'est pas est inutilisable.*

Paul Valéry, *Œuvres II*, 1942

This chapter covers in its first section the working principle of MRFM. Subsequently in section 4.2 additional necessities in order to be able to do MRFM are discussed, as e.g. damping of the cantilever's motion. Section 4.3 lists experimental procedures as e.g. measurements preparations, signal optimisation, and imaging.

4.1 Full Working Principle

This section covers how MRFM works in detail. It starts with the explanation of how spins can be inverted and discusses the main subtopics necessary to eventually get a measurable, quantified signal. A prerequisite for the following sections is the basic physics of nuclear spins recapped in section 2.1.

A short form of MRFM, with an overview of the working principle is given in section 1.3.

4.1.1 Spin Inversion

OVERVIEW: Spins, aligned along a static field $\vec{B}_0$, can be adiabatically inverted from $|\uparrow\rangle$ to $|\downarrow\rangle$ by applying an electromagnetic pulse $\vec{B}_1$ perpendicular to $\vec{B}_0$ and sweeping its carrier frequency $\omega_{\mathrm{RF}}(t)$ through the resonance[1] at $\omega_{\mathrm{res}} = \omega_0$. The technique is called *adiabatic rapid passage* (ARP) and makes use of the precession of spins around a magnetic field. The principle is to alter the effective magnetic field $\vec{B}_{\mathrm{eff}} = \vec{B}_0 + \vec{B}_1(t)$ with the help of $\vec{B}_1$. Spins follow $\vec{B}_{\mathrm{eff}}$ as long as its change is slow enough. Consequently by rotating $\vec{B}_{\mathrm{eff}}$ about 180 ° they get inverted, as depicted in fig. 4.1. In the next paragraphs the process of a simple inversion is carried out. More on the theory and other forms of ARP pulse sequences are discussed in section 2.2.

---

[1] $\omega_{\mathrm{res}} = \omega_0$ is only true for this section. Later on, ω_{res} will also depend on the field of the nano-magnet $\omega_{\mathrm{res}} = \gamma B_z = \gamma(B_0 + B_{\mathrm{tip}_z})$.

In order to simplify the expression of $\vec{B}_{\mathrm{eff}}$, the different fields are in the following denoted by their angular frequency vectors corresponding to the specific spin, i.e. $\vec{\omega}_0 = \gamma\vec{B}_0$, $\vec{\omega}_1 = \gamma\vec{B}_1$ and $\vec{\omega}_{\mathrm{eff}} = \gamma\vec{B}_{\mathrm{eff}}$.

ROTATING FRAME: ARP is described the easiest by considering a rotating Cartesian coordinate system (x', y' and z'). This rotating frame - shown anew[2] in fig. 4.1 - is spinning with varying frequency around the z-axis of the laboratory frame, whereas the origins and the z and z'-axes coincide with each other.

The static field $\vec{\omega}_0$ is set in z-direction and the RF pulse field $\vec{\omega}_1$ rotates in the x-y-plane of the laboratory frame with the angular velocity $\omega_{\mathrm{RF}}(t)$. The trick is to set the angular frequency of the rotating frame to this very same $\omega_{\mathrm{RF}}(t)$. Thereby $\vec{\omega}_1$ is in the rotating frame all the time at rest. In addition to the static field and the magnitude of $\vec{\omega}_1$, also the accelerated temporal dependency of the RF-pulse contributes to the effective field. The oscillation of $\vec{\omega}_1$ can be described by $\vec{\omega}_{\mathrm{RF}}$, a vector perpendicular to the direction of the RF-pulse $\vec{\omega}_1$ with magnitude ω_{RF}. It thus points along the z-axes, parallel with $\vec{\omega}_0$. For convenience the two vectors can be merged and expressed as detuning $\vec{\Delta\omega} = \vec{\omega}_0 - \vec{\omega}_{\mathrm{RF}}$. Finally the effective field becomes then $\vec{\omega}_{\mathrm{eff}} = \vec{\omega}_0 + \vec{\omega}_1 - \vec{\omega}_{\mathrm{RF}} = \vec{\Delta\omega} + \vec{\omega}_1$.

THE RAPID FORM OF THE ADIABATIC RAPID PASSAGE: The ARP pulse starts at $t = 0$ with $\omega_{\mathrm{RF}} \ll \omega_0$. This means, $\vec{\omega}_{\mathrm{eff}}$ is pointing vertically upwards with the spin precessing around it. Now ω_{RF} is increased, which reduces $\vec{\Delta\omega}$ and rotates $\vec{\omega}_{\mathrm{eff}}$ in the x'-z'-plane as shown in fig. 4.1a. When $\omega_{\mathrm{RF}} = \omega_0 \Rightarrow \vec{\Delta\omega} = 0$ and $\vec{\omega}_{\mathrm{eff}}$ is pointing in x'-direction (fig. 4.1b). Increasing ω_{RF} further makes $\vec{\Delta\omega}$ negative and continuously rotates $\vec{\omega}_{\mathrm{eff}}$ until it points vertically downwards at $t = t_p$ (fig. 4.1c). If this passage is done adiabatically, the spin follows the moving $\vec{\omega}_{\mathrm{eff}}$, all the time precessing around it. Adiabatically means: $|\omega_{\mathrm{eff}}(t)| \gg |{}^{\mathrm{d}\alpha_p}\!/_{\mathrm{d}t}|$, i.e. *The magnitude of the effective field has to be much bigger then the speed of its rotation;* (see section 2.2.2).

The frequency range over which ω_{RF} is swept is called the modulation width of the RF-pulse $\Delta\omega_{\mathrm{mod}} = 2\Delta\omega(t = 0)$. The centre frequency of the sweep is in general named ω_{centre}, which is on resonance equal with ω_{res}.

NEIGHBOURING SPINS: In a magnetic field gradient, the neighbouring spins to the one with ω_{res} experience a slightly different field, hence their resonance occurs at a different frequency $\omega_{\mathrm{res}} + \Omega$, whereas Ω is the offset from ω_{res}. All spins within the frequency range $-\Omega_{\mathrm{max}} \geq \Omega \geq \Omega_{\mathrm{max}}$ get inverted by the same ARP pulse. The boundary Ω_{max} is set by the criteria $\Delta\omega_{\mathrm{mod}} \gg \Omega_{\mathrm{max}}$, i.e. that the modulation width $\Delta\omega_{\mathrm{mod}}$ is big enough compared to the deviation from ω_{res}. Of course also the adiabatic condition has to be fulfilled for these frequencies.

---

[2]The figure is already shown in section 2.2, fig. 2.1. It is redisplayed here in the partially recapitulatory section *Full Working Principle* to prevent the reader from being forced to scroll.

(A) $\vec{\omega}_{\mathrm{RF}} \ll \vec{\omega}_0$

(B) $\vec{\omega}_{\mathrm{RF}} = \vec{\omega}_0$

(C) $\vec{\omega}_{\mathrm{RF}} \gg \vec{\omega}_0$
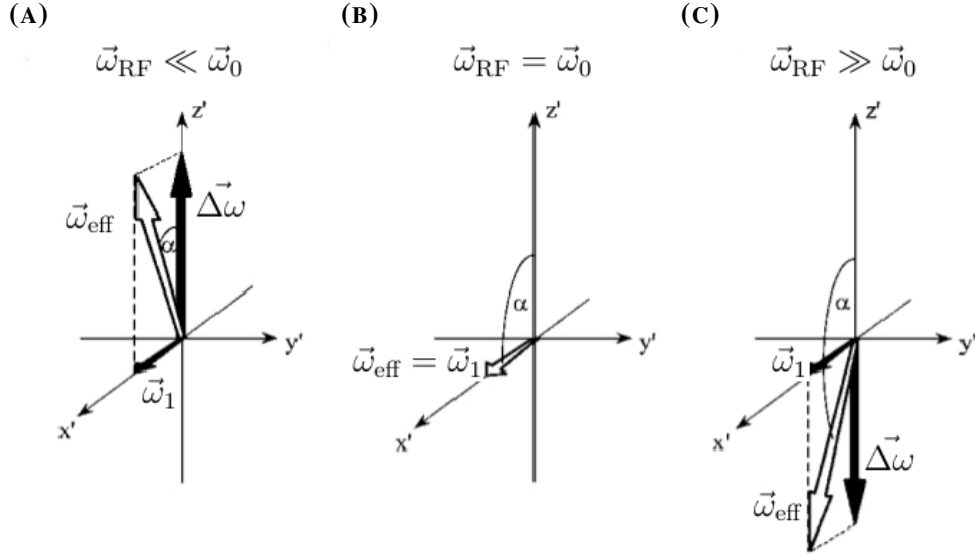
FIGURE 4.1: THE VECTOR $\vec{\omega}_{\mathbf{EFF}}$ OF THE EFFECTIVE MAGNETIC FIELD IN THE ROTATING FRAME

Its components are $\vec{\omega}_1$, the amplitude of the RF-field $\vec{B}_1$, and $\vec{\Delta\omega}$, the detuning of $\vec{B}_1$'s frequency from the resonance frequency $\omega_{\mathrm{res}} = \omega_0$. A nuclear spin $\vec{S}$ precesses around $\vec{\omega}_{\mathrm{eff}}$ and follows it as long as the adiabatic condition is fulfilled. The sequence shows the situations **(A)** far below resonance at the beginning, **(B)** at resonance and **(C)** far above resonance at the end of the sweep. Figure adapted from [96].

Although the inversion of these spins is not synchronous, the pulse rotates all of them by 180 ° in the same amount of time. This enables to concatenate the ARP pulses without inducing pulse related dephasing of the ensemble.

FREQUENCY AND AMPLITUDE MODULATION: In order to optimise the inversion efficiency for a given average power of $B_1(t)$ and pulse length t_p, the amplitude as well as the frequency of a pulse are modulated. For all measurements in this work hyperbolic secant ARP pulses are used. I.e. the amplitude is modulated by a hyperbolic secant and the frequency by a hyperbolic tangent function, as described in section 2.2.

4.1.2 Magnetic Gradient

FORCE GENERATION: As the name Magnetic Resonance *Force* Microscopy says, the transduction of the spin signal to the sensor is mediated by force. A magnetic moment $\vec{\mu}$

in a non-uniform magnetic field exerts a force according to

$$\vec{F} = \nabla \left(\vec{\mu} \cdot \vec{B} \right) \quad . \tag{4.1}$$

Due to its geometry, a cantilever is mainly sensitive in its oscillation direction ($\hat{e}_x$). Hence, arranged ideally, only the x-component of the three dimensional force vector $\vec{F}$ excites a displacement and the relevant component of the above equation is reduced to

$$F_x = \vec{\mu} \cdot \frac{\partial}{\partial x} \vec{B} \quad , \tag{4.2}$$

as shown in appendix A.3. Because in average the transversal components of $\vec{\mu}$ cancel out, only μ_z remains contributing.[3] Replacing μ_z by the ensemble's magnetisation in z-direction M_z, the force in x-direction becomes

$$F_x = M_z \frac{\partial B_z}{\partial x} = M_z G_{zx} \quad . \tag{4.3}$$

The gradient $G_{zx} \equiv \partial B_z / \partial x$ is produced by a nano-magnet made of dysprosium ($_{66}$Dy) as described in section 3.5. B_z is thereby the sum of the external, homogeneous, in z-direction applied field B_0 and the z-component of the field produced by the nano-magnet B_{tip_z}. At a typical measurement distance of 50-100 nm between sample and magnet G_{zx} is in the order of $5 \cdot 10^5$ T/m.

It shall be especially noted, that the strength of G_{zx} holds a big importance for the sensitivity of MRFM. Together with the parameters defining the force noise density S_F (section 3.1.7) it is one of the few toe-holds for further improvement.

RESONANCE SLICE: For a given resonance frequency ω_{res} all spins located at a positions within $B_z = (\omega_{\text{res}} \pm \Omega_{\text{max}})/\gamma$ get inverted by the ARP pulse. The spatial region where this condition is fulfilled is called the resonance slice. The region where the sample intersects with it is called the resonance volume. For a nano-magnet with the shape of a truncated cone the resonance slice has the form of a hemispherical shell as visualised in fig. 1.1. It can be calculated by modelling the field produced by the magnetic tip $\vec{B}_{\text{tip}}$ as shown by Degen et al. [99] and can be iteratively improved during image reconstruction (see section 4.3.4). The strongest gradients G_{zx} are found in front and behind of the tip (on the x-axis setting the origin on the centre of it).

4.1.3 Continuous Spin Inversion

Repeating the ARP pulses inverts the spins consecutively from $|\uparrow\rangle$ to $|\downarrow\rangle$ to $|\uparrow\rangle$ and so on. Thereby the magnetic moments, respectively namely their z-components μ_z, are

---

[3] Also the longitudinal component μ_z is in average zero, but its motion is correlated with the cantilevers oscillation and can therefore drive it (see section 4.1.3).

oscillating with the frequency $\omega_{2\mathrm{p}} = (2\pi)/(2t_p)$, where t_p is the length of the ARP pulse. Consequently the force from eq. (4.3) becomes time-dependant $F_x(t)$ and is oscillating with $\omega_{2\mathrm{p}}$, although not sinusoidally.

The oscillation of the cantilever is described as derived in section 3.1 by the Langevin equation (eq. (3.28)). The magnetic force acting on it is added to the equation, as done before with the thermal force, resulting in

$$m\ddot{x}(t) + \Gamma_0\dot{x}(t) + m\omega_{\mathrm{L}_0}^2 x(t) = F_{th}(t) + F_x(t) \quad . \tag{4.4}$$

By synchronising the inversion with the cantilever's oscillation the cantilever gets driven resonantly. In order to match the resonance, the spins have to be inverted twice per cantilever oscillation, which is achieved by setting the length of the ARP pulses to $t_p = \pi/\omega_{\mathrm{L}_0}$, i.e. $\omega_{2\mathrm{p}} = \omega_{\mathrm{L}_0}$, where ω_{L_0} is the fundamental mode of the cantilever. The signal originating in the spins is thereby enhanced through the resonant behaviour of the cantilever whose displacement Δx can be measured as described in section 3.7. The differentiation between the spin signal transduced by F_x and the uncorrelated thermal noise force F_{th} is done by a lock-in amplifier (see section 3.7.3) yielding to a signal purely depending on the amount of spins.

4.1.4 Noise as Measurement Observable

OVERVIEW: Typically, in physical measurements the actual or mean value of a quantity is of interest and the deviation is considered as the error of the measurement. In MRFM, it is indeed the statistical deviation from the mean value which serves as measurement observable.

The mean magnetisation of a paramagnetic substance originates in the polarisation of the spins into parallel and anti-parallel alignment to an external magnetic field. It is called the thermal or Boltzmann polarisation. Due to the continuous spin inversion the spins do not have the time to align with $\vec{B}_0$ and any previous polarisation will also be destroyed over time. Therefore, the mean magnetisation M_z of the measured ensemble is zero.

However, the ensemble of spins exhibits a statistical polarisation due to incomplete cancellation of random spin flips. On average, the statistical polarisation is also zero, independent of a possible inversion. But it causes the standard deviation σ_{M_z} to be non-zero, even if $M_z = 0$. This spin noise is independent of B_0 and can also be measured without an external magnetic field [3, 21, 154].

How σ_{M_z} is measured in MRFM is carried out in the following. A description of the characteristics of statistical polarisation, especially compared to the thermal polarisation is given in section 5.2.

MEASUREMENT: With a lock-in amplifier the displacement of the cantilever is measured on two different channels, one of them in-phase (ip) with the driving by $\vec{B}_1$, and

the other 90 ° shifted, out-of-phase. The latter is typically called the quadrature channel (qd). The mean value of both channels is in the ideal case zero. The variance of the in-phase channel σ_{ip}^2 contains the spins noise and the thermal noise. In contrast, that of the quadrature channel σ_{qd}^2 contains only the uncorrelated thermal noise. The pure spin signal's variance $\sigma_{\mathrm{spin\text{-}signal}}^2$ is hence given by

$$\sigma_{\mathrm{spin\text{-}signal}}^2 = \sigma_{\mathrm{ip}}^2 - \sigma_{\mathrm{qd}}^2 \quad . \tag{4.5}$$

Every measurement is flawed with an error, which is here given by the error noise $\epsilon_{\mathrm{signal}}$

$$\epsilon_{\mathrm{signal}} = \sqrt{\left(\sigma_{\mathrm{ip}}^2\right)^2 + \left(\sigma_{\mathrm{qd}}^2\right)^2} \sqrt{\frac{2 \cdot 2.2 \cdot T_{\mathrm{lock\text{-}in}}}{t_{\mathrm{acqui}}}} \quad , \tag{4.6}$$

whereas $T_{\mathrm{lock\text{-}in}}$ is the time constant of the lock-in amplifier $(1/f_{\mathrm{3dB}})$, t_{acqui} the acquisition time and the factor 2.2 the correction of the bandpass Butterworth filter's equivalent noise bandwidth.

Dividing these two quantities yields the experimental signal to noise ratio of the measurement

$$SNR_{\mathrm{exp}} = \frac{\sigma_{\mathrm{spin\text{-}signal}}^2}{\epsilon_{\mathrm{signal}}} \quad . \tag{4.7}$$

The theoretical SNR of the force transducer is described in section 3.1.7 and eq. (3.58).

4.1.5 Quantification of the Magnetic Moment and the Number of Spins

The determination of σ_{M_z} and the ensemble's number of spins N_{spins} in a straight forward way based on $\sigma_{\mathrm{spin\text{-}signal}}$ is in principal possible, although very imprecise. The expression for σ_{M_z} is found by combining eqs. (3.47), (4.3) and (4.5) and replacing the quantities with their standard deviations (σ_{M_z} for M_z, $\sigma_{\mathrm{spin\text{-}signal}}$ for x):

$$\sigma_{M_z} = \frac{k}{\alpha_t Q G_{zx}} \sqrt{\sigma_{\mathrm{ip}}^2 - \sigma_{\mathrm{qd}}^2} \quad , \tag{4.8}$$

whereas α_t is the transduction coefficient converting the displacement into a voltage. The number of measured spins is predicted by statistical mechanics and can be calculated according to

$$N_{\mathrm{spins}} = \sigma_{M_z}^2 \frac{3}{I(I+1)(\hbar\gamma)^2} \quad , \tag{4.9}$$

where I denotes the spin quantum number.

The issue is that the value of the gradient G_{zx} is very difficult to determine precisely. Exact knowledge of the nano-magnets magnetisation and its geometry as well as the

size of the resonance volume (the intersection of the sample with the resonance slice) is therefore necessary. Requirements, that can in practise only be estimated coarsely. Hence, the error on σ_{M_z} respectively on N_{spins} is large. A much more accurate method of determination these quantities was developed and demonstrated during this work and presented in chapter 5.

4.2 Additional Necessities

The continuous, adiabatic inversion of spins in a gradual magnetic field together with the separation of correlated from uncorrelated noise covers the full working principle of MRFM. In practise, however, a few more, not less important things, have to be considered in order to get it working. Explained in the next subsections, these are in particular: (1) the broadening of the cantilver's spectral density peak (damping), (2) the phase continuity of the ARP pulses, (3) the determination of the spin ensembles correlation time as an immediate indication of a real signal, (4) the enhancement of the SNR by averaging, (5) the counteraction against cantilever frequency changes and - last in this listing but first in practise - (6) the ability to navigate the sample with respect to the nano-magnet.

4.2.1 Damping

MOTIVATION: In MRFM cantilevers with highest possible quality factors are used in order to obtain a maximal enhancement through the resonant amplification. Such high Q levers exhibit a very narrow Lorentzian peak in the spectral density $S_x(f)$ as shown in fig. 4.2a.

For a force driving the cantilever, this acts like a bandpass filter. It is highly sensitive at the resonance frequency ω_{L_0}, whilst inert to forces at other frequencies, proportional to the line shape of $S_x(f)$. Letting Q unaltered would restrict the minimal measurement bandwidth $\Delta f_{\text{BW}_{\text{min}}}$ dramatically, since it must fulfil $\Delta f_{\text{BW}_{\text{min}}} < f_{L_0}/Q$ [104]. For the used levers this would be $\Delta f_{\text{BW}_{\text{min}}} \lesssim 0.1$ Hz.

A further consequence of the high Q is the slow response time to the applied force. This increases the necessary recording time for a single measurement and thus even more so the total time for the averaged measurement.

To avoid these effects the cantilever is damped by a feedback circuit from initially $Q \approx 3 \cdot 10^4$ to $Q_{\text{damped}} \approx 400$, thereby the line shape of $S_x(f)$ gets broadened and the amplitude of the oscillation is reduced.

The broader and less steep Lorentzian peak increases the maximal allowed $\Delta f_{\text{BW}_{\text{min}}}$. It additionally allows the resonance frequency of the cantilever ω_{L_0} to be slightly off the applied RF-pulse sequence frequency ω_{2p}, without losing much amplification and introducing a too big error to its estimation. This is in practise important, since in

(A)   **(B)**
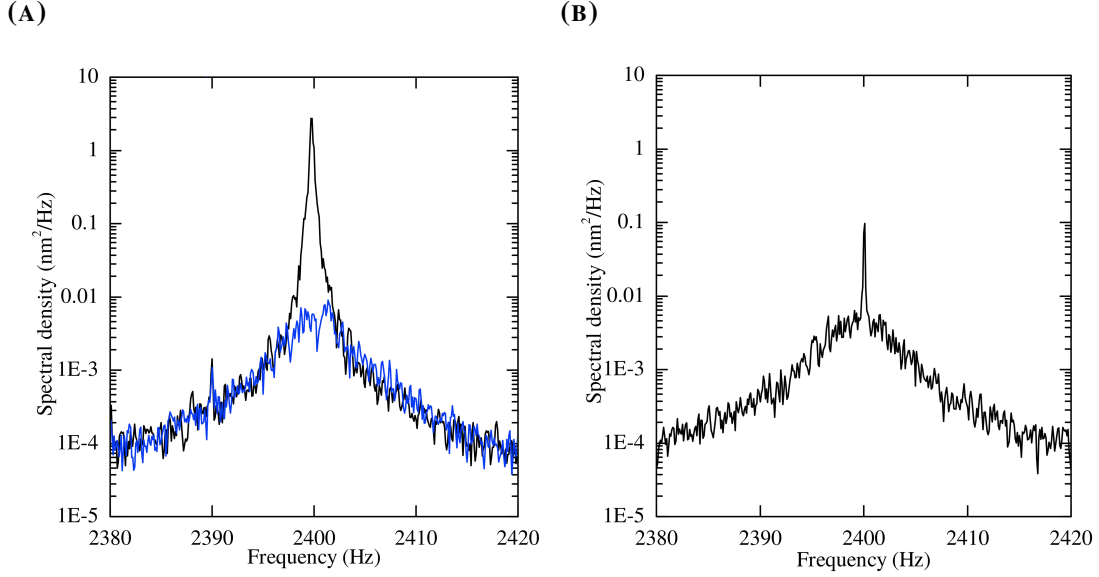
FIGURE 4.2: SPECTRAL DENSITIES OF THE CANTILEVERS OSCILLATION
(A) The undamped case (upper curve in black) compared to the damped case (lower curve in blue). **(B)** The superposition of the damped thermal oscillation with the (equally damped) spin signal centred on top. Figure adapted from [61].

the measurement position in closest vicinity to the micro-wire ω_{L_0} is never absolutely stable.[4] A maximal deviation of $|\omega_{L_0} - \omega_{2p}| \lesssim 0.7$ Hz has turned out to be acceptable.

UNCHANGED SIGNAL TO NOISE RATIO: Feedback damping reduces the Q which is responsible for the big enhancement of the signal. Nevertheless the SNR and the levers force sensitivity are not sacrificed, since the damping reduces the motion of the cantilever independent of its origin. Thus, the ratio of signal to noise stays the same compared to the unmodified motion and it is still given as derived in section 3.1.7 by $\text{SNR} = N(\mu_z G_{zx})^2/(S_F \Delta f_{\text{BW}})$.

FEEDBACK CIRCUIT: The electronic feedback damping can be achieved by measuring the cantilevers position $x(t)$, differentiating it and send it amplified, as a *negative feedback* to a piezoelectric disc actuating the cantilever. Thereby the oscillation can be damped down to a mode temperature limited by the properties of the cantilever and the measurement noise, as described by Poggio et al. [105].

---

[4]ω_{L_0} can fluctuate due to vibration or drift of the micro-wire chip mediated by the electric field to the cantilever.

The motion can also be damped by applying a by *optimal control* theory [61, 155] calculated rather than measured function. Therefore the baseline noise density of the cantilever's spectrum, the thermal force noise, the levers spring constant, f_{L_0} and Q are measured. Together with the desired target quality factor and parameters determining gain and actuation, the transfer function can be calculated. Driving the piezoelectric disc with the transfer function damps the cantilever's oscillation. Properly calculated and applied, the optimal control transfer function performs better for strong damping then negative feedback, since it considers also the thermal noise [61]. In practise however, this method was not yielding the desired target Q "out of the box". It was nevertheless used as a good starting point. Subsequently, the desired damping was eventually achieved by heuristically tuning the optimal control parameters and surveying the effect on the cantilevers spectrum. Additionally to the mentioned parameters, the phase shift compensating delaying effects of the feedback circuit has to be tuned properly.

DETERMINATION OF THE QUALITY FACTOR: The knowledge of the Q-factor is decisive for the quantity of the measured signal since it determines its amplification (see sections 3.1.6 and 4.1.5). The intrinsic Q-factor as well as the damped one are determined by ring-down measurements. This method appeared to be more accurate than measuring the spectral density and calculating the area under the resonance peak, especially in regard to the required time.

For a ring-down measurement, the cantilever is excited by the piezoelectric disc to oscillate with a higher amplitude and the oscillations's decay, which is proportional to $\exp\{1/(Qt)\}$, is measured. For the damped case the two signals - the feedback damping and the excitation for the ring-down - are mixed in analogous manner by a two channel input amplifier.

The Q can significantly change for different positions, if the cantilever's tip is in close vicinity to the nano-magnet, Especially for imaging it should therefore be anew measured for each position. An automation of the process is possible and done in the experiments of Moores et al. [18, 156], but was not implemented in our measurements. The difficulty lies in the setting of the excitation amplitude while the cantilever is damped. If it is too little, the ring-down happens too fast and can not be measured. If it is too high, the cantilever does not oscillate harmonically at f_{L_0} any more. Hence, the right driving amplitude has to be found by increasing it step by step. This extends the amount of time for measuring a single point twofold: firstly because the Q measurement has to be done at all and secondly because the right amplitude for the measurement has to be found successively.

4.2.2 Pulse Phase Continuity:

While concatenating single ARP pulses it has to be ensured that the phase of $\omega_{RF}(t)$ is continuous between two consecutive pulses. Otherwise $\vec{B}_{eff}$ is discontinuous, the

precessing spins are not able to follow it at the intersections and the signal decays over time.

The pulse length t_p is therefore adjusted via correcting the centre frequency f_{centre} of f_{RF} to be an integer multiple of the corrected resonance frequency $f_{\text{L0corrected}}$ of the cantilever. Already f_{L0} is beforehand adjusted to match the sampling rate of the arbitrary waveform generator for technical reasons. The explicit corrections are listed in appendix A.1.

4.2.3 Determination of the Ensemble's Correlation Time τ_m:

The random spin noise causing statistical polarisation exhibits a correlation characterised by the spin ensemble's correlation time τ_m, which can be hundreds of milliseconds to several seconds long. It is closely related to the intrinsic rotating-frame spin lifetime $T_{1\rho}$ and additionally depends on a number of extrinsic parameters, such as the amplitude and modulation of $\vec{B}_1$ [5, 97].

On one hand, τ_m can be determined by calculating the autocorrelation function of $\sigma_{\text{spin-signal}}$'s time trace and fitting its exponential decay as done by Degen et al. [97]. On the other hand, τ_m is found with less effort by measuring $\sigma_{\text{spin-signal}}$ with different filters (bandwidths Δf_{BW}). The spectral density of the spin signal has a Lorentzian line shape which is indeed characterised by τ_m too. With help of e.g. 6 well chosen filters of the lock-in amplifier, the line shape of the spin signal's spectral density can be fitted and τ_m can be calculated without storing the whole time trace.

4.2.4 Averaging

CUTBACK OF UNCORRELATED MEASUREMENT NOISE: The signal $\sigma_{\text{spin-signal}}$ is typically averaged for a time t_{aqui} of 60 to 180 seconds, which reduces the error ϵ_{signal} by a factor $\sqrt{1/t_{\text{aqui}}}$ (see eq. (4.6)). In principle even smaller signals and fewer number of spins could be measured with longer averaging times. For MRFM imaging or other applications though, the total required time just gets too long. Especially since the increase of the SNR is not linear, but it gets smaller over time by the square-root like dependence. Neither are shorter t_{aqui} recommended, e.g for quick scans in order to find ω_{res} at the beginning of a measurement (see section 4.3.2), since too few independent[5] samples would be taken.

REDUCTION OF THE SPIN SIGNAL'S ERROR: Due to long τ_m and the finite averaging time the measurement consists only of a few independent samples (e.g. 10-20) and $\sigma_{\text{spin-signal}}$ is flawed with a large error. By randomising the ensemble's polarisation several times within a period of τ_m the number of independent samples is increased and the

---

[5]An independent sample is specified by the ensemble's correlation and its characteristic time τ_m.

precision of $\sigma_{\text{spin-signal}}$ is improved [97]. However, the mean values of $\sigma_{\text{spin-signal}}$ and the SNR are not increased thereby.

This randomisation is done by interrupting the continuous spin inversion with pulse trains consisting of several arbitrary RF-frequencies. In doing so, the spins get rotated arbitrarily at different locations and the long correlation is destroyed.

4.2.5 Counteracting Cantilever Frequency Changes

The frequency of the cantilever depends highly on the electrostatic field it is exposed to. The field in turn depends on the topography of the micro-wire chip, which exhibits a very uneven feature with the nano-magnet. Already the smallest changes in position of the chip, e.g. due to drift, alter the electric field significantly. Thereby the tuning of the ARP pulses, which is matched to the cantilever oscillation ($\omega_{2p} \stackrel{!}{=} \omega_{L_0}$), gets off and the spin inversions drive the cantilever less or not any more. The micro-wire chip can drift, since it is moved by means of piezoelectric positioners. Because a piezoelectric disc's elongation does not happen instantaneously, but rather logarithmically in time, a delay of up to minutes happens until it is at rest - a time span which is often too long to wait for. Further, the electric field can also change due to charging effects on the micro-wire chip or the cantilever. While big changes make measurements impossible, sometimes small alterations have to be accepted. But still, over time, the detuning will get too big. In order to counteract this, the measurement is interrupted, f_{L_0} is re-measured and ω_{2p} is adjusted before the measurement is continued. Thereby a long measurement time of e.g. 120 s can be split up in 2 times 60 s.

An alternative way to counteract the change of the electric field is to implement an additional gate on the micro-wire chip, as it is done for the vortex-MRFM chip (chapter 6). With a voltage applied to the gate, which is accordingly adjusted by a PID-control loop, f_{L_0} can be kept constant. Initial application with the vortex-MRFM chip have been successful, before the experiment had to be stopped for other reasons. The application of this method in a completed experiment has been demonstrated by Nichol et al. [56]. In principle, the technique could also be used with the existing micro-wire. Nevertheless preliminary tests have been aborted in regard to the new chip design with the additional gate, which avoids any interference with the ARP pulses.

4.2.6 Navigating Above the Micro-Wire Chip

PRINCIPLE: The ability to precisely position sample against the nano-magnet is essential for doing MRFM. The present setup can be used like an AFM in pendulum geometry, since the cantilever is sensitive to the electric field of the surface it oscillates above. Its frequency f_{L_0} depends on the spatial gradient of the field in oscillation direction (x). The changes in f_{L_0} give then the contrast in the topographical images, as shown in section 4.3.1. Such images are acquired by scanning line-by-line over the surface with

a separation between cantilever tip and surface of typically a few hundred nanometres. Further away the electric field gradient of small features vanishes and they can not be recognised any more.

The small distance demands for a high accuracy of the orthogonal alignment of cantilever and micro-wire chip. A possible small tilt can be compensated by simultaneously adjusting the z-position of the micro-wire chip. Therefore the orientation of the chip's plane is measured with three touch-points (see section 4.3.1) and the according adjustment for a given (x, y)-position is calculated and applied to the z-positioner.

As mentioned f_{L_0} couples to the derivative of the field in x-direction. The thus enhanced sensitivity of edges along y has to be kept in mind while perceiving the images and should already be considered in the design of chip's alignment markers.

ADDITIONAL REMARKS: Non-contact friction drags the lever while scanning, which is the reason why the primary scanning direction has to be perpendicular to the cantilever's oscillation direction. For the same reason images acquired by scanning each line in the same direction, rather than in a zig-zag scheme, are smoother. But even if this is considered, non-contact friction can still distort the cantilever faster than the laser's wavelength can be adjusted by the laser PID-controller. In these cases, the locking of the interferometer signal is lost and has to be set up again. Equilibration of the electric potentials by bringing the lower part of the lever in good contact to the micro-wire can in some situations solve this issue. For wide scan windows it can be reasonable to reduce the scanning speed, which gives the laser PID-controller more time to adjust. It is however a very bad indication if bigger problems due to non-contact friction appear already at the stage of scanning. For the measurement itself, the noise will most probably be too high for achieving a reasonable SNR.

Big scan windows enhance drift due to the big voltage differences applied to the piezoelectric positioners. For the final precise positioning, small windows have to be used. If before a substantially different voltage has been applied, it has to be verified that the drift has been temporised.

4.3 Performing MRFM in Practise

Even if the working principal is clear, in practise, already simple things can become a bit fiddly. This gives the motivation to carry out the necessary *measurement preparation steps* as well as the *procedures to find and optimise the signal* in this section. With a *Rabi oscillation* experiment the magnitude of B_1 can be estimated and it provides an unambiguous proof for a real spin signal. Finally, a brief overview of *MRFM imaging*, the *manipulation spin noise's distribution*, the *storing of spin fluctuations* and the polarisation transfer between different isotopes (*double resonance*) conclude this chapter.

4.3.1 Measurement Preparations

As starting point it is assumed, that the micro-wire chip as well as the cantilever with the attached sample are mounted in the system and that the cantilever is aligned and set up with the laser, as described in section 3.7.1.

MISALIGNMENT CANTILEVER - NANO-MAGNET: Eventually the sample has to be in the right position with respect to the nano-magnet. During the cool-down from room temperature to cryogenic temperature the elements of the microscope shrink unequally causing a distortion of any previous alignment. Therefore the position of the micro-wire chip with respect to the cantilever has to be misaligned under an optical microscope (fig. 4.3) in an experimentally determined way. For the used systems, this misalignment is ~ 35 µm in positive y- and ~ 45 µm in negative x-direction. Thereby at liquid nitrogen temperature the cantilever is within ~ 15 µm of the nano-magnet. Further the cantilever has to be retracted in z-direction by about 200 µm to avoid a crash into the chip during the cool-down.[6]
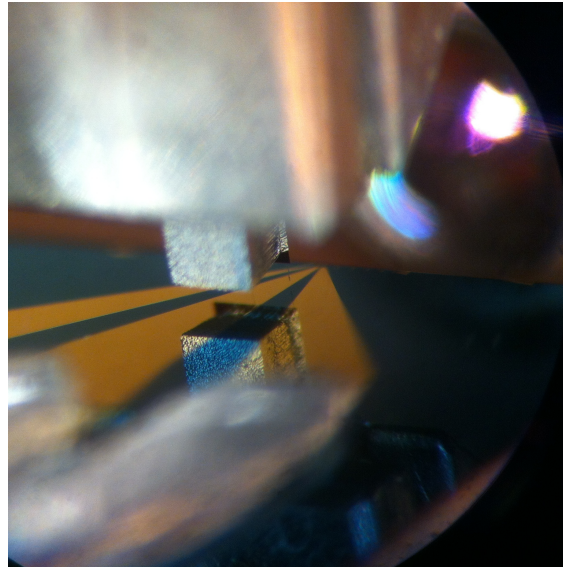
FIGURE 4.3: CANTILEVER AND MICRO-WIRE
Cantilever chip and micro-wire (golden) as seen through an optical microscope during the misalignment. The micro-wire exhibits a third lead in order to minimise non-contact friction and counteract changes in f_{L_0} via V_{bias} (section 3.1.5). In the lower part the mirror image of the cantilever chip visible. The thin cantilever in the gap between the two main leads is not yet in the correct misaligned position.

---

[6]Indeed the cantilever is fixed in space. Only the chip can be moved, even if the description is formulated the opposite way for reasons of convenience.

VERTICAL APPROACH: Monitoring the cantilever frequency f_{L_0} and the oscillation amplitude Δx while coming closer towards the chip ensures a safe approach. When the change of f_{L_0} or Δx exceeds a certain value the approach is stopped. Even a gentle touch does not affect the cantilever or the sample. Since the cantilever is so soft it bends without breaking even if the "approach" continues several tens of microns further[7] than the touch.

ALIGNING AT NITROGEN TEMPERATURE: The previously made misalignment should have brought the cantilever close to the nano-magnet, but the exact position is unknown. Since at 77 K the piezoelectric positioners exhibit a more than 2 times larger scan range than at 4 K, it is mandatory to find the nano-magnet already at this stage. In the worst case this can escalate in a intensive dragnet investigation. Because a simple little dirt grain can have a similar topography than the nano-magnet, an unambiguous identification is important, e.g. by recognising the topography of the surrounding micro-wire. Otherwise any further effort will be in vain. The often vague pictures of the topography as shown in section 4.3.1 are generated as described in section 4.2.6.

   Before cooling down to liquid helium temperature the cantilever is again retracted for safety reasons.

POWERING-ON THE MAGNETIC FIELDS: When the base temperature is (almost) reached but prior to the placing of the cantilever in the measurement position every surrounding effect should to be set to the measurement conditions. The RF-field $\vec{B}_1$ causes significant heating, which clearly affects the alignment of cantilever and nano-magnet. Much less than $\vec{B}_1$ the static magnetic field $\vec{B}_0$ can also cause a shift of the two elements. Both fields have to be powered on before proceeding.

MEASUREMENT POSITION: The best position for a first measurement try is where a high gradient G_{zx} is assumed, the noise, e.g. from non-contact friction is minimal and the spatial gradient of the cantilever frequency is small. This is given in x-direction ~ 50 nm in front of nano-magnet's edge, in y-direction on the centreline of the nano-magnet and in z-direction as close as possible to the top of it, but before the noise starts to increase (e.g ~ 50 to 100 nm from the top) as shown in fig. 4.4.

   For the determination of the separation in z-direction, a gentle touch either on the centre of the nano-magnet or at a specifically chosen position on the micro-wire is made. This can be done either by hand, observing the cantilever displacement spectra on the spectrum analyser, or automatically by measuring f_{L_0} as well as the cantilevers amplitude while approaching and stop when the change of one of them exceeds a certain limit. Measuring the *touch-point* on the centre of the nano-magnet is faster, since no large displacement inducing drift is introduced. Though it can be less precise due to

---

[7]About half of the cantilever length is unproblematic.
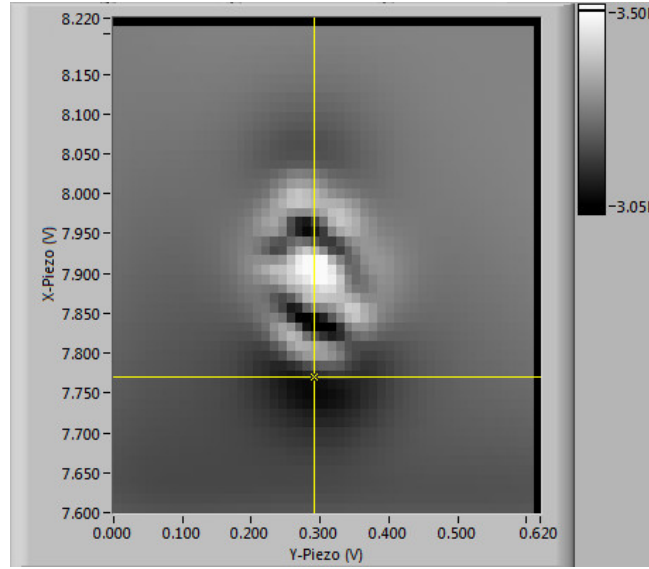
FIGURE 4.4: INDICATION OF OPTIMAL MEASUREMENT POSITION
2D frequency scan picture ~ 50 nm above the magnet with an indicated measurement position (from the LabView controls). The levels of grey reflect the cantilever's frequency f_{L_0}. The picture's details can vary significantly for little changes in cantilever – surface separation. Moreover, since they are a deconvolution of the tip (sample) and the surface objects (nano-magnet), they depend on the shape of the sample. (For more precise 2D-surface-imaging a sharper tip would be needed.) The indicated position is a starting point for the signal optimisation.

possibly too strong electrostatic interaction spoiling the determination. In these cases the touch-point on the micro-wire is chosen.

4.3.2 Finding and Improving the Signal

MAGNETIC RESONANCE FREQUENCY SWEEPS: The first measurement in order to find a magnetic resonance response of the sample is usually to vary the centre f_{centre} of the ARP pulse with RF-frequency f_{RF} and set all other variables to estimated values. Based on a guess of the lower and upper boundary of the tip field $B_{z_{\text{tip}}}$ (typically $\sim 150 - 300$ mT), f_{res} is calculated according to $f_{\text{res}} = \gamma/(2\pi) \cdot (B_0 + B_{z_{\text{tip}}})$. The *resonance frequency sweep*[8] measurement consists of a series of single measurements starting with f_{centre} far below and sweeping it to well above the range where f_{res} is assumed. Off resonance σ_{ip} and σ_{qd} are approximately equal. Matching the resonance, σ_{ip} raises,

---

[8]The expression *resonance frequency "sweep"* can be confusing since finally it is a sweep a swept frequency. It is used for historical reasons. Within an ARP pulse, $f_{\text{RF}}(t)$ is varied to invert the spins, the pulses are repeated and the signal is averaged for a time t_{aqui}. Now, the centre frequency f_{centre} of the ARP pulses is varied (i.e. swept) for several consecutive measurements with duration t_{aqui}.

whilst σ_{qd} ideally stays the same as shown in fig. 4.5. A possible increase of σ_{qd} might be due to an incorrect set phase of the lock-in amplifier and can be accordingly corrected (see paragraph *Sweep Parameters Optimisation* below). The several blank measurements off resonance give indication of absent artificial driving, e.g. by a possible existing electric component of $\vec{B}_1$. A resonance frequency sweep measurement usually takes a bit more than one to several hours, depending on the range over which f_{centre} is swept, the averaging time t_{aqui} and the interval size.
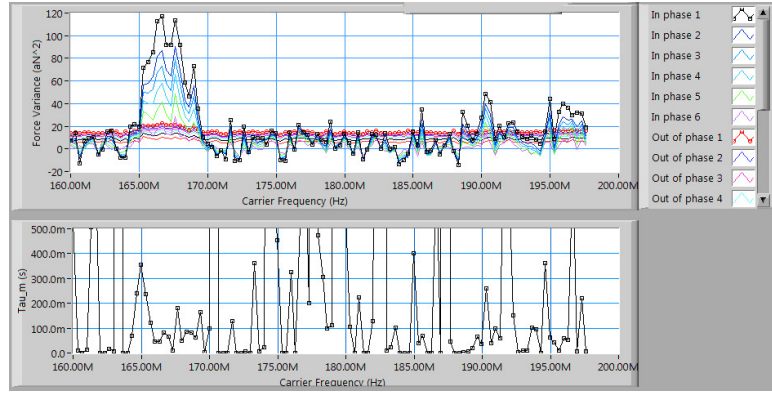
FIGURE 4.5: A RAW MRFM SIGNAL – FINALLY
Magnetic resonance frequency sweep traces. *Upper graph:* Variance of the magnetic force (In phase 1 to 6; black and blueish to greenish curves) versus the carrier frequency alias centre frequency f_{centre}. The reddish flat curves (out of phase 1 to 6) reflect the uncorrelated thermal noise. The each 6 curves correspond to different bandwidth filters. The decomposition of the raw signal this way enables the instantaneous determination of τ_m (section 4.2.3). The smaller peaks at higher frequencies are spurious excitations of the cantilever. *Lower graph:* Spin ensemble correlation time τ_m versus f_{centre}. On resonance (165 MHz to 170 MHz) values between ~ 100 ms to ~ 300 ms are measured. Away from resonance the fit based on the different filters is erroneous and crazy values result.

If the sweep reveals no resonance signal a new position (primary different in x, maybe in z) is chosen and the resonance frequency sweep is repeated with the same parameters. This makes sense, since knowing empirical values for $B_{z_{\mathrm{tip}}}$, B_1, Δf_{mod} and β_{HS}[9], the biggest unknown is G_{zx}, which is determined by the position and can easily be too small to not find a measurable signal at all at the chosen position.

If this is still not successful, the other variable parameters are changed similar to the optimisation description below, e.g. in the following order B_1, Δf_{mod}, β_{HS}, and even more positions are tested, e.g. also by spatial scans.

---

[9]β_{HS} is the truncation factor of the hyperbolic secant ARP pulse as described in section 2.2.

SWEEP PARAMETERS OPTIMISATION: Once a resonance signal, i.e. f_{res} for a given position is found, the other parameters of the ARP pulses are optimised. Therefore sweeps of one of the variables $B_1, \Delta f_{\text{mod}}, \beta_{\text{HS}}$ are made, whilst the others and f_{centre} are set to a fixed value.

Changing Δf_{mod} and β_{HS} in a moderate range[10] is unproblematic and optimal settings can easily be found. Though, varying B_1 changes the power of the RF-pulse and thus the heating produced by the micro-wire. This in turn can change the position of the sample relative to the nano-magnet, which has to be considered especially if B_1 is swept over a large range. Even if the change in position is small and intentionally neglected, f_{L_0} still changes. It can take up to a few seconds until the changes are equalised. Therefore a waiting time after the update of ω_{RF} and before measuring f_{L_0} is introduced. If necessary this is also done for variations of parameters other than B_1.

If σ_{qd} shows an increase on resonance, also the phase between the driving of the spins via the ARP pulses and the detection by the lock-in amplifier has to be optimised. With an internal function of the lock-in amplifier the best phase, yielding the highest difference between σ_{ip} and σ_{qd}, can be evaluated. The settings of this function are limited and also off resonance, where only thermal noise is present, the optimal phase is evaluated, spoiling the proper measurement of $\sigma_{\text{spin-signal}}$. Hence it is only suitable to find the optimal phase. In any case, the actual measurement of $\sigma_{\text{spin-signal}}$ has to be remade with a fixed phase. By using a four-channel detection scheme as demonstrated by Moores et al. [18, 156] the evaluation of the phase can be done with external computing software enabling more customisation and yielding more complete information of the signal.

SPATIAL SCANS: In order to find the position with the highest gradient a spatial scan over the half or the full width of the tip is made. Therefore a distinct f_{centre} is set and the position is typically swept in x-direction. Changing the position alters the cantilever's interaction with its environment and introduces a considerable delay until f_{L_0} is again stable. This is accounted for in a similar way to the above mentioned RF update waiting time; although here it can be up to a few minutes.

Further, also the damping due to non-contact friction can vary, which changes Q_{damped} and thereby the conversion from displacement to force. Ideally, each time the new Q_{damped} should have to be measured by the ring-down method, which is not done in our case.

4.3.3 Rabi Oscillations

The magnitude of B_1 can be determined by modifying the standard continuous spin inversion protocol and forcing the spins to nutate as described by Poggio et al. [142].

---

[10]Setting β_{HS} to a very low value increases the power of $\vec{B}_1$ and thereby the heating significantly, which introduces the same problems as changing the magnitude B_1.

Thereby the continuous spin inversion is repeatedly interspersed with a nutation pulse after a period much shorter than τ_m. The nutation pulse has a constant frequency $f_{RF} = f_{res}$ and a constant amplitude B_1, but is of variable length $t_{Nutation}$. The continuous spin inversion however is always interrupted for a full period T_{L_0} of the cantilever oscillation. Increasing $t_{Nutation}$ induces the spins to nutate with increasing angle. When $t_{Nutation} = \pi/(\gamma B_1)$, each nutation pulse inverts the spins, but rather within T_{L_0} than within $T_{L_0}/2$. This reverses the sign of the force driving the cantilever. Repeatedly applied, the driving force's modulation results into sidebands in the cantilever frequency spectrum. When $t_{Nutation} = 2\pi/(\gamma B_1)$, the spins nutate by 2π and $\sigma_{spin\text{-}signal}$ reaches again a reduced maximum. Increasing $t_{Nutation}$ further and plotting $\sigma_{spin\text{-}signal}$ against $t_{Nutation}$ results in a cosinusoidal Rabi oscillation with decaying envelope. The magnitude of B_1 at the position of the sample can thereby be estimated by $B_1 = 2\pi/(\gamma t_{2\pi-Nutation})$.

This investigation gives unambiguous proof that $\sigma_{spin\text{-}signal}$ is caused by spins. Other effects driving the cantilever in a deceptive way can thereby be excluded.

4.3.4 Imaging

To produce a spatial image of the sample's spin density the sample is scanned in three dimensions over the nano-magnet. The measured signal for each point originates from the arbitrary shaped intersection volume of the sample with the resonance slice. A map of the signal strength depending on the samples position is thereby obtained. Because of the extended geometry of the resonance slice, this is not a real space 3D image of the spin distribution, It is rather a convolution of the point spread function associated with the resonance slice and the real space image. To obtain the latter, the map has to be deconveluted as described e.g. by Degen et al. [99]. MRFM imaging has been demonstrated in several experiments [62, 64, 68, 90, 99]. The highest resolution achieved so far is in the range of 4 to 10 nm [99].

4.3.5 Further Applied MRFM Methods

The capabilities of MRFM extend the ability of measuring spin noise and produce spatial images of the nuclear spin density. In principle most of the spin manipulation techniques developed and well-tried by the NMR community could possibly be adapted to MRFM. Even tough some would need modifications in the setup as e.g. a magnetic field gradient that can be switched off or a second RF-field perpendicular to $\vec{B}_1$. Three applied MRFM methods, which have been examined during this work are discussed in the following.

MANIPULATION THE SPIN NOISE'S DISTRIBUTION: The spin noise responsible for the statistical polarisation of an ensemble naturally follows a distribution determined by statistical mechanics. By observing the trace of the ensembles magnetisation M_z in real time and applying well timed modified ARP pulses, $M'_z s$ distribution can be

manipulated [61, 103]. In classical MRFM the spins are inverted twice per cantilever oscillation by a pair of two ARP pulses forming a 2π pulse. By applying only a π pulse within the oscillation period T_{L_0}, i.e. one ARP pulse with $t_p = T_{L_0}$ instead of two with $t_p = 1/2T_{L_0}$, the sign of the spin fluctuation is inverted. If this is done each time M_z exceeds or falls below a certain threshold, the natural Gaussian distribution of M_z is narrowed and σ_{M_z} is reduced. Similarly, the distribution can be shifted yielding the averaged magnetisation $M_z \neq 0$, or it can be broadened.

The method finds application e.g. in reducing dephasing in quantum dots [157].

STORING SPIN FLUCTUATIONS: By interrupting the continuous spin inversions statistical polarisations can be stored and recaptured for several seconds [61, 103]. This is possible since the spin-lattice relaxation time T_1 is bigger than the spin-lattice relaxation time in the rotating frame $T_{1\rho}$ and the ensemble spin correlation time τ_m. As for the manipulation of the noise's distribution above, the trace of M_z is observed in real time. Now, the ARP pulses are interrupted when a bigger polarisation than the statistical average is measured. When restarted after a certain time t_{storage}, whereas $T_{1\rho} < t_{\text{storage}} < T_1$, the polarisation is found to be still as high as before. It is only[11] reduced by the - in semiconductors - slow T_1 decay. The ability to manipulate and store polarisations of small spin ensembles is important for future development of MRFM and possibly for the implementation of solid-state spin qbits.

This technique builds the base for the experiment presented in chapter 5 and in the publication by Herzog et al. [104].

DOUBLE RESONANCE: Polarisations of different isotopes (i) in a sample can be transferred by tuning the particular Larmor frequencies[12] $\omega_{\text{Larmor},i}(t) = \gamma_i |\vec{B}_0 + \vec{B}_{1,i}(t)|$ to be the same when the spins are in the x, y-plane of the Bloch sphere during the ARP. In this situation, $\vec{B}_0$ is compensated by the AC-component of $\vec{B}_{1,i}(t)$, i.e. $\vec{\omega}_{0,i} = \vec{\omega}_{\text{RF},i}$ and $\vec{B}_{\text{eff},i} = \vec{B}_{1,i}$. The thereby established criteria is known as the Hartmann-Hahn condition: $\gamma_I B_{1,I} = \gamma_S B_{1,S}$, whereas the indices I and S denote the two isotopes. By bringing the two spin species into contact, the polarisations equilibrate in analogy to a thermal bath, and a possibly higher polarisation of one of the isotopes enhances the other.

The technique is called double resonance or cross-polarisation and was already pointed out by Bloch in the earliest reflections about magnetic resonance [2]. It is widely used in NMR to enhance signals of isotopes with low γ and low abundance (e.g. ^{13}C or ^{15}N) and is part of most of the advanced NMR pulse sequences [158–161].

---

[11]The measurement observable Δx is additionally reduced by a noise contribution inherent to the measurement process.

[12]The pulse field $\vec{B}_{1,i}(t)$ has only an effect on the spins and adds up to $\omega_{\text{Larmor},i}(t)$ if its frequency $\omega_{\text{RF},i}(t)$ is tuned to the according isotope i.

Double resonance can not only be used for thermal or other kind of polarisations, it can also be applied to statistical polarisations in MRFM. Poggio et al. demonstrated the reduction of the statistical polarisation of one spin species due to this effect [98].

In principle, double resonance can also be combined with the technique of storing and recapturing statistical fluctuations. A high statistical spin polarisation of one isotope will thereby be transferred to another isotope and the enhanced polarisation will be measured there. An experiment with KPF_6 with the focus on doing a transfer between fluorine and phosphorus has been initiated, but due to technical reasons[13] no successful measurements could be made.

---

[13]RF reflections in the micro-wire causing the power of B_1 and the heating to frequency depending.

5 Thermal versus Statistical Polarisation

> *Das Leben ist werth gelebt werden, sagt die Kunst, die schönste Verführerin;*
> *das Leben ist werth, erkannt zu werden, sagt die Wissenschaft.*

Friedrich Nietzsche, *Homer und die klassische Philologie,*
Antrittsvorlesung in Basel, 1869

This chapter reflects and extends the experiments presented in the article

Boundary between the thermal and statistical polarisation regimes
in a nuclear spin ensemble
by *B. E. Herzog, D. Cadeddu, F. Xue, P. Peddibhotla, and M. Poggio*
published in *Applied Physics Letters 105, 043112 (2014)* [104].

5.1 Introduction

Nanometre-scale spin ensembles differ from larger ensembles in that random fluctuations in the total polarisation – also known as spin noise – exceed the normally dominant mean thermal polarisation. This characteristic imposes important differences between nano-MRI and conventional MRI protocols. In the former technique, statistical fluctuations are usually measured, whereas in the latter the signal is based on the thermal polarisation [2, 97, 103]. Here, the nuclear polarisation of nanometre-scale volumes of ^{19}F spins using MRFM is studied. Thereby, the focus lies on the transition between the regimes in which thermal and statistical polarisation dominate.

The thermal polarisation – also known as Boltzmann polarisation – results from the alignment of nuclear magnetisation under thermal equilibrium along a magnetic field. The statistical polarisation, on the other hand, arises from the incomplete cancellation of magnetic moments within the ensemble. Depending on the number N of spins and the time it takes to reach thermal equilibrium, i.e. the longitudinal relaxation time T_1, either one or the other type of polarisation is more advantageous to measure. In cases where both, the statistical and the thermal polarisation, can be measured simultaneously,[1] this method enables a simple manner to determine N and subsequently the ensemble's

---

[1]Here, simultaneously means within the same measurement sequence, but not at the very same time.

volume. Furthermore it is much less flawed than the usual method, based only on the statistical polarisation (eq. (4.9) in section 4.1.5).

The chapter gives at first an explanation of the origin and characteristics of the two types of polarisation. Subsequently the experimental details are carried out, followed by the presentation of the results and their discussion.

5.2 Polarisation Types

5.2.1 Thermal Polarisation

The thermal polarisation results from the establishment of a thermal equilibrium of nuclear spins interacting with a magnetic field B_z, here set along the z-direction. The interaction can be described by the Hamiltonian (section 2.1)

$$\hat{H} = -\hat{\mu}_z B_z = -\hbar\gamma\hat{I}_z B_z \quad , \qquad (5.1)$$

where $\hat{\mu}_z$ is the magnetic dipole operator, $\hat{I}_z$ the z-component of the nuclear spin operator with the according eigenvalues $m_s = \{I, I-1, \ldots, -I\}$ and I is the spin quantum number. The eigenvalues define the separated energy levels on which the spins in the ensemble distribute:

$$E_m = -\gamma\hbar B_z m_s \qquad . \qquad (5.2)$$

How the spins arrange on these energy levels at given temperature T and magnetic field B_z is described by statistical mechanics as a Boltzmann distribution. Therefore the probability $P(E_m)$ that a spin has the eigenenergy E_m is proportional to the Boltzmann-factor,

$$P(E_m) \propto e^{\frac{E_m}{k_B T}} \quad , \qquad (5.3)$$

resulting in an unequally distributed arrangement. The difference in the population of spins with positive and negative energies E_m leads to a mean magnetisation M_z along the direction of the applied field – the thermal polarisation.

In order to calculate the expectation value of M_z, it is convenient to use the concept of the density matrix $\hat{\rho}$ [5, 102]. It is given as $\hat{\rho} = 1/Z \cdot e^{-\hat{H}/k_B T}$, whereas Z is the partition function $Z = \text{Tr}\left\{e^{(-\hat{H}/k_B T)}\right\}$ [5, 102]. Since the dipolar coupling of nuclear spins is much weaker than the interaction with the here applied magnetic field, spin-spin coupling can be neglected (see section 2.1.2). Therefore the single spin Hamiltonian holds unchanged also for the ensemble: $H = -\hat{\mu}_z B_z$. The mean magnetisation M_z of N spins is now given as $M_z = N \text{Tr}\{\hat{\mu}_z\hat{\rho}\}$. This expression can be simplified by Taylor-expanding it and considering that the thermal energy even at cryogenic temperatures ($T \sim 5$ K) and high magnetic fields ($B_z \sim 5$ T) is much larger than the nuclear Zeeman splitting, i.e. $\hbar\gamma B_z \ll k_B T$. In doing so higher orders of $\hbar\gamma B_z/k_B T$ beyond the first can

be neglected and we obtain:

$$M_z = N \frac{I(I+1)}{3} \left(\frac{\hbar \gamma B_z}{k_B T} \right) \hbar \gamma \quad . \tag{5.4}$$

It is useful to express the magnetisation as relative quantity by comparing it to a fully polarised system with magnetisation $M_{100\%} = N\hbar\gamma I$. This gives the relative thermal polarisation $P_{\text{th}} = \frac{M_z}{M_{100\%}}$,

$$\boxed{P_{\text{th}} = \frac{I+1}{3} \frac{\hbar \gamma B}{k_B T}} \quad . \tag{5.5}$$

It shall be emphasised, that P_{th} is independent of the ensemble size N, which is a crucial difference in comparison to the statistical polarisation, as will be seen in the following section.

5.2.2 Statistical Polarisation

The spins distributed on different energy levels E_m can undergo spontaneous transitions from one to an other state by absorbing, respectively emitting energy to the thermal bath, since the thermal energy is much larger than the difference between the levels, as noted before. The transitions happen randomly and in thermal equilibrium they are eventually compensated by an opposite transition, establishing in average again the equilibrium. Though the balancing does not happen instantaneously causing a permanent fluctuating deviation from equilibrium, which is called spin noise or statistical polarisation. The time scale on which the fluctuations happen depends on the flip rate of the spins [102], which is orders of magnitude shorter than the required averaging time. These fluctuations of an ensemble's magnetisation M_z cause a non-zero standard deviation σ_{M_z}, which is the measurement quantity in nanoscale MRFM. Usually, σ_{M_z} is recorded and averaged over several seconds in order to reduce the measurement noise and achieve an evaluable signal, but the fluctuations in M_z can still be observed in real time.

As for the magnetisation due to the thermal polarisation, the standard deviation of M_z can be calculated by help of the density matrix formalism [5, 102]. The variance $\sigma_{M_z}^2$ is given as $\sigma_{M_z}^2 = N \left(\text{Tr} \{ \hat{\mu}_z^2 \hat{\rho} \} - \left(\text{Tr} \{ \hat{\mu}_z \hat{\rho} \} \right)^2 \right)$. Applying again the same approximation as above, we finally get for the standard deviation:

$$\sigma_{M_z} = \sqrt{N \frac{I(I+1)}{3}} \hbar \gamma \quad . \tag{5.6}$$

The relative statistical polarisation $P_{\text{stat}} = \frac{\sigma_{M_z}}{M_{100\%}}$ reads consequently:

$$\boxed{P_{\text{stat}} = \sqrt{\frac{I+1}{3I} \frac{1}{N}}} \quad . \tag{5.7}$$

In contrast to the thermal polarisation, the statistical polarisation does neither depend on magnetic field B_z nor on temperature T. Though it is depending on the ensemble size N and as absolute value on the magnetic moment.

Several MRFM experiments have detected statistical polarisations of nuclei with spin-½ [97, 98, 100, 142, 162, 163] and spin-³⁄₂ [102].

5.2.3 Comparing the two Polarisations

Comparing the thermal polarisation with the statistical polarisation shows as depicted in fig. 5.5, that for big ensemble sizes P_{th} is clearly larger than P_{stat} since M_z scales with N whereas σ_{M_z} with $\sqrt{N}$. For this reason in macroscopic, clinical MRI usually M_z is the measurement quantity. Going to smaller detection volumes the size of the magnitude of σ_{M_z} becomes not only relatively bigger but eventually also exceeds absolutely the magnitude of M_z. The critical number of spins N_c where this transition occurs is set by the condition $M_z/\sigma_{M_z} = 1$. Hence,

$$N_c = \frac{3}{I(I+1)} \left(\frac{k_B\, T}{\hbar \gamma B} \right)^2 \quad .$$ (5.8)

Though the ensemble size where it becomes more favourable to measure the statistical rather than the thermal polarisation is not only set by N_c. In practise already for volumes where $N > N_c$, the use of σ_{M_z} as measurement quantity is advantageous. Any physical measurement is always comparative, contrasting a value with a bare probe or opposite value. Measuring thermal polarisation requires to let the system establish the thermal equilibrium, for several independent measurements accordingly many times. Its build-up is characterised by the longitudinal relaxation time T_1. Generally, to specify the measurement time not only the averaging time during which the signal is recorded, but also the preparation time, which includes T_1, has to be considered. For hydrogen atoms in biological tissues and liquids T_1 is in the order of 0.1 to 2 s. But in semiconductors T_1 is expected to reach from several seconds to minutes. Measurement repetition and scanning point per point in imaging applications multiplies T_1 and therefore enhances the required time gravely. On the other hand, measurement protocols based on statistical polarisation do not include any subsequence similar to the waiting for establishment of thermal polarisation. σ_{M_z} fluctuates permanently due to the exchange with the thermal bath on a timescale much faster than the averaging time. Independent measurements on spin noise are separated by the ensemble's correlation time τ_m, which is in the order of hundreds of milliseconds (section 4.2.3). Considering the whole effort, depending on the measurement protocol, statistical polarisation does exhibit a distinct temporal benefit for small volumes emphasising anew its importance in the nanometre regime.

5.3 Experiment

5.3.1 Methods

The description of the experimental apparatus and the general principles of MRFM are carried out in chapters 3 and 4. Pictures of the microscope's core are shown in figs. 3.8 and 3.9. In the following the specific experimental details, especially the measurement to measure both, thermal and statistical polarisation, are described.

SAMPLE AND MEASUREMENT CONDITIONS: The $1.2 \times 1.4 \times 3.2$ µm^3 sized sample is made by milling polycrystalline powder of KPF$_6$ between two glass slides into smaller grain sizes. It is glued to the end of an ultra-sensitive Si cantilever which transduces the magnetic force into a displacement. The attachment follows the procedure described in section 3.2. To reduce non-contact friction due to electrostatic interactions between the magnetic tip and the sample (section 3.1.5), a 15 nm thick layer of Au is evaporated on the sample after attachment.
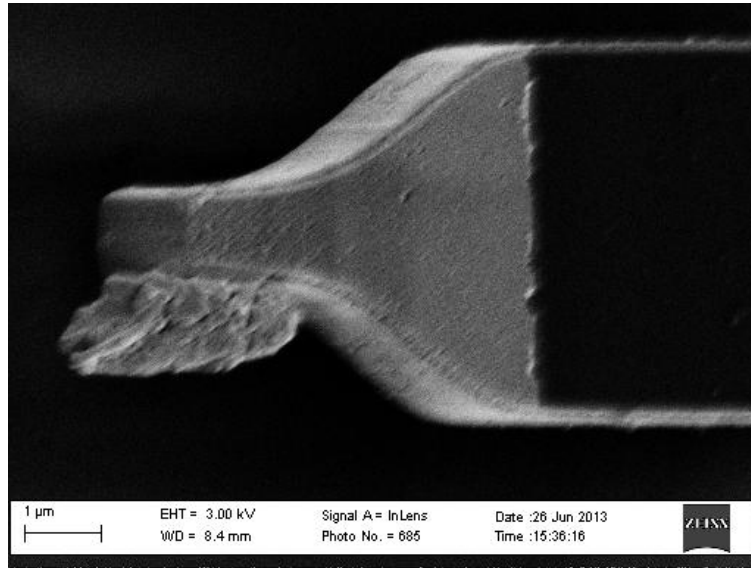
FIGURE 5.1: KPF$_6$ SAMPLE
The $1.2 \times 1.4 \times 3.2$ µm^3 sized sample glued to the cantilever's tip and covered with a 15 nm thick gold layer (bright) to reduce non-contact friction. The picture was taken after the finished experiment.

The cantilever is 130 µm long, 4 µm wide, 0.1 µm thick and has a spring constant $k = 75$ µN/m, as determined by thermal noise measurements at various temperatures (section 3.1.4). In the cryogenic measurement chamber at $T = 4.4$ K, with an applied external magnetic field $B_0 = 6$ T along the z-direction and in a vacuum better than 10^{-6} mbar, the sample-loaded cantilever has a mechanical resonance frequency $f_{L_0} = 3.28$

kHz and a quality factor $Q = 3.1 \times 10^4$. In the subsequently described experiment a lower field of $B_0 = 4.37$ T is applied. During the measurement the cantilever is damped using electronic feedback to a quality factor $Q = 400$ in order to increase the minimal bandwidth $\Delta f_{\text{BW}_{\text{min}}}$ of our force detection without sacrificing force sensitivity (section 4.2.1 and [105]).
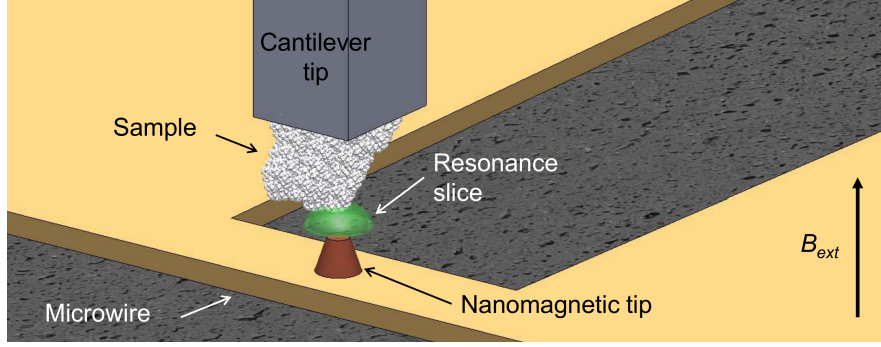
FIGURE 5.2: SCHEMATIC SET-UP
The experimental setup with the poly-crystalline KPF$_6$ sample (white) at the end of the cantilever. A small section of it intersects with the resonance slice (green) above the nano-magnet. The micro-wire produces the transverse RF magnetic field used to adiabatically invert the nuclear spins.

MRFM PRINCIPLE: In order to measure the signal of nuclear spins the sample attached to the cantilever's tip is positioned in a gradual magnetic field $\vec{B}_{\text{tip}}$ and the spins are inverted by a magnetic AC field $\vec{B}_1$, synchronised with the oscillation of the cantilever. A nano-magnetic tip serves as source for $\vec{B}_{\text{tip}}$ (section 3.5). It is placed on top of a micro-wire which provides $\vec{B}_1$ (section 3.4). By a superconducting external magnet a large static magnetic field $\vec{B}_0$ is applied in z-direction (section 3.6), hence the total static field in z direction is $B_z = B_0 + B_{\text{tip}_z}$. To generate the $\vec{B}_1$ field a current with a frequency sweep waveform, designed as adiabatic rapid passage (ARP) pulses, is driven through the micro-wire (section 3.3). At the sample's position, the circular $\vec{B}_1$ field is pointing in x-direction perpendicular to $\vec{B}_0$ whereby the spins oriented parallel and anti-parallel to $\vec{B}_0$ are inverted adiabatically. The ARP technique is described in detail in sections 2.2, 4.1.1 and 4.1.3.

Between the magnetic moment $\vec{\mu}$, originated in the spins, and the gradual field acts an alternating force according to $\vec{F}(t) = \nabla \left(\vec{\mu}(t)\vec{B} \right)$ depending on the inversion of the spins. By means of the cantilever, $\vec{F}(t)$ is transduced in a displacement $x(t)$ which is measured by an laser interferometer and filtered out of the uncorrelated noise by a lock-in amplifier.

The cantilever's direction of oscillation along x makes it essentially sensitive to forces and thereby also to the spatial derivative along this direction. As carried out in

section 4.1.2 and appendix A.3, the alignment of $\vec{\mu}$ along z eventually makes $F_x(t)$ depending on the derivative of the z-component of the magnetic field: B_z. The determining component of the force caused by a single spin with μ_z is given by $F_x(t) = \mu_z(t)^{\partial}/\partial x B_z$. Finally, for an ensemble of spins with M_z, the ensemble's magnetisation in z-direction and the gradient $G_{zx} \equiv \partial B_z/\partial x$, the force is given as already introduced in section 4.1.2 by equation (4.3)

$$F_x(t) = M_z(t)\frac{\partial B_z}{\partial x} = M_z(t)G_{zx} \quad .$$

(5.9)

From $F(t)$ the average force F and its standard deviation σ_F over fixed time intervals are derived.

MEASUREMENT SEQUENCE: In order to measure the size of the thermal nuclear polarisation, first the spins are initialised to a mean polarisation of zero. This is done by applying the ARP pulse sequence with its carrier frequency set to $f_{\text{res}} = \gamma B_z$, the NMR frequency of the nuclear spins of interest. During the application of the resonant ARP pulses, the correlation time τ_m of the nuclear spins (section 4.2.3) is short relative to the spin-lattice relaxation time T_1, $\tau_m \ll T_1$. Here it is estimated to be $\tau_m \approx 200$ ms. Therefore, by applying resonant pulses for a time $t_{\text{init}} \gg \tau_m$, the initial thermal polarisation is erased, leaving only the statistical polarisation fluctuations.

At $t = 0$ the carrier frequency is changed to $f_{\text{off-res}} \sim 7$ MHz far from f_{res}, as shown in fig. 5.3(A). During this off resonant time t_{pol}, the spin ensemble polarises along the magnetic field B_0 with a characteristic time T_1. The principal concept is to turn the inversion off, have no more driving of the spins and let them align with $\vec{B}_0$. This could simply be done by turning the B_1 field off. The reason for instead tuning it away, is to sustain the thermal equilibrium of the setup. The change in temperature produced by the B_1 field lies in the order of 10 to 100 mK, which would alter the alignment of sample to nano-magnet significantly.

When tuning the ARP pulses back on resonance at t_{pol} the force $F_{t_{\text{pol}}}$ reflects the built-up magnetisation M_z. The signal rises[2] with the time constant of the lock-in amplifier, $t_{\text{lock-in}} \sim 300$ ms and decays again due to the persistent application of the on resonant ARP pulses. The measured peak[2] value is already reduced by the decay during $t_{\text{lock-in}}$. The real thermal magnetisation at t_{pol} of the ensemble is $M_z = {}^{M_{z\,\text{measured}}}\!/\!\left(1 - e^{-t_{\text{lock-in}}/\tau_m}\right)$, a factor of ~ 1.3 bigger than the measured value. This deviation was uncovered after the publication and is thus not considered in the presented data. It affects the listed values of F in figs. 5.3 and 5.4 and the numbers of measured spins, respective the measurement volumes (text and fig. 5.5), but it does not influence the reported T_1 values (eq. (5.10)). The statistical fluctuations accounting to a single measured value of σ_{M_z} are averaged to zero by the repetitions and do not change the measured M_z.

---

[2] Here, the figures show a dip. For convenience the terminology *rising*, respectively *peak* is used.

By recording the standard deviation of the resonant force σ_F during the same time, the effect on the ensemble's statistical fluctuations σ_{M_z} is also measured. The curve of σ_F is constant apart from a single step at t_{pol}.

This is the basic measurement sequence which is repeated 500 times and averaged yielding a single signal trace for the pair of F and σ_F as shown in fig. 5.3(B).
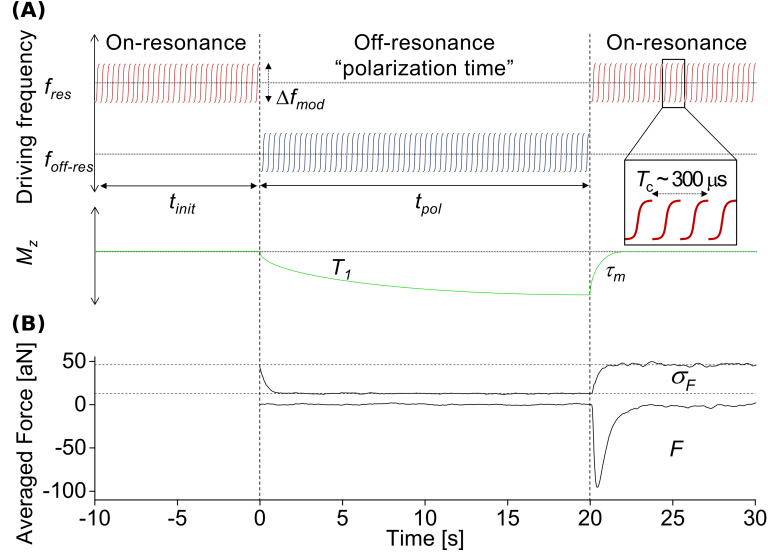
FIGURE 5.3: BASIC MEASUREMENT SEQUENCE AND SIGNAL TRACES
(A) Schematic diagram of the pulse sequence and the response of the average nuclear magnetisation M_z. The pulse spacing has been exaggerated for clarity. **(B)** F and σ_F averaged over 500 measurements for $t_{\mathrm{pol}} = 20$ s and $\Delta f_{\mathrm{mod}} = 3$ MHz. The fast decay of F after the pulses are switched on resonance is due to the correlation time τ_m of the spins during the ARP pulses.

By allowing the off resonant condition to persist for a variety of different t_{pol} before tuning the ARP pulses back on resonance and measuring the resulting $F_{t_{\mathrm{pol}}}$, the build-up of the ensemble's thermal polarisation is measured as shown four times in fig. 5.4. The magnitude of the standard deviation σ_F before and after the switch from off- and on resonance, and therefore also the step size $\Delta\sigma_F$ are independent of t_{pol}.

$F_{t_{\mathrm{pol}}}$ follows the simple exponential law

$$F_{t_{\mathrm{pol}}} = F_0 + F_{\max} e^{t_{\mathrm{pol}}/T_1} \quad . \tag{5.10}$$

Fitting $F_{t_{\mathrm{pol}}}$ for different t_{pol} with this curve the spin-lattice relaxation time T_1 as well as the full thermal magnetisation for infinite time can be extracted. F_0 proves to be zero, as expected.

Different ensemble sizes are addressed by changing the frequency modulation amplitude (modulation width) Δf_{mod} of the ARP pulse sequences. The thickness of the
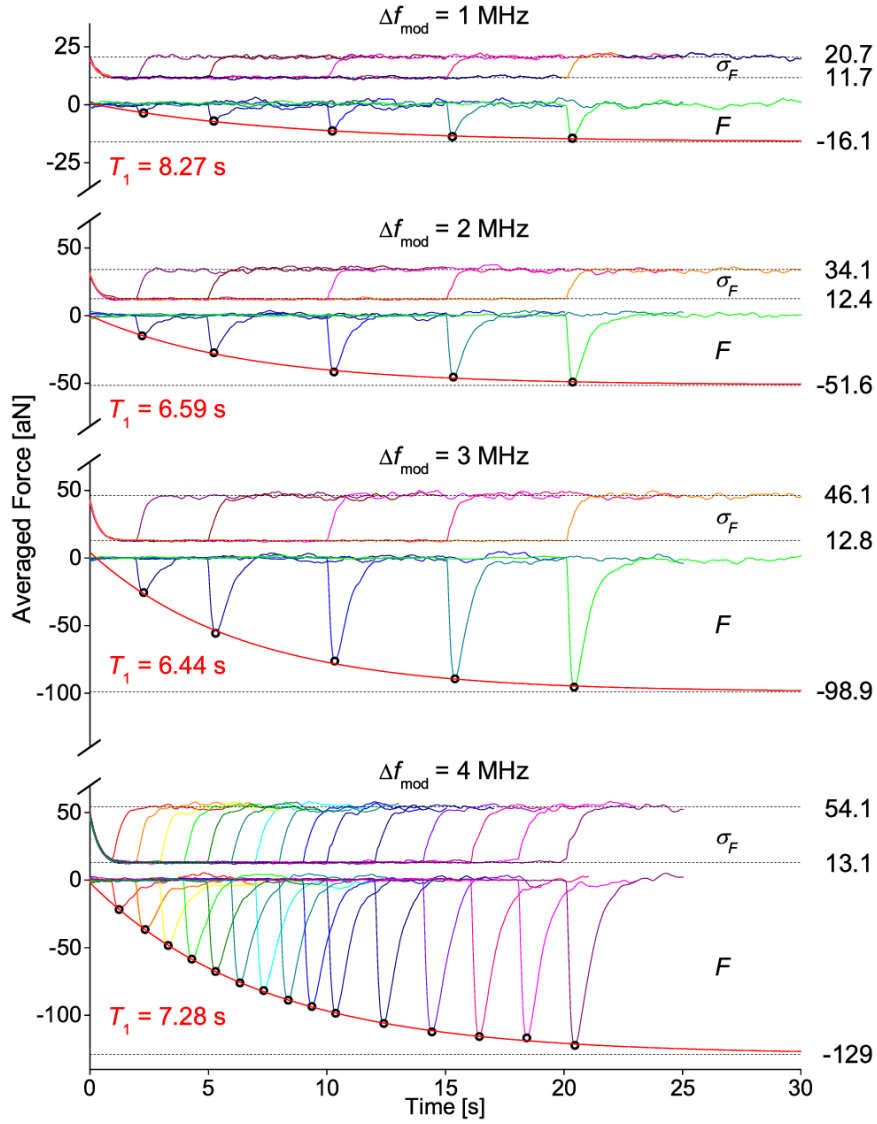
FIGURE 5.4: MEASUREMENTS OF T_1 FOR DIFFERENT ENSEMBLE SIZES
F and σ_F averaged over 500 measurements at $B = 4.37$ T and $T = 4.4$ K for different modulation widths $\Delta f_{\text{mod}} = \{1, 2, 3, 4\}$ MHz of the ARP pulses. Each graph shows F in the lower part, reflecting the thermal polarisation, and σ_F in the upper part, reflecting the statistical polarisation, for a series of different polarisation times t_{pol}. Only at $t = t_{\text{pol}}$ (black circles), when the ARP pulses are turned back on resonance, is F related to the thermal spin polarisation. During the polarisation time ($t < t_{\text{pol}}$) $\sigma_F = \sigma_{\text{F-cant}}$, while on resonance ($t > t_{\text{pol}}$) spin noise also contributes, i.e. $\sigma_F = \sqrt{\sigma_{\text{F-spin}}^2 + \sigma_{\text{F-cant}}^2}$.

resonant slice (section 4.1.2) depends due to the gradual field and via the resonant

condition $f_{\text{res}} = \gamma B_z$ on B_1. For the small volumes G_{zx} is nearly constant and therefore the resonant slices volume of intersection with the sample is roughly proportional to Δf_{mod}. The above described sequence for a fixed modulation width is carried out for $\Delta f_{\text{mod}} = [1, 2, 3, 4]$ MHz. The corresponding traces of F and σ_F for the four different ensemble sizes are shown in fig. 5.4. These measurements are performed at $B_0 = 4.37$ T and $T = 4.4$ K, the on- and off-resonant carrier frequencies are $f_{\text{res}} = 175$ MHz and $f_{\text{off-res}} = 168$ MHz respectively.

FORCE DISTINCTION AND CONVERSION: So far, only the measured quantities, i.e. the mean and standard deviation of the entire force acting on the cantilever, $F(t)$ and $\sigma_F(t)$ respectively, are discussed. In general they contain also thermal and other noise, additionally to contribution from the spin ensemble's magnetisation, M_z.

Since the thermal noise force is uncorrelated its mean value is zero. As it can be seen in figs. 5.3 and 5.4, $F(t) = 0$ for $t < t_{\text{pol}}$ and $t \gg t_{\text{pol}}$. Hence the only contributing part of $F(t)$ comes from the magnetisation of the sample:

$$F(t) = M_z(t)G_{zx} \quad . \tag{5.11}$$

However the standard deviation $\sigma_F(t)$ on resonance consists of contributions from the inverted spins and from thermal noise:

$$\sigma_F = \sqrt{\sigma_{\text{F-spin}}^2 + \sigma_{\text{F-noise}}^2} \cong \sqrt{\sigma_{M_z}^2 G_{zx}^2 + \sigma_{\text{F-cant}}^2} \quad , \tag{5.12}$$

where $\sigma_{\text{F-spin}}$ is the standard deviation of the force originated in the spins and $\sigma_{\text{F-noise}}$ is the measurement force noise's standard deviation. In a thermally limited setup it is predominated by $\sigma_{\text{F-cant}}$, the standard deviation of the random thermal force acting on the cantilever ($\sigma_{\text{F-noise}} \cong \sigma_{\text{F-cant}}$). The latter is given by the fluctuation-dissipation theorem (section 3.1.7):

$$\sigma_{\text{F-cant}} = \sqrt{\frac{2k k_B T \Delta f_{\text{BW}}}{\pi f_{\text{L}_0} Q}} \quad , \tag{5.13}$$

where the measurement bandwidth $\Delta f_{\text{BW}} = 0.1$ Hz.

In general $F = \langle G_{zx} \rangle_V M_z$ and $\sigma_F = \sqrt{\langle G_{zx}^2 \rangle_V \sigma_{M_z}^2 + \sigma_{\text{F-cant}}^2}$, where $\langle \cdots \rangle_V$ denotes an average taken over the detection volume V. For detection volumes small enough that G_{zx} is slowly varying throughout, as in all experiments discussed here, $\langle G_{zx} \rangle_V^2 = \langle G_{zx}^2 \rangle_V$.

Off resonance, only thermal fluctuations drive the cantilever resulting in $F = 0$ and $\sigma_F = \sigma_{\text{F-cant}}$.

The above quantities correspond to variance of the lock-in amplifier's in-phase channel σ_{ip}^2 and the variance of its quadrature channel σ_{qd}^2 as following (sections 3.1.6,

3.7.3 and 4.1.4):

$$\sigma_{\text{F-spin}} = \left(\frac{k}{\alpha_t Q} \right) \sqrt{\sigma_{\text{ip}}^2 - \sigma_{\text{ip}}^2} \quad , \tag{5.14}$$

$$\sigma_{\text{F-noise}} = \left(\frac{k}{\alpha_t Q} \right) \sqrt{\sigma_{\text{qd}}^2} \quad , \tag{5.15}$$

where α_t is the transduction coefficient in units of V/m (section 3.1.7).

5.3.2 Results

From the described measurements the number of spins in the addressed ensemble is determined. The here presented method is much more precise than by the straight forward calculation mentioned in section 4.1.5, which involves the calculation of the intersection of the resonance slice section 4.1.2 with the sample wherefore the distribution of the $\vec{B}$-field has to be known. Further, the spin-lattice relaxation time T_1 of the nanoscale ensemble is determined.

NUMBER OF SPINS AND DETECTION VOLUME: Combining the equations (5.4) and (5.6) gives the expression for N depending, aside from the known measurement constants T, B_z and γ, only on the ratio of M_z and σ_{M_z}:

$$N = \frac{3}{I(I+1)} \left(\frac{k_B T}{\hbar \gamma B_z} \right)^2 \left(\frac{M_z}{\sigma_{M_z}} \right)^2 \quad . \tag{5.16}$$

In a material with a nuclear spin density na, where n is the number density of the nuclear element and a is the natural abundance of the measured isotope, the corresponding detection volume is then given by $V = \frac{N}{na}$.

From the ratio of the measured thermal and statistical polarisations and using eq. (5.16) with $M_z/\sigma_{M_z} = F/\sigma_{\text{F-spin}}$, the number of spins in the detected ensembles is determined. N ranges from 0.98×10^6 to 6.61×10^6 corresponding to detection volumes V from $(26.3 \text{ nm})^3$ to $(49.7 \text{ nm})^3$. As shown in fig. 5.5, pulses with the smallest $\Delta f_{\text{mod}} = 1$ MHz address a spin ensemble slightly smaller than $N_c = 1.10 \times 10^6$ spins, i.e. just small enough to be dominated by statistical nuclear spin polarisation. The calculated number of spins compare favourably to the lower limit of spins determined through estimates of the magnetic field gradient based on a magneto-static model in the manner of the supplementary section of Peddibhotla et al. [103].

SPIN-LATTICE RELAXATION TIME T_1:   The experiments also show that $T_1 = 7.2 \pm 1.0$ s and is independent of the ensemble size within the error of the measurement. This value is similar to previous measurements of larger detection volumes, yielding $T_1 = 6.2$ s [84]. Precise comparisons are difficult given that T_1 depends strongly on the density
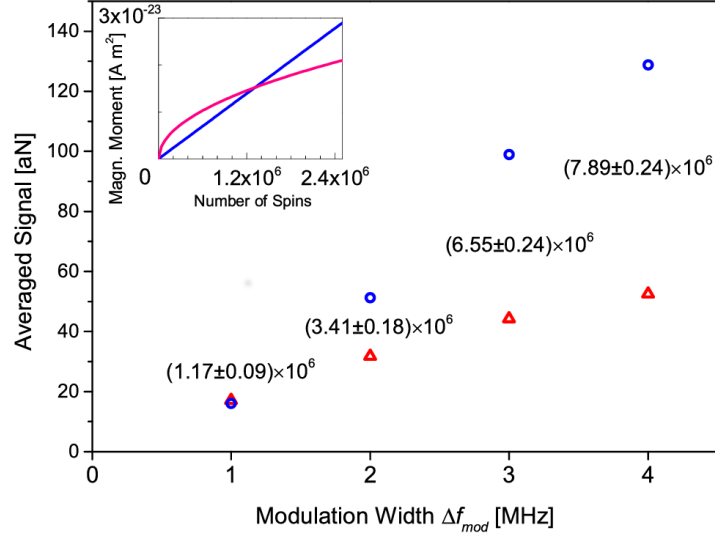
FIGURE 5.5: THERMAL VERSUS STATISTICAL POLARISATION
F (blue circles), originating from the thermal polarisation, and $\sigma_{\text{F-spin}}$ (red triangles), originating from the statistical polarisation, as a function of the ARP modulation width Δf_{mod} at $B = 4.37$ T and $T = 4.4$ K. The values between the symbols show the corresponding number of spins N given by equation (5.16). As expected from (5.4) and (5.6), F increases linearly with increasing detection volume or roughly linearly with Δf_{mod}, while $\sigma_{\text{F-spin}}$ increases roughly as $\sqrt{\Delta f_{\text{mod}}}$.
Inset: A theoretical plot of M_z and σ_{M_z} for ^{19}F as a function of N showing the crossover at $N_c = 1.10 \times 10^6$ spins. The similarity between the inset and the figure indicate that the number of detected spins or the detection volume V is roughly proportional to Δf_{mod}.

of paramagnetic impurities in the sample as well as oxygen at the surface. Recent measurements of small ensembles of electron spins also show that a small detection volume can alter the measured T_1 relative to conventional measurements. For tiny detection volumes within a larger sample, the measured T_1 can be reduced by spin diffusion effects relative to measurements of macroscopic detection volumes [164].

5.3.3 Discussion

NUMBER OF SPINS AND DETECTION VOLUME: For detection volumes in which G_{zx} is nearly constant, the error in the determination of the size of the detected ensemble depends only on the error of the measurements of F and σ_F and on the error in determining B_z and T. This method therefore provides a complementary and, in some cases, more precise alternative to other techniques.

In particular, in MRFM the size of the detected ensemble is usually determined by measuring either F or σ_F (depending on whether the volume is in the thermal or

statistical regime), estimating the magnetic field gradient, and then calculating the number of moments responsible for the measured force. The precision of this scheme depends on knowledge of, additionally to B_z and T, the magnetic field gradient G_{zx} at the sample and the spring constant k of the cantilever. Often, such quantities are measured with a high degree of error.

An estimate of the size of the detection volume can also be made through knowledge of the magnetic field profile of the tip, calculation of the resonant slice geometry, and knowledge of the shape and position of the sample. Again, such calculations are typically imprecise.

In fact, our method can be applied to any NMR technique capable of detecting both the thermal and statistical polarisations. These include conventional RF probes at room temperature [165, 166] and optical Faraday rotation methods in alkali metal vapours [167]. In all cases the comparison of statistical and thermal magnetisation may provide additional information, especially when either the precise shape or density distribution of the sample is unknown.

SPIN-LATTICE RELAXATION TIME T_1:   Classical MRFM does not exhibit the ability to measure T_1 in nanoscale samples. By the presented method this is possible only through changing the measurement sequence and some different wiring (section 3.7.4), but without changing anything in the existing measurement setup.

CONCLUSION: In the presented experiment, NMR measurements of small ensembles of ^{19}F nuclei showing the transition from a thermally dominated to statistically dominated ensemble magnetisation are performed. In addition, a method for determining the number of spins in nanometre-scale ensembles by measuring and comparing both the thermal and statistical polarisations is demonstrated.

These results are relevant to a number of recent experiments, which can now address nanometre-scale ensembles of nuclear spins. Until today, statistical polarisation in conventional NMR and MRI of macroscopic samples has played a limited role [154]. The fact that even for a fairly large ensemble of 10^6 ^{19}F nuclear spins at low temperature and high field natural polarisation fluctuations overtake the thermal polarisation underscores just how weak conventional NMR signals are. As methods for nano-MRI continue to develop, the role of statistical polarisation, as highlighted here, will become increasingly important.

6 Magnetic Vortex as Gradient Source

> *Wer mich korrekterweise kritisiert, ist mein Lehrer. Wer mir fälschlich schmeichelt, ist mein Feind.*
>
> Sunzi, *Die Kunst des Krieges*, ~ 500 v. Chr.

6.1 Idea

Permalloy disks can produce magnetic vortices (MV) with high field gradients $\vec{G}$ above a flat surface. In contrast, the highest gradients of MRFM's solid-state magnets are found closest to their edges.

The used nano-magnets for the experiments described in this work are (intentionally) extremely uneven, relative to their surrounding (section 3.5). Thereby, they produce not only filed gradients of $> 10^6$ T/m but they also cause limiting troubles in frequency stability (section 4.2.5) and enhance non-contact friction exactly because they are uneven. The application of MV as gradient source for MRFM would significantly reduce these problems.

MV are curling magnetisation structures formed in micro- and nano-sized magnetic disks and polygons. They are known for having four distinct magnetisation configurations defined by the combination of the polarity (up or down) and circulation direction. Vortex states can be controlled by applying a static out-of-plane (polarity control) [168] or in-plane (circulation control) [169] magnetic field, although the amplitude of these fields can be quite large. However, both the polarity and the circulation can be switched more effectively by using fast-rising magnetic fields [170].

In collaboration with Jesse Berezovsky, case western reserve university, Cleveland, we came up with the simplified idea to use a static state of such a vortex [171] as source for $\vec{G}$. Therefore the nano-magnet on top of the micro-wire (section 3.4) is swapped with a permalloy disc and the entire measurement apparatus (chapter 3) as well as the MRFM protocol (chapter 4) needs only minor adjustments. Already anticipating a part of the conclusion, the switching dynamics[170, 172, 173] have been underestimated.

6.2 Effort Made

SIMULATIONS: Robert Badea, PhD student in Berezovsky's group, made simulations of the magnetic field strength 50 nm above Permalloy disks for different out-of-plane static magnetic fields B_0 (in z-direction). As shown in fig. 6.1 at $B_0 = 100$ mT the simulations showed a gradient $\partial B_z/\partial x = G_{zx} \sim 4 \cdot 10^5$ T/m.
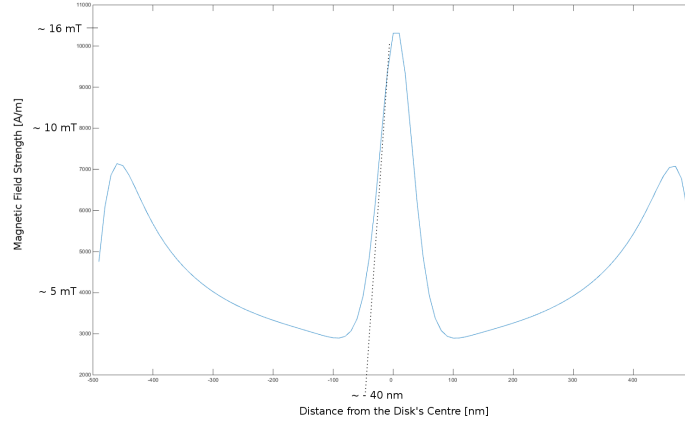

FIGURE 6.1: SIMULATION OF THE MAGNETIC FIELD STRENGTH
Line cuts of the magnetic field strength 50 nm above a 1 µm wide Permalloy disk with an applied static field $\vec{B}_0 = 100$ mT. The peak in the middle is the vortex's field with a gradient of roughly $4 \cdot 10^5$ T/m. As for the standard nano-magnet, also the edges exhibit significant G_{zx}, which gets bigger with higher $\vec{B}_0$. For $B_{\text{tot}} = B_0 + B_{\text{vortex}} = 116$ mT resonance frequencies of 6.81 MHz for ^{1}H, respectively 2.00 MHz for ^{19}F are expected. The simulations are made by Robert Badea.

VORTEX MICRO-WIRE: The existing micro-wires are too narrow for the permalloy disks. Therefore new, wider ones are made, with an integrated additional gate in order to vary the electric field around the cantilever with an applied voltage. The design follows the standard micro-wires with large pads for the in-bonding and a narrow constriction, here between 2 to 4 µm wide and 8 µm long. Based on the design, a custom made photolithography chromium mask for negative photoresist was ordered. The 200 nm high Au micro-wires are made by optical lithography and electron-beam evaporation according to the manual in appendix A.4.

On top of each wire Badea deposited 3 Permalloy ($Ni_{0.81}$ $Fe_{0.19}$) disks with a diameter of ~ 1 µm and a height of ~ 40 nm. Some disks are capped with a 5 nm thick alumina layer reducing degradation due to oxidation; The advantage of the disks without capping is that the sample can be brought closer to the magnetic material and thereby into higher G_{zx}. Badea successfully tested the disks for MV by magneto-optical Kerr effect (MOKE) microscopy [171] .
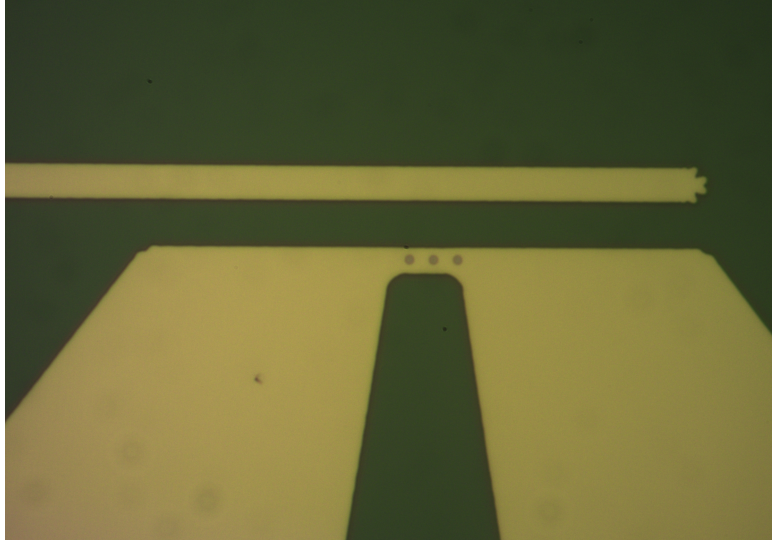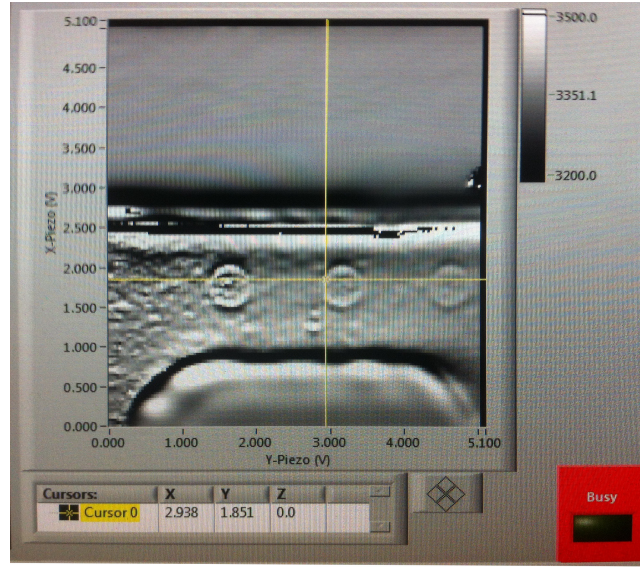
FIGURE 6.2: VORTEX MICRO-WIRE
Three Permalloy disks (grey) with a diameter of 1 μm and a height of ~ 40 nm on a ~ 3 μm wide micro-wire (golden). The horizontal stripe at the top is an additional (third) gate in order to minimise non-contact friction and counteract changes in f_{L_0} via V_{bias} (section 3.1.5).

EXPERIMENT INITIALISATION: MRFM measurements with uncoated types of MV disks are initiated following the description in section 4.3.1, whereby the KPF$_6$ test-sample was positioned in the middle of a disc. Figure 6.3 shows a 2D frequency-scan picture of the micro-wires constriction with the MV disks. Magnetic resonance frequency sweeps at $B_0 = 0.1$ T, $B_z = 116$ mT, and $f_{\text{centre}} = \{6.81, 2.00\}$ MHz for ^{1}H, respectively ^{19}F, together with ARP pulse parameter optimisation and spatial scans are preformed as described in section 4.3.2 in order to find a MRFM signal.

On all three disks, neither in the middle nor at the edges, a NMR response could be detected even after extensive, semi-automated frequency and spatial scans.

Reasons for failing are not definitely determined. Possible reasons are: a too low G_{zx}, a too small resonant volume (intersection of the sample with the region where the B_1 field is on resonance with the spins), and last but not least disturbing MV dynamics due to the ARP pulses. The pulse frequencies and strengths to dynamically switch the spin circulation and vortex polarity are not investigated for these particular MV discs. Our (including Berezovsky) presumption is that the MV are too inert to follow the applied B_1.

FIGURE 6.3: 2D FREQUENCY SCAN PICTURE OF THE VORTEX MICRO-WIRE
Image of the LabView controls of a 2D frequency scan. The levels of grey reflect the
cantilever's frequency f_{L_0}. The micro-wire is 3 μm wide, the disks measure 1 μm in
diameter and ~ 40 nm in height. Unfortunately, for none of the three Permalloy disks a
MRFM signal could be measured. The possible reasons are mentioned in the text.

6.3 How Could it Work?

If the successful implementation of MV gradients in MRFM wants to be enforced with
more effort, I would propose to determine magnetic field distribution and dynamics with
e.g. magnetic force or MOKE microscopy, accompanied by theoretical studies of the
MV behaviour at the MRFM resonance frequencies und pulse strengths.

Although, on the base of my knowledge, this particular MV disks are not ideally
suited to improve MRFM. Advantages of frequency stability and lower non-contact
friction do not overweight the lower gradient and experimental troubles.

7 Outlook

> *Caminante, no hay camino, – se hace camino al andar.*
> *Wanderer, es gibt keinen Weg, – der Weg entsteht beim Gehen.*

Antonio Machado, *Proverbios y cantares XXIX*, 1912

The first part of this thesis' outlook focuses on the upcoming possible improvements of the present MRFM setup. The direct improvements listed in the following have already been discussed in their specific sections in the chapters 1, 3, 4 and 6. In the second part, a glance on the applications of sensitivity improved MRFM is taken. Both parts depend to a major part on the co-authored book section *Force-Detected Nuclear Resonance* [1].

7.1 Improvements of MRFM Itself

SUMMARY: Since the imaging experiments of 2009 [99], no improvement of the MRFM's imaging resolution has been demonstrated, although progress has been made on the force sensitivity's key components: cantilevers, gradient sources, and detection protocols. Combining these recent improvements into a single apparatus should lead to a resolution of ~ 1 nm over a range of ~ 100 nm. Further development in the topics of nanowires as force transducers and switchable gradient sources, enabling the access to a vast repository of NMR puls sequences, may yield an even higher improvement.

FLAT GRADIENT SOURCES reduce non-contact friction and improve the frequency stability in comparison to nano-magnet pillars. Thereby less effort on the frequency stabilisation will be needed allowing faster measurement repetition with longer averaging times and by the lower dissipation the minimal measurable force is decreased.

The usage of a commercial hard disk drive (HDD) write head exhibiting an extremely flat surface and yielding a magnetic gradient of up to $28 \cdot 10^6$ T/m has been demonstrated [57]. Moreover, such a HDD write head can be switched on and off, hence the remarks on switchable magnetic field gradients further below apply as well.

The permalloy magnets with a vortex state discussed in chapter 6 can also serve as flat gradient sources. Although it is questionable if thereby as high as today or even higher gradients can be achieved.

NANOWIRES are promising candidates for more sensitive force transducers due to their dimensions and bottom-up instead of top-down fabrication (section 1.4.3). As introduced in the beginning (section 1.3.2) and later on carried out in detail, the *force sensitivity*, i.e. the inverse of the *minimal measurable force* $F_{\min}$ (eq. (3.56)), is characterised by the spectral density S_F. S_F is proportional to the intrinsic dissipation $\Gamma_0 = {}^k/{\omega_{L_0} Q}$ (eq. (3.53)), with $k = m\omega_{L_0}^2$. Since $m \propto wdl$ (the force sensor's dimensions), $\omega_{L_0} \propto {}^d/{l^2}$, and in the given surface loss dominated regime (section 3.1.5) $Q \propto d$, we get $\Gamma_0 \propto {}^{wd}/{l}$. Shrinking the dimensions can be expressed by a multiplication of w, d and l with a factor $\xi < 1$. It is now obvious why the sensitivity of smaller force sensors is higher i.e. why a better force sensor is smaller:

$$\text{FORCE SENSITIVITY} \propto \frac{1}{\sqrt{S_F}} \propto \frac{1}{\sqrt{\Gamma_0}} \propto \frac{1}{\sqrt{\xi}} \quad . \tag{7.1}$$

The difficulties with nanowires are combinations of several issues: they have to be at the edge of the carrier chip, because of the interferometric detection; they should not be removed from the substrate they were grown onto, to keep clamping losses minimal; and the attachment of quasi-arbitrary samples to a specific NW is even more difficult than with cantilevers. Also a faster procedure of NW identification and interferometer alignment would make the their usage easier as force transducers.

SAMPLE ATTACHMENT to cantilevers still is a demanding task. The entire process of preparing the sample, glueing it to the cantilever and coating it in order to reduce non-contact friction so far yields only a mendable success rate.

Faster and more successful attachment procedures would reduce delays in the experiments due to such problems, and, in regard of sample attachment to NW, this issue becomes much more difficult and important.

SWITCHABLE MAGNETIC FIELD GRADIENTS open the door to various, well established NMR pulse sequences. Already a switchable gradient in one spacial direction like the 240 nm narrow constriction in a "micro-wire" or the mentioned HDD write head enables Fourier-transform MRI [56]. The extension to two orthogonally orientated switchable gradients offers much more possibilities and lies within reach [74]. The proof of concept of Budakian's group [56, 77, 88] represents a paradigm shift in MRFM and exhibits a big potential for future development.

MAGNET ON CANTILEVER configuration points in the promising direction of applied MRFM. The preparation of a high gradient magnetic tip on the end of delicate cantilever is probably more demanding than producing nano-magnets on a micro-wire [60, 61, 146]. Though in this configuration serial measurements of different sample would be straight-forwardly possible. Integrating the samples together with the RF field source on

the same chip specifically for this task has to be further developed, but initial attempts have already been made [61].

A MRFM setup where only the multi-sample chip, but not the cantilever, has to be exchanged, would make measurements of different samples extremely faster. One could call it: Fast Versatile MRFM.

7.2 Applied MRFM

GENERALLY: MRI's ability to produce truly three dimensional, non-destructive, spectroscopic "images" is unique. None of today's measurement methods like optical photography, microscopy, radiography, x-ray spectroscopy, SEM, AFM, STM, . . ., are able to produce anything likewise. Also computed tomography (CT) images are only made by calculations based on radiography images and they eventually suffer, at least a bit, under the absorption by the material ahead and behind the image point.

In order to apply MRFM to a wide range of interesting nanoscale samples, the technically involved MRFM apparatuses have to be simplified to a great extent in hardware, sample preparation and measurement protocols. Further either the resolution (~ 10 nm) and/or the imaging range (~ 100 nm) have to be improved by at least one to two orders of magnitude so that the application of MRFM becomes more interesting for biological samples. Thereby, in the first case viruses and macro-molecules could be resolved, and in the second case, entire cells and bacterias could be imaged with today's or improved resolution. Protocols for the preparation of biological samples for the high-vacuum and cryogenic environment exist e.g. from cryo-electron microscopy [174] and could be adapted to MRFM. The impact of spatially resolving proteins would be quantum leap in biology!

Along with nano-biology samples, also other sample prospects are longing until MRFM enables to better explore the "unbridged imaging regime" between $\lesssim 1$ nm and 100 nm [18], or that (spectroscopic) images of several microns big objects can be made with at least sub-μm or even nm spatial resolution.

Most semiconductors contain non-zero nuclear magnetic moments. Therefore, MRFM may prove useful for sub-surface imaging of nanoscale electronic devices. MRFM also appears to be the only technique capable of directly measuring the dynamics of the small ensembles of nuclear spins that limit electron spin coherence in single semiconductor quantum dots. Polymer films and self-assembled monolayers – important for future molecular electronics – are another exciting target for MRFM and its capability to image chemical composition on the nanoscale. Finally, isotopically engineered materials are becoming increasingly important for tuning a variety of physical properties such as transport and spin. Researchers currently lack a general method for non-invasively imaging the isotopic composition of these materials [175–177]; MRFM techniques could fill this void [1].

RELAXATION TIMES IN 1-D NANOWIRES   are such a possible research subject. Low-dimensional condensed matter systems with strong spin-orbit interaction (SOI) have attracted much theoretical and experimental attention for their realisation of nontrivial momentum space topology [178].

Examples of such systems are semiconducting nanowires e.g. InGaAs or Mn-doped GaAs wires, which form a one-dimensional system. The theorist's theories[1] say, that due to RKKY interaction and/or Rashba SOI localised spins can order into a helical state. In case of RKKY interaction: if the polarisation of current-carrying electrons and localised spins differ, spin-transfer torque arises which is important for dynamics of domain walls [179]. Insulating and superconducting states of helical Rashba wires can host Jackiw-Rebbi and Majorana bound states around topological defects [178]. These effects influence the spin-lattice relaxation time T_1 and might be observed and investigated already with the present MRFM system [179]. The magnet-on-cantilever configuration would be even better suited.

---

[1]I mean no offence, on the contrary. To say I have properly understood their work would be a bald lie.

Bibliography

[1] M. Poggio and B. E. Herzog. "Force-Detected Nuclear Magnetic Resonance". In: *Micro and Nano Scale NMR: Technologies and Systems*. Ed. by Jens Anders and Jan G. Korvink. Weinheim: Wiley-VCH, 2017, p. 31 (cit. on pp. 2, 5, 99, 101).

[2] F. Bloch. "Nuclear Induction". In: *Phys. Rev.* 70.7-8 (1946), pp. 460–474 (cit. on pp. 3, 79, 81).

[3] Tycho Sleator, Erwin L. Hahn, Claude Hilbert, and John Clarke. "Nuclear-Spin Noise". In: *Phys. Rev. Lett.* 55.17 (1985), pp. 1742–1745 (cit. on pp. 3, 7, 65).

[4] C. J Hardy, W. A Edelstein, and D Vatis. "Efficient Adiabatic Fast Passage for NMR Population Inversion in the Presence of Radiofrequency Field Inhomogeneity and Frequency Offsets". In: *Journal of Magnetic Resonance (1969)* 66.3 (1986), pp. 470–482 (cit. on p. 4).

[5] Charles P. Slichter. *Principles of Magnetic Resonance*. 3rd enlarged and updated ed. 1990. Corr. 3rd printing 1996 edition. Berlin ; New York: Springer, 1996. 658 pp. (cit. on pp. 4, 15–17, 70, 82, 83).

[6] Malcolm H. Levitt and Ray Freeman. "NMR Population Inversion Using a Composite Pulse". In: *Journal of Magnetic Resonance (1969)* 33.2 (1979), pp. 473–476 (cit. on p. 4).

[7] J. A. Sidles. "Noninductive Detection of Single-Proton Magnetic Resonance". In: *Appl. Phys. Lett.* 58.24 (1991), pp. 2854–2856 (cit. on pp. 4, 7).

[8] Martino Poggio and Christian L. Degen. "Force-Detected Nuclear Magnetic Resonance: Recent Advances and Future Challenges". In: *Nanotechnology* 21.34 (2010). 00041, p. 342001 (cit. on pp. 5, 7).

[9] Prof Martino Poggio and Prof Christian L. Degen. "Magnetic Resonance Force Microscopy". In: *Encyclopedia of Nanotechnology*. Ed. by Professor Bharat Bhushan. Springer Netherlands, 2012, pp. 1256–1264 (cit. on p. 5).

[10] Seppe Kuehn, Steven A. Hickman, and John A. Marohn. "Advances in Mechanical Detection of Magnetic Resonance". In: *J Chem Phys* 128.5 (2008), p. 052208 (cit. on p. 5).

[11] Mladen Barbic. "Magnetic Resonance Force Microscopy". In: *Magnetic Resonance Microscopy*. Ed. by Sarah L. Codd and Joseph D. Seymour. Wiley-VCH Verlag GmbH & Co. KGaA, 2008, pp. 49–63 (cit. on p. 5).

[12] P. Chris Hammel and Denis V. Pelekhov. "The Magnetic Resonance Force Microscope". In: *Handbook of Magnetism and Advanced Magnetic Materials*. John Wiley & Sons, Ltd, 2007 (cit. on p. 5).

[13] Gennady P Berman, Fausto Borgonovi, Vyacheslav N Gorshkov, and Vladimir I Tsifrinovich. *Magnetic Resonance Force Microscopy and a Single-Spin Measurement*. WORLD SCIENTIFIC, 2006 (cit. on p. 5).

[14] A. Suter. "The Magnetic Resonance Force Microscope". In: *Progress in Nuclear Magnetic Resonance Spectroscopy* 45.3–4 (2004), pp. 239–274 (cit. on p. 5).

[15] N. Nestle, A. Schaff, and W. S. Veeman. "Mechanically Detected NMR, an Evaluation of the Applicability for Chemical Investigations". In: *Progress in Nuclear Magnetic Resonance Spectroscopy* 38.1 (2001), pp. 1–35 (cit. on p. 5).

[16] J. A. Sidles et al. "Magnetic Resonance Force Microscopy". In: *Rev. Mod. Phys.* 67.1 (1995). 00413, pp. 249–265 (cit. on pp. 5, 49).

[17] John A. Sidles and Daniel Rugar. "Signal-to-Noise Ratios in Inductive and Mechanical Detection of Magnetic Resonance". In: *Phys. Rev. Lett.* 70.22 (1993), pp. 3506–3509 (cit. on p. 5).

[18] Bradley Adam James Moores. "Spanning the Unbridged Imaging Regime: Advances in Mechanically Detected MRI". In: (2015) (cit. on pp. 6, 15, 45, 54, 69, 77, 101).

[19] D. F. Evans. "Direct Observation of Static Nuclear Susceptibilities at Room Temperature". In: *Philos. Mag.* 1.4 (1956), pp. 370–373 (cit. on p. 7).

[20] G. Alzetta, E. Arimondo, C. Ascoli, and A. Gozzini. "Paramagnetic Resonance Experiments at Low Fields with Angular-Momentum Detection". In: *Nuovo Cimento B (1965-1970)* 52.2 (1967), pp. 392–402 (cit. on p. 7).

[21] Tycho Sleator, Erwin L. Hahn, Claude Hilbert, and John Clarke. "Nuclear-Spin Noise and Spontaneous Emission". In: *Phys. Rev. B* 36.4 (1987), pp. 1969–1980 (cit. on pp. 7, 65).

[22] G. Binnig, H. Rohrer, Ch. Gerber, and E. Weibel. "Surface Studies by Scanning Tunneling Microscopy". In: *Phys. Rev. Lett.* 49.1 (1982), pp. 57–61 (cit. on p. 7).

[23] "United States Patent: 4724318 -Atomic Force Microscope and Method for Imaging Surfaces with Atomic Resolution". 4724318. Gerd K. Binnig. 1988 (cit. on p. 7).

[24] G. Binnig, C. F. Quate, and Ch. Gerber. "Atomic Force Microscope". In: *Phys. Rev. Lett.* 56.9 (1986), pp. 930–933 (cit. on p. 7).

[25] J. A. Sidles. "Folded Stern-Gerlach Experiment as a Means for Detecting Nuclear Magnetic Resonance in Individual Nuclei". In: *Phys. Rev. Lett.* 68.8 (1992), pp. 1124–1127 (cit. on p. 7).

[26] John A. Sidles, Joseph L. Garbini, and Gary P. Drobny. "The Theory of Oscillator-Coupled Magnetic Resonance with Potential Applications to Molecular Imaging". In: *Rev. Sci. Instrum.* 63.8 (1992), pp. 3881–3899 (cit. on p. 7).

[27] D. Rugar, C. S. Yannoni, and J. A. Sidles. "Mechanical Detection of Magnetic Resonance". In: *Nature* 360.6404 (1992), pp. 563–566 (cit. on pp. 7, 8, 49).

[28] D. Rugar et al. "Force Detection of Nuclear Magnetic Resonance". In: *Science* 264.5165 (1994), pp. 1560–1563 (cit. on p. 8).

[29] Z. Zhang, P. C. Hammel, and P. E. Wigen. "Observation of Ferromagnetic Resonance in a Microscopic Sample Using Magnetic Resonance Force Microscopy". In: *Appl. Phys. Lett.* 68.14 (1996), pp. 2005–2007 (cit. on p. 8).

[30] K. Wago, D. Botkin, C. S. Yannoni, and D. Rugar. "Paramagnetic and Ferromagnetic Resonance Imaging with a Tip-on-Cantilever Magnetic Resonance Force Microscope". In: *Appl. Phys. Lett.* 72.21 (1998), pp. 2757–2759 (cit. on pp. 8, 10, 49).

[31] H Jonathon Mamin, Raffi Budakian, Ben W. Chui, and Daniel Rugar. "Detection and Manipulation of Statistical Polarization in Small Spin Ensembles". In: *Phys Rev Lett* 91.20 (2003), p. 207604 (cit. on p. 8).

[32] D. Rugar, R. Budakian, H. J. Mamin, and B. W. Chui. "Single Spin Detection by Magnetic Resonance Force Microscopy". In: *Nature* 430.6997 (2004), pp. 329–332 (cit. on pp. 8, 10, 24).

[33] K. J. Bruland, J. Krzystek, J. L. Garbini, and J. A. Sidles. "Anharmonic Modulation for Noise Reduction in Magnetic Resonance Force Microscopy". In: *Review of Scientific Instruments* 66.4 (1995), pp. 2853–2856 (cit. on p. 8).

[34] John A. Marohn, Raúl Fainchtein, and Doran D. Smith. "Mechanical Modulation of Sample Magnetization in Magnetic Resonance Force Microscopy". In: *Journal of Applied Physics* 86.8 (1999), pp. 4619–4625 (cit. on p. 8).

[35] B. C. Stipe et al. "Electron Spin Relaxation Near a Micron-Size Ferromagnet". In: *Phys. Rev. Lett.* 87.27 (2001), p. 277602 (cit. on p. 8).

[36] Sean R. Garner, Seppe Kuehn, Jahan M. Dawlaty, Neil E. Jenkins, and John A. Marohn. "Force-Gradient Detected Nuclear Magnetic Resonance". In: *Appl. Phys. Lett.* 84.25 (2004), pp. 5091–5093 (cit. on p. 8).

[37] T. D. Stowe et al. "Attonewton Force Detection Using Ultrathin Silicon Cantilevers". In: *Appl. Phys. Lett.* 71.2 (1997), pp. 288–290 (cit. on p. 8).

[38] H. J. Mamin and D. Rugar. "Sub-Attonewton Force Detection at Millikelvin Temperatures". In: *Appl. Phys. Lett.* 79.20 (2001), pp. 3358–3360 (cit. on p. 8).

[39] B.W. Chui et al. "Mass-Loaded Cantilevers with Suppressed Higher-Order Modes for Magnetic Resonance Force Microscopy". In: *TRANSDUCERS, Solid-State Sensors, Actuators and Microsystems, 12th International Conference on, 2003*. TRANSDUCERS, Solid-State Sensors, Actuators and Microsystems, 12th International Conference on, 2003. Vol. 2. 00025. 2003, 1120–1123 vol.2 (cit. on pp. 8, 24, 25).

[40] Y. Tao et al. "Permanent Reduction of Dissipation in Nanomechanical Si Resonators by Chemical Surface Protection". In: *Nanotechnology* 26.46 (2015), p. 465501 (cit. on pp. 9, 24, 35).

[41] K.Y. Yasumura et al. "Quality Factors in Micron- and Submicron-Thick Cantilevers". In: *J. Microelectromechanical Syst.* 9.1 (2000), pp. 117–125 (cit. on pp. 9, 35).

[42] Jinling Yang, T. Ono, and M. Esashi. "Energy Dissipation in Submicrometer Thick Single-Crystal Silicon Cantilevers". In: *J. Microelectromechanical Syst.* 11.6 (2002), pp. 775–783 (cit. on pp. 9, 37).

[43] J. L. Garbini, K. J. Bruland, W. M. Dougherty, and J. A. Sidles. "Optimal Control of Force Microscope Cantilevers. I. Controller Design". In: *Journal of Applied Physics* 80.4 (1996), pp. 1951–1958 (cit. on p. 9).

[44] K. J. Bruland, J. L. Garbini, W. M. Dougherty, and J. A. Sidles. "Optimal Control of Force Microscope Cantilevers. II. Magnetic Coupling Implementation". In: *Journal of Applied Physics* 80.4 (1996), pp. 1959–1964 (cit. on p. 9).

[45] K. J. Bruland, J. L. Garbini, W. M. Dougherty, and J. A. Sidles. "Optimal Control of Ultrasoft Cantilevers for Force Microscopy". In: *Journal of Applied Physics* 83.8 (1998), pp. 3972–3977 (cit. on p. 9).

[46] C. L. Degen, U. Meier, Q. Lin, A. Hunkeler, and B. H. Meier. "Digital Feedback Controller for Force Microscope Cantilevers". In: *Review of Scientific Instruments* 77.4 (2006), p. 043707 (cit. on p. 9).

[47] Yu. Obukhov, K. C. Fong, D. Daughton, and P. C. Hammel. "Real Time Cantilever Signal Frequency Determination Using Digital Signal Processing". In: *Journal of Applied Physics* 101.3 (2007), p. 034315 (cit. on p. 9).

[48] K. Wago et al. "Magnetic Resonance Force Detection and Spectroscopy of Electron Spins in Phosphorus-Doped Silicon". In: *Review of Scientific Instruments* 68.4 (1998), pp. 1823–1826 (cit. on pp. 9, 10).

[49] Arnd Schaff and Wiebren S. Veeman. "Mechanically Detected Nuclear Magnetic Resonance at Room Temperature and Normal Pressure". In: *Journal of Magnetic Resonance* 126.2 (1997), pp. 200–206 (cit. on p. 9).

[50] K. Wago, D. Botkin, C. S. Yannoni, and D. Rugar. "Force-Detected Electron-Spin Resonance: Adiabatic Inversion, Nutation, and Spin Echo". In: *Phys. Rev. B* 57.2 (1998), pp. 1108–1114 (cit. on p. 9).

[51] Rieko Verhagen, Alexander Wittlin, Cees W. Hilbers, Herman van Kempen, and Arno P. M. Kentgens. "Spatially Resolved Spectroscopy and Structurally Encoded Imaging by Magnetic Resonance Force Microscopy of Quadrupolar Spin Systems". In: *J. Am. Chem. Soc.* 124.8 (2002), pp. 1588–1589 (cit. on p. 9).

[52] C. L. Degen et al. "Microscale Localized Spectroscopy with a Magnetic Resonance Force Microscope". In: *Phys. Rev. Lett.* 94.20 (2005), p. 207601 (cit. on p. 9).

[53] Qiong Lin et al. "Magnetic Double Resonance in Force Microscopy". In: *Phys. Rev. Lett.* 96.13 (2006), p. 137604 (cit. on p. 9).

[54] Kai W. Eberhardt, Qiong Lin, Urban Meier, Andreas Hunkeler, and Beat H. Meier. "Sensitive Magnetic Resonance Force Imaging of Low-$\ensuremath{\gamma}$ Nuclei". In: *Phys. Rev. B* 75.18 (2007), p. 184430 (cit. on p. 9).

[55] Kai W. Eberhardt, Christian L. Degen, Andreas Hunkeler, and Beat H. Meier. "One- and Two-Dimensional NMR Spectroscopy with a Magnetic-Resonance Force Microscope". In: *Angewandte Chemie International Edition* 47.46 (2008), pp. 8961–8963 (cit. on p. 9).

[56] John M. Nichol, Tyler R. Naibert, Eric R. Hemesath, Lincoln J. Lauhon, and Raffi Budakian. "Nanoscale Fourier-Transform Magnetic Resonance Imaging". In: *Phys. Rev. X* 3.3 (2013), p. 031016 (cit. on pp. 9, 14, 47, 71, 100).

[57] Y. Tao, A. Eichler, T. Holzherr, and C. L. Degen. "Ultrasensitive Mechanical Detection of Magnetic Moment Using a Commercial Disk Drive Write Head". In: *Nat. Commun.* 7 (2016), p. 12714 (cit. on pp. 9, 47, 99).

[58] K. J. Bruland et al. "Thermal Tuning of a Fiber-Optic Interferometer for Maximum Sensitivity". In: *Review of Scientific Instruments* 70.9 (1999), pp. 3542–3544 (cit. on pp. 10, 49).

[59] Jonilyn G. Longenecker, Eric W. Moore, and John A. Marohn. "Rapid Serial Prototyping of Magnet-Tipped Attonewton-Sensitivity Cantilevers by Focused Ion Beam Manipulation". In: *J. Vac. Sci. Technol. B* 29.3 (2011), p. 032001 (cit. on p. 10).

[60] Jonilyn G. Longenecker et al. "High-Gradient Nanomagnets on Cantilevers for Sensitive Detection of Nuclear Magnetic Resonance". In: *ACS Nano* 6.11 (2012), pp. 9637–9645 (cit. on pp. 10, 47, 100).

[61] Phani Kumar Peddibhotla. "Magnetic Resonance Force Microscopy : Harnessing Nuclear Spin Fluctuations". phd. University_of_Basel, 2013. 91 Bl. (Cit. on pp. 10, 15, 47, 49, 53, 59, 68, 69, 79, 100, 101).

[62]   O. Züger and D. Rugar. "First Images from a Magnetic Resonance Force Microscope". In: *Appl. Phys. Lett.* 63.18 (1993), pp. 2496–2498 (cit. on pp. 10, 78).

[63]   O. Züger and D. Rugar. "Magnetic Resonance Detection and Imaging Using Force Microscope Techniques (Invited)". In: *J. Appl. Phys.* 75.10 (1994), pp. 6211–6216 (cit. on p. 10).

[64]   O. Züger, S. T. Hoen, C. S. Yannoni, and D. Rugar. "Three-Dimensional Imaging with a Nuclear Magnetic Resonance Force Microscope". In: *J. Appl. Phys.* 79.4 (1996), pp. 1881–1884 (cit. on pp. 10, 78).

[65]   Aharon Blank, Curt R. Dunnam, Peter P. Borbat, and Jack H. Freed. "High Resolution Electron Spin Resonance Microscopy". In: *Journal of Magnetic Resonance* 165.1 (2003), pp. 116–127 (cit. on p. 10).

[66]   Kent R Thurber, Lee E Harrell, and Doran D Smith. "170 Nm Nuclear Magnetic Resonance Imaging Using Magnetic Resonance Force Microscopy". In: *Journal of Magnetic Resonance* 162.2 (2003), pp. 336–340 (cit. on p. 10).

[67]   S Tsuji, T Masumizu, and Y Yoshinari. "Magnetic Resonance Imaging of Isolated Single Liposome by Magnetic Resonance Force Microscopy". In: *Journal of Magnetic Resonance* 167.2 (2004), pp. 211–220 (cit. on p. 10).

[68]   H. J. Mamin, M. Poggio, C. L. Degen, and D. Rugar. "Nuclear Magnetic Resonance Imaging with 90-Nm Resolution". In: *Nat Nano* 2.5 (2007), pp. 301–306 (cit. on pp. 10, 24, 78).

[69]   Y. Tao, J. M. Boss, B. A. Moores, and Christian L. Degen. "Single-Crystal Diamond Nanomechanical Resonators with Quality Factors Exceeding One Million". In: *Nat Commun* 5 (2014) (cit. on pp. 11, 35).

[70]   Igor Aharonovich, Andrew D. Greentree, and Steven Prawer. "Diamond Photonics". In: *Nat Photon* 5.7 (2011), pp. 397–405 (cit. on p. 11).

[71]   F. Jelezko and J. Wrachtrup. "Single Defect Centres in Diamond: A Review". In: *phys. stat. sol. (a)* 203.13 (2006), pp. 3207–3225 (cit. on p. 11).

[72]   Christian Degen. "Nanoscale Magnetometry: Microscopy with Single Spins". In: *Nat Nano* 3.11 (2008), pp. 643–644 (cit. on p. 11).

[73]   D. D. D. Ma, C. S. Lee, F. C. K. Au, S. Y. Tong, and S. T. Lee. "Small-Diameter Silicon Nanowire Surfaces". In: *Science* 299.5614 (2003), pp. 1874–1877 (cit. on p. 11).

[74]   John Nichol. "Nanoscale Magnetic Resonance Imaging Using Silicon Nanowire Oscillators". 00000. Dissertation. University of Illinois at Urbana-Champaign, 2014 (cit. on pp. 11, 35, 47, 100).

[75] F. R. Braakman et al. "Nonlinear Motion and Mechanical Mixing in As-Grown GaAs Nanowires". In: *Appl. Phys. Lett.* 105.17 (2014), p. 173111 (cit. on pp. 11, 12, 35, 49).

[76] D. Rugar, H. J. Mamin, and P. Guethner. "Improved Fiber-Optic Interferometer for Atomic Force Microscopy". In: *Appl. Phys. Lett.* 55.25 (1989), pp. 2588–2590 (cit. on pp. 12, 49).

[77] John M. Nichol, Eric R. Hemesath, Lincoln J. Lauhon, and Raffi Budakian. "Displacement Detection of Silicon Nanowires by Polarization-Enhanced Fiber-Optic Interferometry". In: *Appl. Phys. Lett.* 93.19 (2008), p. 193110 (cit. on pp. 12, 100).

[78] A. Krishnan, E. Dujardin, T. W. Ebbesen, P. N. Yianilos, and M. M. J. Treacy. "Young's Modulus of Single-Walled Nanotubes". In: *Phys. Rev. B* 58.20 (1998), pp. 14013–14019 (cit. on p. 12).

[79] Joel Moser et al. "Ultrasensitive Force Detection with a Nanotube Mechanical Resonator". In: *Nat Nano* 8.7 (2013), pp. 493–496 (cit. on p. 12).

[80] S. Stapfner et al. "Cavity-Enhanced Optical Detection of Carbon Nanotube Brownian Motion". In: *Appl. Phys. Lett.* 102.15 (2013), p. 151910 (cit. on p. 13).

[81] Anil Kumar, Dieter Welti, and Richard R. Ernst. "NMR Fourier Zeugmatography". In: *J. Magn. Reson. 1969* 18.1 (1975), pp. 69–83 (cit. on p. 13).

[82] D. I. Hoult. "Rotating Frame Zeugmatography". In: *J. Magn. Reson. 1969* 33.1 (1979), pp. 183–197 (cit. on p. 13).

[83] Lizann Bolinger and John S. Leigh. "Hadamard Spectroscopic Imaging (HSI) for Multivolume Localization". In: *J. Magn. Reson. 1969* 80.1 (1988), pp. 162–167 (cit. on p. 13).

[84] Kai W. Eberhardt, Christian L. Degen, and Beat H. Meier. "Fast Magnetic Resonance Force Microscopy with Hadamard Encoding". In: *Phys. Rev. B* 76.18 (2007), p. 180405 (cit. on pp. 13, 91).

[85] Kai W. Eberhardt. "Advances in Magnetic Resonance Force Microscopy". Dissertation. Eidgenössische Technische Hochschule ETH Zürich, Nr. 17562, 2008, 2008 (cit. on p. 13).

[86] Kai W. Eberhardt et al. "Two-Dimensional Magnetic Resonance Force Microscopy Using Full-Volume Fourier and Hadamard Encoding". In: *Phys. Rev. B* 78.21 (2008), p. 214401 (cit. on p. 13).

[87] Rosmarie Joss, Ivan T. Tomka, Kai W. Eberhardt, Jacco D. van Beek, and Beat H. Meier. "Chemical-Shift Imaging in Micro- and Nano-MRI". In: *Phys. Rev. B* 84.10 (2011), p. 104435 (cit. on p. 13).

[88] John M. Nichol, Eric R. Hemesath, Lincoln J. Lauhon, and Raffi Budakian. "Nanomechanical Detection of Nuclear Magnetic Resonance Using a Silicon Nanowire Oscillator". In: *Phys. Rev. B* 85.5 (2012), p. 054414 (cit. on pp. 13, 100).

[89] N. David Mermin. "What's Wrong with This Pillow?" In: *Phys. Today* 42.4 (1989), pp. 9–11 (cit. on p. 15).

[90] H. J. Mamin et al. "Isotope-Selective Detection and Imaging of Organic Nanolayers". In: *Nano Lett.* 9.8 (2009), pp. 3020–3024 (cit. on pp. 15, 78).

[91] J. J. Sakurai. *Modern Quantum Mechanics*. Revised edition. Reading, Mass: Addison Wesley, 1993. 500 pp. (cit. on p. 16).

[92] E. Van Veenendal, B. H. Meier, and A. P. M. Ketgens. "Frequency Stepped Adiabatic Passage Excitation of Half-Integer Quadrupolar Spin Systems". In: *Mol. Phys.* 93.2 (1998), pp. 195–213 (cit. on p. 17).

[93] W. F. Reynolds. "NMR Pulse Sequences". In: *Encyclopedia of Spectroscopy and Spectrometry (Third Edition)*. Ed. by John C. Lindon, George E. Tranter, and David W. Koppenaal. Oxford: Academic Press, 2017, pp. 195–208 (cit. on p. 17).

[94] E. M. Purcell, H. C. Torrey, and R. V. Pound. "Resonance Absorption by Nuclear Magnetic Moments in a Solid". In: *Phys. Rev.* 69.1-2 (1946), pp. 37–38 (cit. on p. 18).

[95] F. Bloch, W. W. Hansen, and Martin Packard. "Nuclear Induction". In: *Phys. Rev.* 69.3-4 (1946), p. 127 (cit. on p. 18).

[96] Michael Garwood and Lance DelaBarre. "The Return of the Frequency Sweep: Designing Adiabatic Pulses for Contemporary NMR". In: *Journal of Magnetic Resonance* 153.2 (2001), pp. 155–177 (cit. on pp. 18–22, 63).

[97] C. L. Degen, M. Poggio, H. J. Mamin, and D. Rugar. "Role of Spin Noise in the Detection of Nanoscale Ensembles of Nuclear Spins". In: *Phys. Rev. Lett.* 99.25 (2007), p. 250601 (cit. on pp. 24, 70, 71, 81, 84).

[98] M. Poggio, H. J. Mamin, C. L. Degen, M. H. Sherwood, and D. Rugar. "Nuclear Double Resonance between Statistical Spin Polarizations". In: *Phys. Rev. Lett.* 102.8 (2009). WOS:000263816200068, p. 087604 (cit. on pp. 24, 80, 84).

[99] C. L. Degen, M. Poggio, H. J. Mamin, C. T. Rettner, and D. Rugar. "Nanoscale Magnetic Resonance Imaging". In: *PNAS* 106.5 (2009), pp. 1313–1317 (cit. on pp. 24, 49, 64, 78, 99).

[100] T. H. Oosterkamp, M. Poggio, C. L. Degen, H. J. Mamin, and D. Rugar. "Frequency Domain Multiplexing of Force Signals with Application to Magnetic Resonance Force Microscopy". In: *Appl. Phys. Lett.* 96.8 (2010). WOS:000275027200073, p. 083107 (cit. on pp. 24, 84).

[101] Fei Xue, P. Peddibhotla, Michele Montinaro, D. P. Weber, and Martino Poggio. "A Geometry for Optimizing Nanoscale Magnetic Resonance Force Microscopy". In: *Appl. Phys. Lett.* 98.16 (2011), p. 163103 (cit. on pp. 24, 47, 49, 55).

[102] Fei Xue, D. P. Weber, P. Peddibhotla, and M. Poggio. "Measurement of Statistical Nuclear Spin Polarization in a Nanoscale GaAs Sample". In: *Phys. Rev. B* 84.20 (2011), p. 205328 (cit. on pp. 24, 49, 82–84).

[103] P. Peddibhotla et al. "Harnessing Nuclear Spin Polarization Fluctuations in a Semiconductor Nanowire". In: *Nat Phys* 9.10 (2013), pp. 631–635 (cit. on pp. 24, 45, 49, 59, 79, 81, 91).

[104] B. E. Herzog, D. Cadeddu, F. Xue, P. Peddibhotla, and M. Poggio. "Boundary between the Thermal and Statistical Polarization Regimes in a Nuclear Spin Ensemble". In: *Appl. Phys. Lett.* 105.4 (2014), p. 043112 (cit. on pp. 24, 25, 49, 59, 67, 79, 81).

[105] M. Poggio, C. L. Degen, H. J. Mamin, and D. Rugar. "Feedback Cooling of a Cantilever's Fundamental Mode below 5 mK". In: *Phys. Rev. Lett.* 99.1 (2007), p. 017201 (cit. on pp. 24, 25, 49, 68, 86).

[106] D. P. Weber et al. "Cantilever Magnetometry of Individual Ni Nanotubes". In: *Nano Lett.* 12.12 (2012). 00005, pp. 6139–6144 (cit. on pp. 24, 49, 55).

[107] M. Montinaro et al. "Feedback Cooling of Cantilever Motion Using a Quantum Point Contact Transducer". In: *Appl. Phys. Lett.* 101.13 (2012). WOS:000309426800069, p. 133104 (cit. on pp. 24, 49).

[108] A. Buchter et al. "Reversal Mechanism of an Individual Ni Nanotube Simultaneously Studied by Torque and SQUID Magnetometry". In: *Phys. Rev. Lett.* 111.6 (2013). 00002, p. 067202 (cit. on pp. 24, 49, 55).

[109] J. Nagel et al. "Nanoscale Multifunctional Sensor Formed by a Ni Nanotube and a Scanning Nb nanoSQUID". In: *Phys. Rev. B* 88.6 (2013), p. 064425 (cit. on pp. 24, 55).

[110] A. Mehlin et al. "Stabilized Skyrmion Phase Detected in MnSi Nanowires by Dynamic Cantilever Magnetometry". In: *Nano Lett.* 15.7 (2015), pp. 4839–4844 (cit. on pp. 24, 49, 55).

[111] Sean M. Han, Haym Benaroya, and Timothy Wei. "Dynamics of Transversely Vibrating Beams Using Four Engineering Theories". In: *Journal of Sound and Vibration* 225.5 (1999), pp. 935–988 (cit. on pp. 25, 27).

[112] Andrew N Cleland. *Foundations of Nanomechanics From Solid-State Theory to Device Applications*. Berlin, Heidelberg: Springer Berlin Heidelberg, 2003 (cit. on pp. 25, 27, 30, 33, 39, 40).

[113] James M. Gere. *Mechanics of Materials*. 6th edition. Belmont, CA: Thomson-Engineering, 2003. 940 pp. (cit. on pp. 25, 26).

[114]   Mathias Bachmayer. "Effizientes Positionieren am Beispiel Regalbediengerät". München: TU München, 2012 (cit. on p. 27).

[115]   Kurt Magnus, Karl Popp, and Walter Sextro. *Schwingungen*. Wiesbaden: Springer Fachmedien Wiesbaden, 2013 (cit. on p. 27).

[116]   Matthias Imboden and Pritiraj Mohanty. "Dissipation in Nanoelectromechanical Systems". In: *Physics Reports*. Dissipation in nano-electromechanical systems 534.3 (2014), pp. 89–146 (cit. on pp. 29, 33, 34, 37).

[117]   Michele Montinaro. "Coupling of Nanomechanical Resonators to Controllable Quantum Systems". phd. University_of_Basel, 2014. 127 S. (Cit. on pp. 30, 32, 39–41, 49–51).

[118]   B. D. Hauer, C. Doolin, K. S. D. Beach, and J. P. Davis. "A General Procedure for Thermomechanical Calibration of Nano/Micro-Mechanical Resonators". In: *Annals of Physics* 339 (2013), pp. 181–207 (cit. on pp. 30, 32, 39, 40, III).

[119]   S. Rast et al. "Force Microscopy Experiments with Ultrasensitive Cantilevers". In: *Nanotechnology* 17.7 (2006), S189 (cit. on pp. 34–36).

[120]   Hiroshi Hosaka, Kiyoshi Itao, and Susumu Kuroda. "Damping Characteristics of Beam-Shaped Micro-Oscillators". In: *Sens. Actuators Phys.* 49.1-2 (1995), pp. 87–95 (cit. on p. 35).

[121]   A. I. Volokitin and B. N. J. Persson. "Adsorbate-Induced Enhancement of Electrostatic Noncontact Friction". In: *Phys. Rev. Lett.* 94.8 (2005), p. 086104 (cit. on pp. 35, 36).

[122]   A. I. Volokitin, B. N. J. Persson, and H. Ueba. "Enhancement of Noncontact Friction between Closely Spaced Bodies by Two-Dimensional Systems". In: *Phys. Rev. B* 73.16 (2006), p. 165423 (cit. on pp. 35, 36).

[123]   Marcin Kisiel et al. "Suppression of Electronic Friction on Nb Films in the Superconducting State". In: *Nat Mater* 10.2 (2011), pp. 119–122 (cit. on p. 35).

[124]   Markus Langer et al. "Giant Frictional Dissipation Peaks and Charge-Density-Wave Slips at the NbSe2 Surface". In: *Nat Mater* 13.2 (2014), pp. 173–177 (cit. on p. 35).

[125]   R. Bennewitz, E. Gnecco, T. Gyalog, and E. Meyer. "Atomic Friction Studies on Well-Defined Surfaces". In: *Tribology Letters* 10.1-2 (2001), pp. 51–56 (cit. on p. 35).

[126]   M. Guggisberg et al. "Separation of Interactions by Noncontact Force Microscopy". In: *Phys. Rev. B* 61.16 (2000), pp. 11151–11155 (cit. on p. 35).

[127]   Markus Samadashvili. "Non-Contact Friction Studied with Pendulum AFM". phd. University_of_Basel, 2014. 105 p. (Cit. on p. 35).

[128] B. C. Stipe, H. J. Mamin, T. D. Stowe, T. W. Kenny, and D. Rugar. "Noncontact Friction and Force Fluctuations between Closely Spaced Bodies". In: *Phys. Rev. Lett.* 87.9 (2001), p. 096801 (cit. on pp. 35, 36).

[129] B. C. Stipe, H. J. Mamin, T. D. Stowe, T. W. Kenny, and D. Rugar. "Magnetic Dissipation and Fluctuations in Individual Nanomagnets Measured by Ultrasensitive Cantilever Magnetometry". In: *Phys. Rev. Lett.* 86.13 (2001), pp. 2874–2877 (cit. on p. 35).

[130] Kohta Saitoh, Kenichi Hayashi, Yoshiyuki Shibayama, and Keiya Shirahama. "Gigantic Maximum of Nanoscale Noncontact Friction". In: *Phys. Rev. Lett.* 105.23 (2010), p. 236103 (cit. on p. 35).

[131] Marcin Kisiel, Markus Samadashvili, Urs Gysin, and Ernst Meyer. "Non-Contact Friction". In: *Noncontact Atomic Force Microscopy*. Ed. by Seizo Morita, Franz J. Giessibl, Roland Wiesendanger, and Ernst Meyer. Cham: Springer International Publishing, 2015, pp. 93–110 (cit. on p. 35).

[132] M. Labardi and M Allegrini. "Non-Contact Friction Force Microscopy Exploiting Lateral Resonance Enhancement". In: World TRIBOLOGY Congress. Vienna, 2001 (cit. on p. 35).

[133] M. Labardi and M. Allegrini. "Noncontact Friction Force Microscopy Based on Quartz Tuning Fork Sensors". In: *Appl. Phys. Lett.* 89.17 (2006), p. 174104 (cit. on p. 35).

[134] Marcin Kisiel et al. "Dissipation at Large Separations". In: *Fundamentals of Friction and Wear on the Nanoscale*. Ed. by Enrico Gnecco and Ernst Meyer. NanoScience and Technology. Springer International Publishing, 2015, pp. 609–627 (cit. on p. 36).

[135] William E. Newell. "Miniaturization of Tuning Forks". In: *Science* 161.3848 (1968), pp. 1320–1326 (cit. on p. 37).

[136] Clarence Zener. "Internal Friction in Solids. I. Theory of Internal Friction in Reeds". In: *Phys. Rev.* 52.3 (1937), pp. 230–235 (cit. on p. 37).

[137] Ron Lifshitz and M. L. Roukes. "Thermoelastic Damping in Micro- and Nanomechanical Systems". In: *Phys. Rev. B* 61.8 (2000), pp. 5600–5609 (cit. on p. 37).

[138] A. Einstein. "Über Die von Der Molekularkinetischen Theorie Der Wärme Geforderte Bewegung von in Ruhenden Flüssigkeiten Suspendierten Teilchen". In: *Ann. Phys.* 322.8 (1905), pp. 549–560 (cit. on p. 39).

[139] A. Einstein. "Zur Theorie Der Brownschen Bewegung". In: *Ann. Phys.* 19 (1906), p. 371 (cit. on p. 39).

[140] A. A. Clerk, M. H. Devoret, S. M. Girvin, Florian Marquardt, and R. J. Schoelkopf. "Introduction to Quantum Noise, Measurement, and Amplification". In: *Rev. Mod. Phys.* 82.2 (2010), pp. 1155–1208 (cit. on p. 39).

[141]   Dennis Patrick Weber. "Dynamic Cantilever Magnetometry of Individual Ferromagnetic Nanotubes". phd. University_of_Basel, 2014. 111 S. (Cit. on p. 42).

[142]   M. Poggio, C. L. Degen, C. T. Rettner, H. J. Mamin, and D. Rugar. "Nuclear Magnetic Resonance Force Microscopy with a Microwire Rf Source". In: *Appl. Phys. Lett.* 90.26 (2007), p. 263111 (cit. on pp. 44, 45, 47, 48, 77, 84).

[143]   Ivan Tobias Tomka. "Methods in Magnetic Resonance Force Microscopy". theses. Diss., Eidgenössische Technische Hochschule ETH Zürich, Nr. 21493, 2014, 2014 (cit. on p. 45).

[144]   B. E. Herzog. "Magnetic Resonance Force Microscopy at Room Temperature". Masters Thesis. Basel: University of Basel, 2012 (cit. on p. 47).

[145]   H. J. Mamin, C. T. Rettner, M. H. Sherwood, L. Gao, and D. Rugar. "High Field-Gradient Dysprosium Tips for Magnetic Resonance Force Microscopy". In: *Appl. Phys. Lett.* 100.1 (2012), p. 013102 (cit. on pp. 47, 48).

[146]   Jonilyn Longenecker. "High-Gradient Nanomagnet-On-Cantilever Fabrication For Scanned Probe Detection Of Magnetic Resonance". 2013 (cit. on pp. 47, 100).

[147]   Allen Dean Drake and Dennis C. Leiner. "Fiber-optic Interferometer for Remote Subangstrom Vibration Measurement". In: *Review of Scientific Instruments* 55.2 (1984), pp. 162–165 (cit. on p. 49).

[148]   D. Rugar, H. J. Mamin, R. Erlandsson, J. E. Stern, and B. D. Terris. "Force Microscope Using a Fiber-optic Displacement Sensor". In: *Review of Scientific Instruments* 59.11 (1988), pp. 2337–2340 (cit. on pp. 49–51).

[149]   M. Poggio et al. "An Off-Board Quantum Point Contact as a Sensitive Detector of Cantilever Motion". In: *Nat. Phys.* 4.8 (2008). WOS:000258326000016, pp. 635–638 (cit. on p. 49).

[150]   Nicola Rossi et al. "Vectorial Scanning Force Microscopy Using a Nanowire Sensor". In: *Nat Nano* 12.2 (2017), pp. 150–155 (cit. on p. 49).

[151]   B. Gross et al. "Dynamic Cantilever Magnetometry of Individual CoFeB Nanotubes". In: *Phys. Rev. B* 93.6 (2016), p. 064409 (cit. on pp. 49, 55).

[152]   D. Cadeddu et al. "Time-Resolved Nonlinear Coupling between Orthogonal Flexural Modes of a Pristine GaAs Nanowire". In: *Nano Lett.* 16.2 (2016), pp. 926–931 (cit. on p. 49).

[153]   A. Buchter et al. "Magnetization Reversal of an Individual Exchange-Biased Permalloy Nanotube". In: *Phys. Rev. B* 92.21 (2015), p. 214432 (cit. on p. 55).

[154]   Norbert Müller and Alexej Jerschow. "Nuclear Spin Noise Imaging". In: *PNAS* 103.18 (2006), pp. 6790–6792 (cit. on pp. 65, 93).

[155] Jonathan P. Jacky, Joseph L. Garbini, Matthew Ettus, and John A. Sidles. "Digital Control of Force Microscope Cantilevers Using a Field Programmable Gate Array". In: *Rev. Sci. Instrum.* 79.12 (2008), p. 123705 (cit. on p. 69).

[156] B. A. Moores et al. "Accelerated Nanoscale Magnetic Resonance Imaging through Phase Multiplexing". In: *Appl. Phys. Lett.* 106.21 (2015), p. 213101 (cit. on pp. 69, 77).

[157] Mathieu Munsch et al. "Manipulation of the Nuclear Spin Ensemble in a Quantum Dot with Chirped Magnetic Resonance Pulses". In: *Nat. Nanotechnol.* 9.9 (2014). WOS:000341814400007, pp. 671–675 (cit. on p. 79).

[158] S. R. Hartmann and E. L. Hahn. "Nuclear Double Resonance in the Rotating Frame". In: *Phys. Rev.* 128.5 (1962), pp. 2042–2053 (cit. on p. 79).

[159] S. Hediger, B. H. Meier, Narayanan D. Kurur, Geoffrey Bodenhausen, and R. R. Ernst. "NMR Cross Polarization by Adiabatic Passage through the Hartmann—Hahn Condition (APHH)". In: *Chemical Physics Letters* 223.4 (1994), pp. 283–288 (cit. on p. 79).

[160] Waclaw Kolodziejski and Jacek Klinowski. "Kinetics of Cross-Polarization in Solid-State NMR: A Guide for Chemists". In: *Chem. Rev.* 102.3 (2002), pp. 613–628 (cit. on p. 79).

[161] A. Pines, M. G. Gibby, and J. S. Waugh. "Proton-enhanced NMR of Dilute Spins in Solids". In: *The Journal of Chemical Physics* 59.2 (2003), pp. 569–590 (cit. on p. 79).

[162] H. J. Mamin, R. Budakian, B. W. Chui, and D. Rugar. "Magnetic Resonance Force Microscopy of Nuclear Spins: Detection and Manipulation of Statistical Polarization". In: *Phys. Rev. B* 72.2 (2005), p. 024413 (cit. on p. 84).

[163] C. L. Degen, M. Poggio, H. J. Mamin, and D. Rugar. "Nuclear Spin Relaxation Induced by a Mechanical Resonator". In: *Phys. Rev. Lett.* 100.13 (2008), p. 137601 (cit. on p. 84).

[164] Jeremy Cardellino et al. "The Effect of Spin Transport on Spin Lifetime in Nanoscale Systems". In: *Nat Nano* 9.5 (2014), pp. 343–347 (cit. on p. 92).

[165] M.A. McCoy and R.R. Ernst. "Nuclear Spin Noise at Room Temperature". In: *Chem Phys Lett* 159.5-6 (1989), pp. 587–593 (cit. on p. 93).

[166] M Guéron and J.L Leroy. "NMR of Water Protons. The Detection of Their Nuclear-Spin Noise, and a Simple Determination of Absolute Probe Sensitivity Based on Radiation Damping". In: *J Magn Reson* 85.1 (1989), pp. 209–215 (cit. on p. 93).

[167] S A Crooker, D G Rickel, A V Balatsky, and D L Smith. "Spectroscopy of Spontaneous Spin Noise as a Probe of Spin Dynamics and Magnetic Resonance". In: *Nature* 431.7004 (2004), pp. 49–52 (cit. on p. 93).

[168]   N. Kikuchi et al. "Vertical Bistable Switching of Spin Vortex in a Circular Magnetic Dot". In: *Journal of Applied Physics* 90.12 (2001), pp. 6548–6549 (cit. on p. 95).

[169]   M. Schneider, H. Hoffmann, and J. Zweck. "Magnetic Switching of Single Vortex Permalloy Elements". In: *Appl. Phys. Lett.* 79.19 (2001), pp. 3113–3115 (cit. on p. 95).

[170]   Michal Urbánek et al. "Dynamics and Efficiency of Magnetic Vortex Circulation Reversal". In: *Phys. Rev. B* 91.9 (2015), p. 094415 (cit. on p. 95).

[171]   R. Badea, J. A. Frey, and J. Berezovsky. "Magneto-Optical Imaging of Vortex Domain Deformation in Pinning Sites". In: *Journal of Magnetism and Magnetic Materials* 381 (2015), pp. 463–469 (cit. on pp. 95, 96).

[172]   B. Van Waeyenberge et al. "Magnetic Vortex Core Reversal by Excitation with Short Bursts of an Alternating Field". In: *Nature* 444.7118 (2006), pp. 461–464 (cit. on p. 95).

[173]   V. Uhlíř et al. "Dynamic Switching of the Spin Circulation in Tapered Magnetic Nanodisks". In: *Nat. Nanotechnol.* 8.5 (2013), pp. 341–346 (cit. on p. 95).

[174]   Kenneth A. Taylor and Robert M. Glaeser. "Electron Diffraction of Frozen, Hydrated Protein Crystals". In: *Science* 186.4168 (1974), pp. 1036–1037 (cit. on p. 101).

[175]   I. Shlimak, V. I. Safarov, and I. D. Vagner. "Isotopically Engineered Silicon/Silicon-Germanium Nanostructures as Basic Elements for a Nuclear Spin Quantum Computer". In: *J. Phys.: Condens. Matter* 13.26 (2001), p. 6059 (cit. on p. 101).

[176]   Yasuo Shimizu and Kohei M. Itoh. "Growth and Characterization of Short-Period Silicon Isotope Superlattices". In: *Thin Solid Films*. Proceedings of the Fourth International Conference on Silicon Epitaxy and Heterostructures (ICSI-4)ICSI-4Proceedings of the Fourth International Conference on Silicon Epitaxy and Heterostructures (ICSI-4) 508.1–2 (2006), pp. 160–162 (cit. on p. 101).

[177]   Thomas F. Kelly and Michael K. Miller. "Atom Probe Tomography". In: *Review of Scientific Instruments* 78.3 (2007), p. 031101 (cit. on p. 101).

[178]   Alexander A. Zyuzin, Tobias Meng, Viktoriia Kornich, and Daniel Loss. "Nuclear Spin Relaxation in Rashba Nanowires". In: *Phys. Rev. B* 90.19 (2014), p. 195125 (cit. on p. 102).

[179]   Viktoriia Kornich, Peter Stano, Alexander A. Zyuzin, and Daniel Loss. "Voltage-Induced Conversion of Helical to Uniform Nuclear Spin Polarization in a Quantum Wire". In: *Phys. Rev. B* 91.19 (2015), p. 195423 (cit. on p. 102).

Appendices

A Appendices

A.1 Corrections of the Cantilever and Spin Resonance Frequencies

Correction of the Cantilever Frequency

Before calculating $f_{\text{centre}_{\text{corrected}}}$, the measured cantilever frequency f_{L_0} is slightly corrected in order to match the sampling rate:

$$f_{\text{L}_0\text{corrected}} = \frac{f_{\text{sampling}}}{\left[\frac{f_{\text{sampling}}}{f_{\text{L}_0}/2}\right] \cdot 2} \quad . \tag{A.1}$$

$f_{\text{L}_0\text{corrected}}$ is the corrected frequency of the cantilever, f_{sampling} the sampling rate of the arbitrary waveform generator and $[\dots]$ denotes the rounding to the nearest integer value.

Correction of the Spin Resonance Frequency

In order that the phase of concatenated ARP pulses is continuous, the centre frequency f_{centre} of f_{RF} has to be adjusted to fulfil $f_{\text{centre}_{\text{corrected}}} = n \cdot f_{\text{L}_0\text{corrected}}$, where $n \in \mathbb{N}$:

$$f_{\text{centre}_{\text{corrected}}} = \left(\left[\left(\frac{f_{\text{centre}}}{f_{\text{L}_0\text{corrected}}} - 1\right)/2\right] \cdot 2 + 1\right) f_{\text{L}_0\text{corrected}} \quad . \tag{A.2}$$

$f_{\text{centre}_{\text{corrected}}}$ is the corrected centre frequency of the modulated carrier frequency f_{RF} of an ARP pulse.

A.2 Experimentally Minimal Measurable Force

For individual frequencies $S_F(\omega)$ and $S_x(\omega)$ are connected via the generalised susceptibility $\chi(\omega)$ [118]

$$S_x(\omega) = |\chi(\omega)|^2 S_F(\omega) \quad , \tag{A.3}$$

whereas $\chi(\omega)$ is the ratio of the Fourier transforms of $x(t)$ and $F(t)$ [118]

$$\chi(\omega) = \frac{\mathcal{F}\{x(t)\}}{\mathcal{F}\{F(t)\}} = \frac{1}{m\left(\omega_{\text{L}_0}^2 - \omega^2 - i\omega_{\text{L}_0}\omega/Q\right)} \quad . \tag{A.4}$$

On resonance $\omega = \omega_{\mathrm{L}_0}$ eq. (A.3) becomes thus

$$S_x(\omega_{\mathrm{L}_0}) = \left(\frac{Q}{m\omega_{\mathrm{L}_0}^2}\right)^2 S_F(\omega_{\mathrm{L}_0}) \quad , \tag{A.5}$$

$$S_F(f_{\mathrm{L}_0}) = \left(\frac{k}{Q}\right)^2 S_x(f_{\mathrm{L}_0}) \quad . \tag{A.6}$$

From recalling eq. (3.55):

$$S_V(f) = S_{V_N} + \alpha_t^2 \left(S_{x_N} + S_x(f)\right) \tag{A.7}$$

and neglecting S_{V_N} since $S_{V_N} \ll S_{x_N}\alpha_t^2$, we know

$$S_x(f_{\mathrm{L}_0}) = \frac{S_V(f_{\mathrm{L}_0})}{\alpha_t^2} - S_{x_N} = \frac{S_V(f_{\mathrm{L}_0}) - S_{V_{\mathrm{floor}}}}{\alpha_t^2} \quad , \tag{A.8}$$

whereas $S_{V_{\mathrm{floor}}} = S_{x_N}\alpha_t^2$ is the measurement noise floor far away from f_{L_0}. Combining eqs. (A.6) and (A.8) we get

$$S_F(f_{\mathrm{L}_0}) = \left(\frac{k}{Q}\right)^2 \frac{S_V(f_{\mathrm{L}_0}) - S_{V_{\mathrm{floor}}}}{\alpha_t^2} \quad . \tag{A.9}$$

Finally, the experimentally minimal measurable force is

$$F_{\min}^{\mathrm{exp}} \cong \frac{k}{Q}\sqrt{\frac{S_V(f_{\mathrm{L}_0}) - S_{V_{\mathrm{floor}}}}{\alpha_t^2}\Delta f_{\mathrm{BW}}} \quad . \tag{A.10}$$

A.3 Force by Magnetic Moment in Gradual Field

Given is a magnetic moment $\vec{\mu}$ and the magnetic field $\vec{B}$

$$\vec{F} = \nabla\left(\vec{\mu}\cdot\vec{B}\right) \tag{A.11}$$

$$= \begin{pmatrix}\frac{\partial}{\partial x}\\\frac{\partial}{\partial y}\\\frac{\partial}{\partial z}\end{pmatrix}(\mu_x B_x + \mu_y B_y + \mu_z B_z) \tag{A.12}$$

$$= \begin{pmatrix}\left(\frac{\partial}{\partial x}\mu_x\right)B_x + \mu_x\frac{\partial}{\partial x}B_x + \left(\frac{\partial}{\partial x}\mu_y\right)B_y + \mu_y\frac{\partial}{\partial x}B_y + \left(\frac{\partial}{\partial x}\mu_z\right)B_z + \mu_z\frac{\partial}{\partial x}B_z\\ \left(\frac{\partial}{\partial y}\mu_x\right)B_x + \mu_x\frac{\partial}{\partial y}B_x + \left(\frac{\partial}{\partial y}\mu_y\right)B_y + \mu_y\frac{\partial}{\partial y}B_y + \left(\frac{\partial}{\partial y}\mu_z\right)B_z + \mu_z\frac{\partial}{\partial y}B_z\\ \left(\frac{\partial}{\partial z}\mu_x\right)B_x + \mu_x\frac{\partial}{\partial z}B_x + \left(\frac{\partial}{\partial z}\mu_y\right)B_y + \mu_y\frac{\partial}{\partial z}B_y + \left(\frac{\partial}{\partial z}\mu_z\right)B_z + \mu_z\frac{\partial}{\partial z}B_z\end{pmatrix} \quad . \tag{A.13}$$

Since $\frac{\partial}{\partial i}\mu_j = 0$ for all $i, j \in \{x, y, z\}$ the summands in brackets of the vector above vanish

$$\vec{F} = \begin{pmatrix} \mu_x \frac{\partial}{\partial x} B_x + \mu_y \frac{\partial}{\partial x} B_y + \mu_z \frac{\partial}{\partial x} B_z \\ \mu_x \frac{\partial}{\partial y} B_x + \mu_y \frac{\partial}{\partial y} B_y + \mu_z \frac{\partial}{\partial y} B_z \\ \mu_x \frac{\partial}{\partial z} B_x + \mu_y \frac{\partial}{\partial z} B_y + \mu_z \frac{\partial}{\partial z} B_z \end{pmatrix} \tag{A.14}$$

$$= \begin{pmatrix} \vec{\mu} \cdot \frac{\partial}{\partial x} \vec{B} \\ \vec{\mu} \cdot \frac{\partial}{\partial y} \vec{B} \\ \vec{\mu} \cdot \frac{\partial}{\partial z} \vec{B} \end{pmatrix} \tag{A.15}$$

With the x-component

$$F_x = \vec{\mu} \cdot \frac{\partial}{\partial x} \vec{B} \tag{A.16}$$

A.4 Micro-Wire Fabrication

A.4.1 Photolithography

With Ma-N 415 photoresist and Ma-D 332/S developer, exposed resist remains. Adapted from Fei Xue.

1. Clean the wafer's surface;

2. Remove the moisture and gases by baking it on a 120 Celsius hot plate for > 5 min;

3. Cool the wafer down by spinning it for 1 min;

4. Drop some photoresist Ma-N 415 onto the wafer;

    - Hold the bottle always at its neck since photoresists are sensitive to temperature;

    - Use a plastic pipette, remove bubbles inside the pipette before dispensing Ma-N 415 onto the wafer;

5. Remove possible bubbles on the waver with the pipette;

6. Spin photoresist, settings: 6000 rpm, 60 seconds, ramping up time 6 seconds;

7. Bake the wafer with photoresist on the 93 Celsius hot plate for 1.5 min;

8. Fix the mask on the mask aligner;

9. Place the waver in the mask aligner, make the alignment;

10. Make sure the lamp is ok;

11. Expose the sample, settings: Hard contact 6 seconds, CH1, 14 seconds;

12. Develop the sample with Ma-D 332/S, 110 seconds, longer developing time gives larger undercutting;

13. Rinse it with DI water for 20 seconds;

14. Check the pattern under a microscope.

A.4.2 Electron-beam Evaporation

In addition to the e-beam machine specific *Sharon* manual.

1. Make sure the Ti and Au targets are filled;

2. Mount the sample;

3. Pump, if possible over night to reach highest vacuum;

4. Evaporate according to the Sharon manual, respect the warm up times for both materials while having the shutters closed in order to achieve a stable evaporation rate;

   a) 10 nm Ti as sticking layer;

   b) 200 nm nm Au;

5. Dismount.

A.4.3 Photoresist Removal

Adapted from Fei Xue and Arne Buchter.

1. Bath it in NMP ($\gtrsim$ 2 h) at 50 °C, (probably even longer, in worst case at room temperature over night);

2. Carefully release the waste material by gently moving the beaker;

3. Bath it in acetone ($\sim$ 5 min) while gently moving, rinse (new beaker), do not let the wafer get dry until the next step, acetone leaves residues;

4. Bath it in acetone ($\sim$ 5 min) while gently moving, rinse (new beaker), do not let the wafer get dry until the next step, acetone leaves residues;

5. Bath it in isopropanol ($\sim$ 5 min) while gently moving, rinse (new beaker);

6. Bath it in isopropanol ($\sim$ 5 min) while gently moving, rinse (new beaker);

7. Rinse it DI water ($\sim$ 5 min);

8. Blow it dry with nitrogen to avoid stains;

9. Check the pattern under a microscope.

Acknowledgement

> " *A race without suffering isn't a race.* "

Martino Poggio, *by word of mouth*, $\sim$ 2013

Curriculum Vitae

Benedikt Eduard Herzog

Born on April 4th 1981 in Basel, Switzerland.

Department of Physics
University of Basel
Klingelbergstrasse 82
4056 Basel
Switzerland
ben.herzog@unibas.ch

Education And Relevant Work

2018   PhD (Dr. phil.) in Experimental Physics
       University of Basel, Switzerland
       Thesis on
       "Nuclear Spin Noise Examined by Magnetic Resonance Force Microscopy"
       in the group of Prof. Martino Poggio.

2012   Master of Science in Physics (M.Sc.)
       University of Basel, Switzerland
       Thesis on "Magnetic Resonance Force Microscopy at Room Temperature"
       and project on "Design of an UHV Magnetic Resonance Force Microscope"
       in the group of Prof. Martino Poggio.

2009   Bachelor of of Science in Physics (B.Sc.)
       University of Basel, Switzerland

2000   Matura Typ C
       Gymnasium Muttenz, Switzerland

List of Publications

[107]   B. E. Herzog, D. Cadeddu, F. Xue, P. Peddibhotla, and M. Poggio. "Boundary between the Thermal and Statistical Polarization Regimes in a Nuclear Spin Ensemble". In: *Appl. Phys. Lett.* 105.4 (2014), p. 043112.

[156]   B. E. Herzog. "Magnetic Resonance Force Microscopy at Room Temperature". Masters Thesis. Basel: University of Basel, 2012.

[181]   M. Poggio and B. E. Herzog. "Force-Detected Nuclear Magnetic Resonance". In: *Micro and Nano Scale NMR: Technologies and Systems*. Ed. by Jens Anders and Jan G. Korvink. Weinheim: Wiley-VCH, 2017, p. 31.